Nanostructured Optical Materials for Dye Solar Cells

Doctoral Thesis presented by

M Carmen López López

Institute of Materials Science of Seville (CSIC-US)

Supervisor
Dr. Hernán R. Míguez García

Sevilla, 2013

Table of Contents

Chapter 3

Panchromatic Photonis Crystal for Efficient Transparent Dye Solar Cells

Chapter 1

Dye Solar Cells: Generalities and Photon Management Strategies

1. Introduction

The increasing energy demands and shortage of fossil fuels have kindled worldwide research interest in developing new types of environmentally sustainable energy technologies. Nuclear power, wind and hydro energy are already strong players, but also solar energy is increasing. Photovoltaic technology is one of the most favorable ways to convert solar energy and is receiving extraordinary attention. Equally importantly to direct solar cell applications, investigations of these systems have created a vibrant field of physics, chemistry, and materials science, from which much new science has sprung.

Nowadays, the majority of new installations use monocrystalline and polycristalline silicon solar cells, which can achieve about 20–25% sun to power conversion efficiency[1] due to the excellent charge transport properties and environmental stability of high purity silicon. However, their high material, fabrication and installation cost and production time make look for new alternatives to them. Because of this, there has been a great deal of research on thin-film solar cells over the past years. Among all of them, Dye Solar Cell (DSC) is presented as a promising candidate for future large-scale

power production directly from sunlight and will be at the focus of our attention along this thesis.

This chapter will provide a general review about Dye Solar Cells as a credible alternative technology to conventional photovoltaic systems. Also, both their basic operating principles and the evaluation of the different strategies proposed in the last years to improve light-harvesting will be carried out, special interest being put in one dimensional photonic crystal based DSCs, since it will be the base of the work here exposed. The motivation and the aim of this thesis will be presented at the end of this chapter.

2. Dye Solar Cells: Generalities

The great attractive of DSCs stem from their low cost fabrication and their possibility to be designed in a variety of different colours and transparencies, which distinguishes them among other types of solar cells and make them ideal for building integrated photovoltaic (BIPV) applications. Recently, commercial technologies, such as transportable chargers, solar bags, wireless solar keyboards or photovoltaic windows integrating this technology have appeared. It therefore seems only a matter of time before large production starts. Figure 1.1 shows some of these potential applications and several prototypes of transparent, coloured and flexible DSCs.

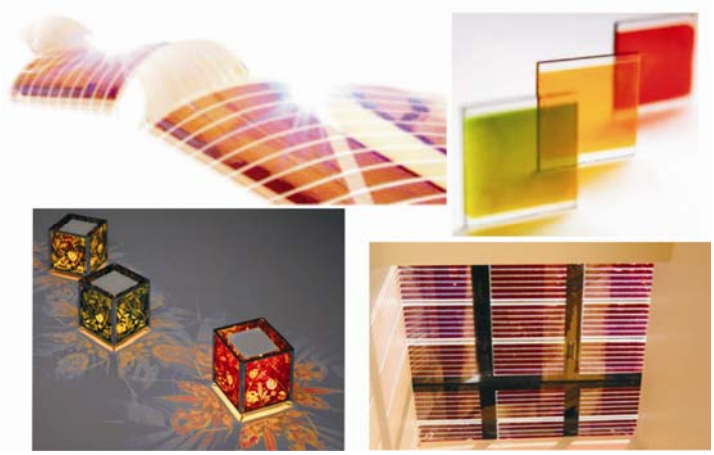

Figure 1.1. *Prototypes of DSCs (extracted from Oxford Photovoltaics, Dyesol and Sony websites).*

2.1. Background

An important first step on the development of DSCs was given by Fujishima and Honda, who found that titanium dioxide (TiO_2) could split water with a small bias voltage when exposed to light.[2] However, the conversion efficiency was low when using the sun as illumination source owing to the large band-gap for TiO_2, which makes it transparent for visible light. Some years previously, Gerischer and Tributsch studied how to extend the absorption range of semiconductor electrodes into the visible region by integrating a dye as a sensitizer.[3,4] In this way electrons are injected from photoexcited dye molecules into the conduction band of the n-type semiconductor, but light absorption was low since only dye molecules directly attached to the semiconductor surface were efficiently photoactive. Grätzel and his co-workers solved this issue by employing nanoporous TiO_2 electrodes,[5,6,7] providing huge surface area. By designing proper electrode thickness and sensitization dyes, DSCs are able to absorb most of the visible light. Since this first successful combination of nanostructured electrodes and efficient charge injection dyes numerous studies have investigated dye solar cells (DSCs) as an alternative next generation solar cell. Their evolution has continued to progress, and solar light-to-electricity conversion efficiencies have now exceeded 11%.[8-12]

2.2. DSC Structure and Working Principle

The basic functioning principles of the DSC are related to natural photosynthesis and are fundamentally different from those of conventional semiconductor p–i–n junction solar cells such as crystalline Silicon. In DSCs, light absorption and charge transport are separated with charge carrier generation taking place in the chemisorbed self-assembled monolayer of sensitizer molecules sandwiched between a wide band-gap semiconductor (usually titanium dioxide) and a redox electrolyte acting as electron and hole conducting materials.

At its standard configuration (Figure 1.2), DSCs are comprised of the working electrode comprising a dye-absorbed porous nanocrystalline TiO_2 (nc-TiO_2) film deposited on a transparent conductive oxide (TCO) substrate, an electrolyte containing a reduction-oxidation couple such as I^-/I^{3-} and a catalyst coated counter-electrode, the electrical circuit being completed via electron migration through the external load. Essential to the optical of this porous

electrode structure is the fact that TiO_2, as a large band gap semiconductor, absorbs only below λ~400 nm, letting the major part of the solar spectrum available for the dye molecules. The regenerative working cycle of DSCs is in Figure 1.2 and depicted in what follows.

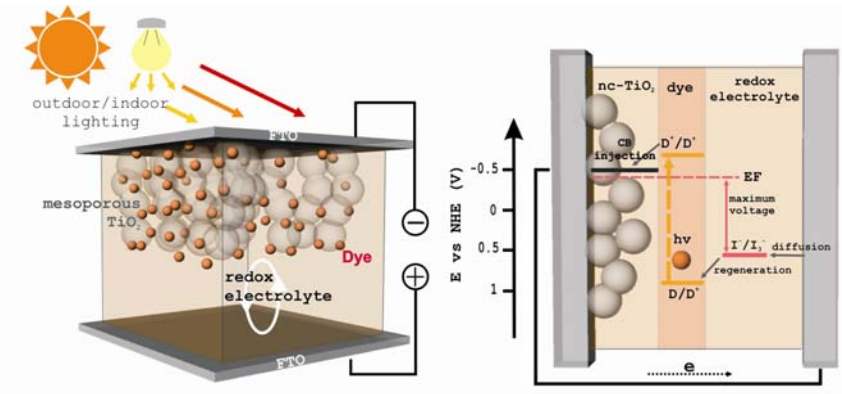

Figure 1.2. *Illustrative scheme and energetics of the operation mechanism that governs the functioning of a typical liquid electrolyte based DSC.*

The performance of a DSC is predominantly based on four energy levels of its components; the excited state (LUMO) and the ground state (HOMO) of the photosensitizer, the Fermi level of the TiO_2 electrode, which is located near the conduction-band level, and the redox potential of the mediator (I^-/I_3^-) in the electrolyte. The incoming photons excite the electrons on the ground state (or HOMO) of dye, generally based on a ruthenium polypyridyl complex, to the excited state (or LUMO) of dye, which is refereed to charge generation step. These photo-excited electrons are injected in the conduction band of TiO_2. This injection process is in competition with the decay of the excited state by luminescence, thermal decay to ground-state, or quenching. The photo-injected electrons are then transported through the porous TiO_2 network and eventually collected on TCO, which is denoted as charge collection step. Those three successive steps are essential for photocurrent generation. On the other hand, the oxidized dyes are regenerated by oxidation of iodide. Open-circuit voltage is generally determined by the energy difference between the Fermi level of TiO_2 and the redox electrolyte potential. Charge collection efficiency is not always 100% since photo-injected electron may be transferred back to the oxidized species of the electrolyte. The photocurrent measured externally is the flux of injection minus the flux of both recombination reactions.

2.3. Photovoltaic performance

The standard characterization techniques of DSC include the determination of the photocurrent-voltage characteristics (also known as IV curves) under different light irradiance and the determination of the incidence photon to collected electron (IPCE) efficiency, which is often referred as external quantum efficiency (EQE), under low intensity monochromatic light.

IV curve represents an integrated response of the cell to all incident wavelengths simultaneously. The standard test conditions correspond to power density of 1 sun (100mW/cm2), light spectrum of an air mass 1.5 global (AM1.5G) and working temperature of 25°C. Experimentally, these curves are the result of varying the resistance of the outer circuit (Figure 1.3.A). Parameters like short circuit current (I_{sc}), open circuit voltage (V_{oc}), fill factor (ff) and power conversion efficiency (η) of the solar device are obtained from this characterization: I_{SC} is attained when the resistance of the outer circuit is zero (thus voltage is zero) and V_{OC} when the resistance reaches its maximum value (thus photocurrent is zero). The power output (η) of the device is finally calculated combining these parameters extracted from the IV curve and by the incident light intensity (P_{in}) that impinges the cell:[13,14]

$$\eta = \frac{Jsc.Voc.ff}{Pin} \qquad 1.1$$

where, ff, denoted as the fill factor of the cell, can be calculated through the following the equation 1.2, where Pmax correspond to the maximum power output of the device.

$$ff = \frac{Pmax}{Jsc.Voc} \qquad 1.2$$

Incident Photon-to-electron Conversion Efficiency (IPCE) measurements, on the other hand, quantify how many incident photons at a single wavelength are converted in extracted electrons at the electrodes. It strictly depends on the optical and electrical properties of the cell, as follows:[15,16]

$$IPCE(\lambda) = LHE(\lambda)\phi(\lambda)\xi(\lambda) \qquad 1.3$$

Where, *ϕ(λ)* and *ξ(λ)* are, respectively, the yield of electron injection from the excited state of the dye to the conduction band of the semiconductor oxide and the charge collection efficiency and LHE the light harvesting efficiency (LHE) or absorptance (Figure 1.3.B). This latter is defined as the fraction of incident photons that are absorbed by the dyed electrode and is reduced by optical

phenomena, such as reflections, transmission and competitive absorption. Injection and collection efficiencies depend on electrical mechanisms at widely different time scales. While the injection counts how many excited electrons are transferred from dye molecules to titanium dioxide film, the collection efficiency says how many injected electrons into the titanium dioxide film reach the electrodes.

IV characteristics and IPCE spectra can be related each other. Actually, from the complete IPCE spectra, it is possible to calculate the short circuit current that one should measure under a solar simulator in the following way:

$$Jsc = \int qIPCE(\lambda)F(\lambda)d(\lambda) \qquad 1.4$$

Where q is the electron charge and F(λ) is the ratio between the solar spectra irradiance and the photon energy.

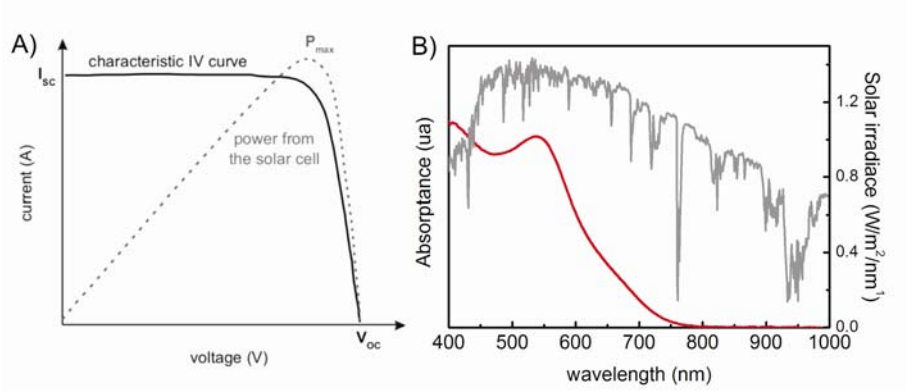

Figure 1.3. A) Characteristic IV curve measured for a DSC and photovoltaic parameters determining the overall conversion efficiency of the device (I_{SC}, V_{OC}, ff). B) Comparison between the spectral irradiance of AM 1.5 sunlight and the absorption spectrum corresponding to a N719 sensitized TiO_2 film.

3. Photon management strategies

As it was exposed in the previous section, the power conversion efficiency of DSCs is intimately linked with the number of photons collected by the dye molecules attached to the semiconductor. Taking this into consideration, photon management approaches based on improving or extending the optical absorption properties of DSCs will improve the photocurrent generated by these solar devices.

Light trapping encompasses an array of nano-engineering techniques designed to increase the optical absorption caused by either an enlargement of the photon path length through the working electrode or light trapping effects occurring within the TiO_2 electrodes, thus enhancing the power conversion efficiency of the cell. Whereas such approaches have been largely employed in other types of thin film solar cells,[17-22] it has not been easy to adapt their implementation in DSCs due to the delicate sensibility of the charge transport and recombination dynamics to any alteration of the nature of the interfaces present in this sort of solar device.[23]

In this section, I will give a brief review of the efforts carried out to improve the light harvesting in DSCs through the optimization of their optical design and provide a detailed description of the new emerging possibilities such as the use of plasmonic particles or the integration of different periodic structures. A further description of one dimensional photonic crystals based dye solar cells (1DPC-DSCs) will be reported, which will allow the reader to put this thesis work into perspective.

3.1. Diffuse scattering approach

The basic goal of a diffuse scattering approach is to extend the traveling distance of light within the photoelectrode film as a result of randomizing the light path. In this way, the opportunity for photons to be absorbed by the dye molecules is increased, and consequently, the light harvesting efficiency of the photoelectrode, as well as the conversion efficiency of the solar cell, is enhanced.

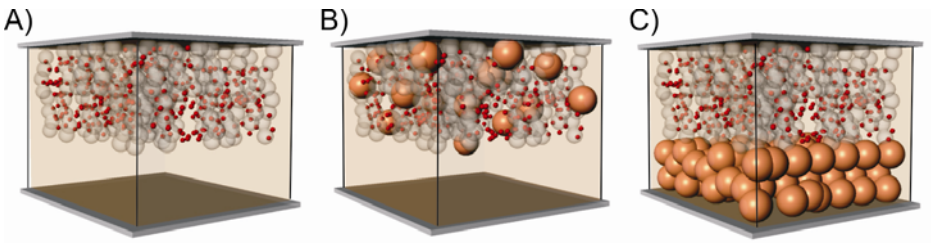

Figure 1.4. Schemes showing: A) a standard cell consisting of a semitransparent electrode and the ones based on diffuse scattering, B) involving the incorporation of larger particles inside the nanocrystalline film, and C) including a thick layer of such particles deposited on top of it.

Quite a few theoretical works have reported the design and optimization of the structure of DSC photoelectrodes integrating a light scattering function. The introduction of large TiO_2 particles as backscattering layer in DSCs for a more effective absorption of incident solar energy was firstly studied by A. Usami in 1997.[24] In another effort to integrate into DSCs the diffuse scattering concept, Ferber and Luther demonstrated that an enhancement in photon absorption could be produced when a suitable mixture of small and large particles was used as photoanode.[25] It is worth pointing out that, since Mie scattering, which depends on features such as particle size and refractive index, is best applicable to single scattering[26], the simulation of multiple scattering caused by large particles close to each other become a more complex task. Numerous theoretical works[27-32] have investigated multiple light scattering designs from large particles when incorporated in DSCs under different configurations in order to evaluate its potential for an efficient light collection. Schemes representing the main optical designs of the cell by considering the abovementioned approximations are displayed in figure 1.4.

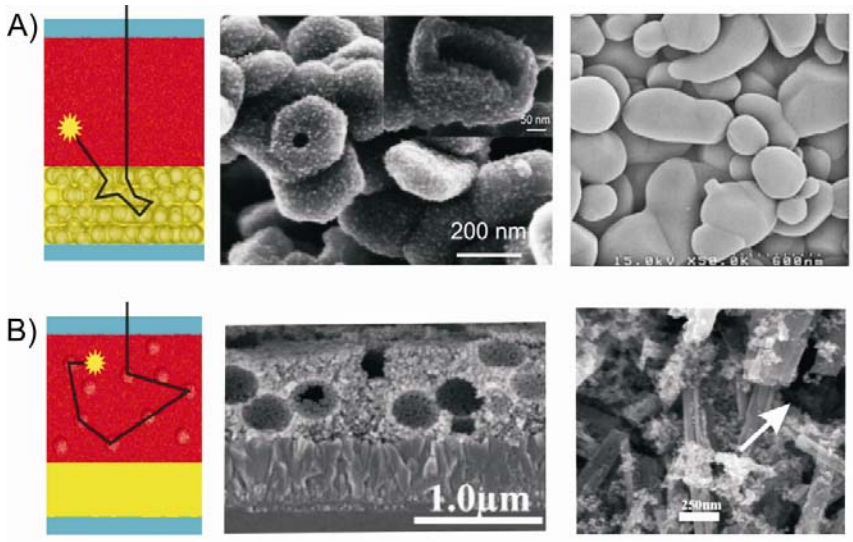

Figure 1.5. *Schemes showing different trajectories travelled by the incident light that strikes a DSC (extracted from reference 32) and SEM pictures of A) different kinds of particles commonly used as diffuse scattering layers (extracted from references 36 and 35) and B) different mixture structures as photoelectrodes of DSCs.(extracted from references 37 and 38).*

Experimental evidence that light scattering from both the double-layer structure[33-36] and the mixture designed photoelectrode[37-39] increase the photocurrent response of DSCs have appeared. Figure 1.5 shows some

examples of different particles, which were used to this end. It is also important mentioning that practically all DSCs exhibiting the highest efficiency values reported until now at laboratory scale incorporate the additional porous backscattering film made of larger particles, which are deposited onto the photoactive layer to reflect any non absorbed light back into the film.[8-12] However, this optical element has the unfortunate effect of rendering the DSC opaque thus depriving it of one of its main advantages over competing technologies as window photovoltaic panels or any other application where transparency is required from these devices.

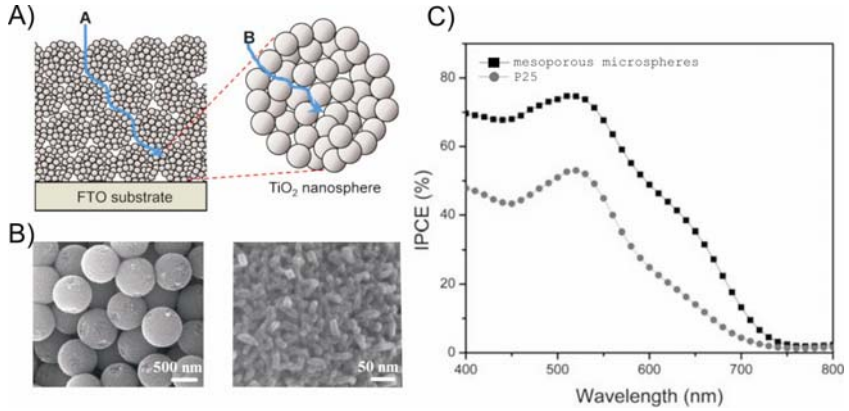

Figure 1.6. A)Schemes of aggregate structures (extracted from reference 44), B)SEM images corresponding to theses aggregates particles (extracted from reference 43), C) IPCE curves of the TiO_2 electrodes prepared from mesoporous TiO_2 microspheres and commercial-available P25 TiO_2 nanoparticles of 12 μm thickness (extracted from reference 44).

Aside from the above methods, photoelectrodes with a more sophisticated structure, for example, using multiple scattering layers, have been investigated to better enhance the optical absorption of DSC photoelectrodes.[33,40]

On the other hand, hierarchical nanostructures comprised of nano-sized building blocks, have been recently applied to dye-sensitized solar cells (Figure 1.6).[41-45] As a result, in a first approximation, these photoelectrodes may possess sufficient internal surface area for dye adsorption and meanwhile may generate highly effective light scattering. Some other merits, such as the capability to enhance electron transport, have been also observed on the hierarchically structured films. The advantages of hierarchically structured photoelectrode films in optical absorption, plus the other merits in terms of dye adsorption and charge transport, make the hierarchically structured

photoelectrode film an extremely promising candidate for achieving high-efficiency DSCs over the existing films.

3.2. Plasmonic light trapping schemes

Plasmonic nanostructures have been recently investigated as a possible way to improve absorption of light in dye solar cells since it has been demonstrated their suitability on several thin-film solar cells.[46-50] Surface plasmon resonances from noble metal nanostructures can give rise to unique properties, such as an intense absorption feature and enhanced local electromagnetic field. In general, two main basic mechanisms have been proposed to explain photocurrent enhancement by metal particles incorporated into or onto solar cells:[51-53] light scattering, which couples and traps freely propagating plane waves from the Sun into the photoactive layer, and near-field concentration of light, which is capable of greatly increasing the effective molecular dye absorptivity.[54]

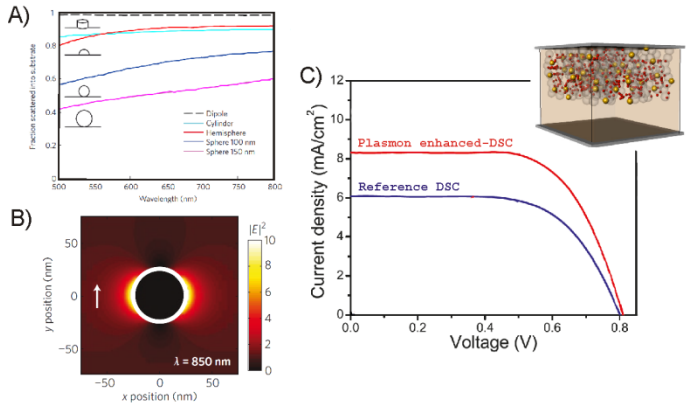

Figure 1.7. A) Fraction of light scattered into the substrate, divided by total scattered power, for different sizes and shapes of Ag particles on Si. B) The near field calculated close to the surface of a 25 nm diameter Au particle embedded in a medium with refractive index of 1.5 (extracted from reference 53) C) Improvement in photocurrent attained for a DSC made of a thin active layer after incorporating core shell metal oxide (Ag@TiO_2) nanoparticles. (extracted from reference 59)

Most of the earlier work on plasmon assisted DSCs including noble metal nanoparticles in different configurations reported only improved dye absorption or photocurrent, however the improved device performance was not appreciated.[55-57] Beyond this, it was also observed that bare metal nanoparticles in direct contact with the dye and the redox pair electrolyte,

resulted in recombination and back reaction of photogenerated carriers and corrosion of metal nanoparticles by electrolytes.[57] To address this problem, metal nanoparticles coated with a thin TiO_2 or SiO_2 shell have been successfully applied to efficient harnessing of light into the mesoporous electrode with alleged negligible influence on the optical properties. Furthermore, they are corrosion resistant in the iodide/triiodie electrolyte and have no apparent detrimental electronic consequence in the solar cells, as far as charge recombination is concerned.[58-60] These studies have shown that plasmonic enhancement is indeed a viable and novel path toward improving DSCs performance.

3.3. Structured surfaces for light trapping

An alternative to the use of random structures like those above mentioned to amplify the optical absorption of DSCs is the introduction of backside grating structures to diffract incident light into highly oblique angles (Figure 1.8.A). The diffraction induced by such interfaces improves light trapping by increasing the distance that light travel into the photoactive layer. Furthermore, if the angle of the diffracted beam is greater than the critical angle, light will be also reflected back at the top surface by total internal reflection. In particular, these periodic structures have been used extensively to enhance absorption in silicon solar cells,[17,61,62] thereby increasing the power conversion efficiency. However, until very recently, only a few studies based on such approach in DSCs have been reported.[63,64] These first works made use of a soft lithography approach to replicate the grating from an elastomeric stamp to the back side of the nanoparticle TiO_2 electrode. By this means, incident light that reaches the backside grating can be diffracted backward increasing the distance that light must travel within the active layer and thus the probability of the photons to be absorbed by the dye. Figure 1.8 display several examples of these molded electrodes and their effect over the photovoltaic performance of DSCs.

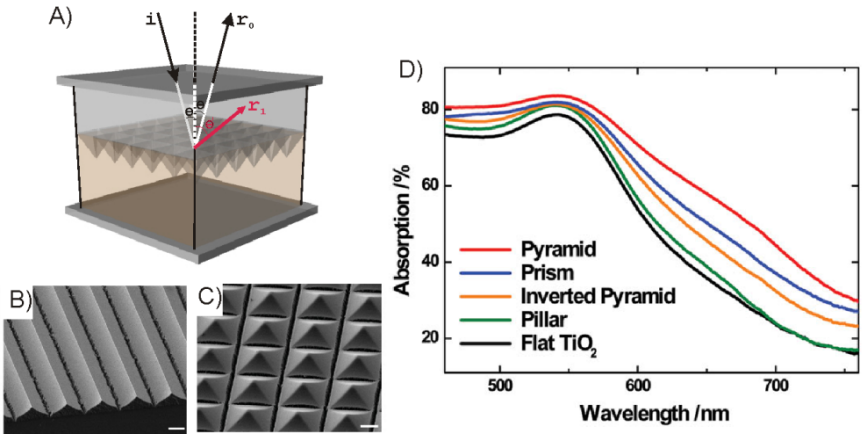

Figure 1.8. *A) Illustration of a DSC with a diffraction grating on the electrode back. B-C) SEM images of nanopatterned electrodes. (scale bars in the SEM pictures: 10 □m). D) Effect of nanopatterned electrodes have on the DSC absorptance. (extracted to reference 64)*

Finally, metal grating elements coupled to DSC have been explored to improve the cell efficiency as result of combining diffraction grating and plasmonic structures. [65,66] In this way the propagating surface plasmon polaritons (SPP) waves is most efficiently excited thanks to the periodic grating structures. At this point, an important distinction have to be made between the excitation localized surface plasmon (SP) resonances that occur when conduction electrons in finite-sized particles are driven into oscillation, and SPPs which are surface electromagnetic waves that propagate along metal surfaces. SPPs have their highest field intensity at the metal/dielectric interface, although they also exhibit a large penetration depth into the dielectric medium adjacent to the metal. For this reason, the excitation of SPP can produce absorption enhancements in thicker active layers in a solar cell. Two example of this light trapping strategy in dye solar cells are displayed in figure 1.9.

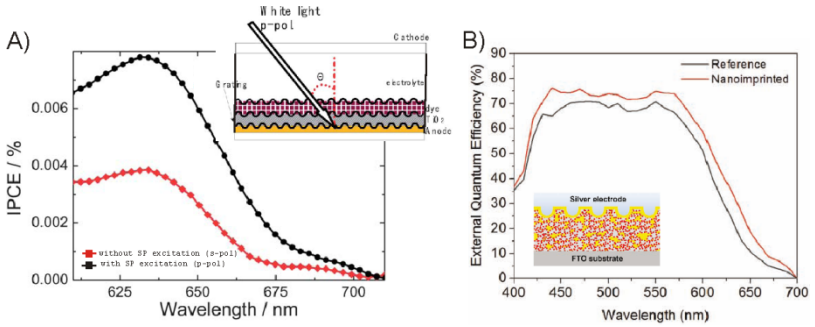

Figure 1.9. *A) IPCE with and without SP excitation measured at incident angle of 10° for the cell design presented in the upper side. B) External quantum efficiency (EQE) spectra of the cell configuration indicated graph inside and using C220 dye. (These results were extracted from references 65 and 66 respectively).*

3.4. Photonic crystal as back reflectors

Other approach based on the use of periodic structures to enhance light harvesting in specific parts of the spectrum is the introduction of porous materials in which a periodic variation of the refractive index has been built up. Depending on the spatial dimensions where the modulation of refractive index is found, we will refer these structures as one, two, or three dimensional photonic crystals (1DPC, 2DPC, or 3DPC, respectively)[67]. The interference effects associated with these periodic dielectrics give rise to the opening of a photonic band gap whose effect is detected as a maximum in the specular reflectance spectrum of the structure. When, in a first approximation, juxtaposed to a thin photoactive anode, photonic crystals (PCs) act as back mirrors reflecting coherently the light in a targeted wavelength range, determinated by the lattice constant and the average refractive index of the photonic crystal, localizing the photons of this frequency range in the photoactive layer increasing in this way the chances of them being harvested by the cell.

Three Dimensional Photonic Crystals based DSCs

In 2003, in an earlier work by Mallouk and co-workers, the optical absorption enhancement effect of a DSC coupled to a particular type of 3DPC was demonstrated for the first time.[68] The structure employed, an inverse opal, was composed of air voids periodically arranged in a semiconductor oxide matrix,

in this case TiO_2, thus allowing proper electrolyte diffusion to take place. By doing so, IPCE was shown to increase with respect to that of a standard cell used as reference. In a first approximation this result was attributed to the reduction of the group velocity of photons near the edge of a stop band or photonic pseudogap, which implies the increase of the probability of absorption. In a subsequent study, this absorption enhancement was also partly explained by the diffuse scattering caused by imperfections presented in the opal structure.[69] However, some aspects of the observed enhancement remained unclear or were apparently contradictory. Some years later, the origin of this improvement was further reviewed by A. Mihi and H. Míguez, and they found that its leading cause was the back reflection into the unstructured dyed electrode of photons with energies lying in the photonic band gap frequencies of the dielectric mirror.[70] Experimental evidence that confirms this theoretical model was also reported and, as predicted, the improvement was found for frequencies comprised within the photonic pseudogap of the inverse opal structure, as it can be observed in figure 1.10.B.[71,72] The selection of this region is made through the lattice parameter of the photonic crystal which is controlled both by the size of the templating spheres and the infiltration degree. It is also possible to pile up several inverse opal films with different lattice parameters to obtain an amplification of optical absorption over a wider spectral range.[73]

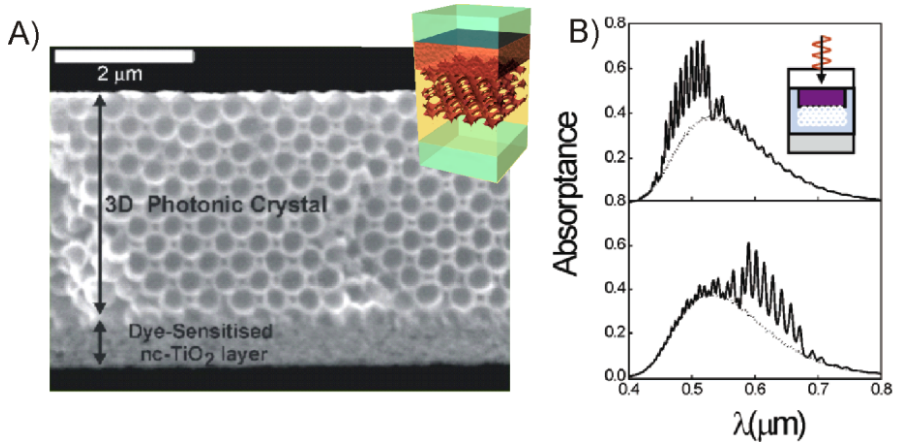

Figure 1.10. A) SEM image of an inverse TiO_2 opal grown on top of a nanocristalline titania layer. B) Absorption spectra of DSCs in which have been pill up two inverse opals with different lattice parameters, the absorptance of a standard cell is also plotted for the sake of comparison (dotted line). (Figure extracted from reference 70)

One Dimensional Photonic Crystals based DSCs

Experimentally, the main drawback of the 3D structures is the difficult assembly process to achieve reasonable reflecting periodic materials, which leads usually to thick structures, which might have a deleterious effect on charge transport and recombination through the cell. As an alternative, porous one dimensional photonic crystal (1DPC) structures made by alternative layers of SiO_2 and TiO_2 nanoparticles[74] were integrated in dye solar cells.[75] The arrangement of silica-titania bilayers creates a periodic refractive index responsible of interference phenomena that give rise to the opening of a photonic band gap in a well-defined wavelength range, whose effect is detected as a maximum in the specular reflectance spectrum of the structure. The position of this maximum could be roughly estimated through a combination of Bragg's law and Snell's law as follows:

$$\lambda_m = \frac{2\Delta}{m}\sqrt{n_{eff}^2 - sin^2\theta} \qquad 1.5$$

Where m is the diffraction order, Δ is the period or unit cell thickness, θ is the angle between the direction of incidence and the direction normal to the surface of the arrangement and *neff* is the effective refractive index of the structure. The latter can be in turn calculated as,

$$n_{eff} = \frac{n_1 d_1 + n_2 d_2}{d_1 + d_2} \qquad 1.6$$

Where,

$$\Delta = d_1 + d_2 \qquad 1.7$$

n_1 and n_2 being the refractive indexes of each layer, and d_1 and d_2 their respective thicknesses. At normal incidence, and considering only the first diffraction order, the position of the reflectance maximum could be simplified as,

$$\lambda_B = 2\Delta n_{eff} \qquad 1.8$$

, so any change the thickness of the layers would affect the spectral position of the Bragg peak (λ_B), as it can be seen in figure 1.11.A, where the reflectance spectra of several multilayer with different lattice parameters are plotted. In Figure 1.11.C some photographs displaying the wide variety of coloured

reflections arising of these structures are also shown. The evolution of the optical properties with the number of layers (N) forming the optical structure is illustrated in Figure 1.11.B, and, as can be clearly observed, as the number of layers in the stack is increased, the reflectance maximum becomes both narrower and more intense.[76] The main advantages of such lattices lie in the possibility to obtain accurate control over the optical properties of the periodic ensemble, and on the high structural and optical quality attainable, even more when compared to the selft-assembly opals commonly used for the same propose.

The novelty of these nanostructures that made them suitable for their integration in dye solar cells was the accessible interconnected mesoscopic porosity that they present; it also implies that the liquid electrolyte containing the redox pair can flow through them, soaking all the solar device. Furthermore, the easy colloidal chemistry approaches used to the fabrication of these nanoparticle 1DPCs are compatible with the processing method of DSCs making these photonic crystals suitable to be implemented in this type of solar devices to improve their performance.

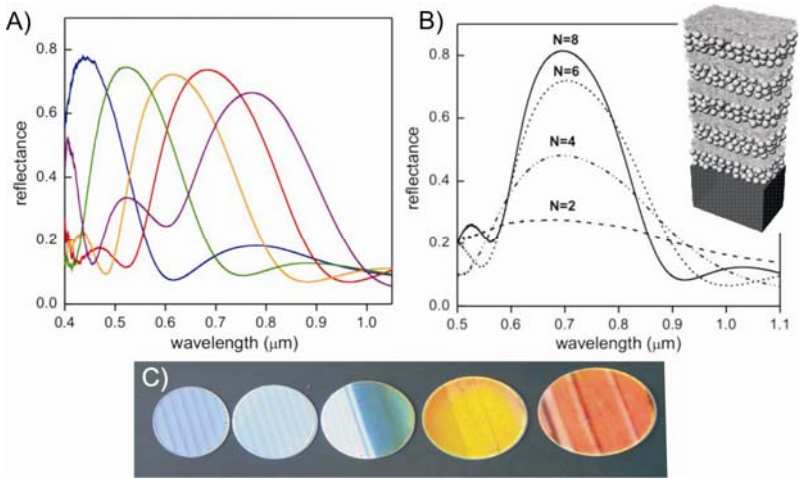

Figure 1.11. *Evolution of the reflectance spectrum of a SiO_2-TiO_2 nanoparticle multilayer A) with the lattice parameter and B) with the number of unit cells (Extracted from reference 74). C) Images of different 1DPCs with different thickness of the unit cell displaying different colors.*

By making use of this approach, optical absorption enhancement of a DSC could be selectively tuned over the whole visible range by appropriately selecting the back reflecting properties of the periodic structure, which could be

done by a simple modification of the lattice parameter of the periodic arrangement, as explained before. Consequently, it can be devised to present a Bragg peak that precisely matches the absorption band of the dye, but that has no effect on the longer visible wavelengths, keeping the reddish transparency of the cell unaltered, one of the main added values of this type of solar cell. In Figure 1.12.A, the transmission spectra of two device in which two 1DPCs with different lattice are integrated is displayed, the transmittance of a reference cell (without any optical element) and those of a scattering layer based DSC is also plotted for the sake of comparison. In this latter case, it can be clearly seen that the cell transparency is completely lost due to the lack of spectra selectiveness of the incoherent scattering produced by slurries with a wide distribution of particle size.

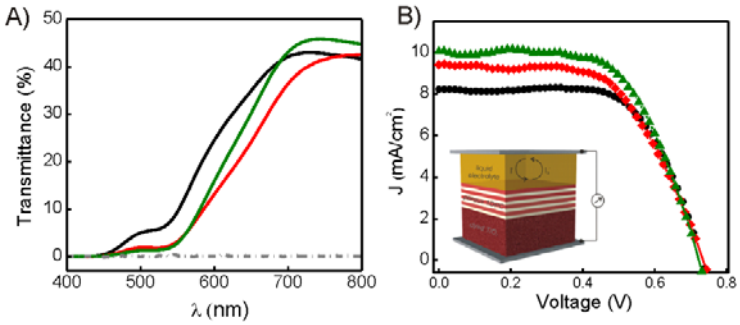

Figure 1.12. A) Transmittance spectra of a DSC composed of a 7.5μm thick titania electrode (black curve) and of the same electrode coupled to PCs with different lattice parameters (green and red curves) For comparison, the transmittance spectra of a scattering layer based DSC is also plotted (grey dashed line). B) IV curve measured from the reference cell (black) and the PC based DSC (green and red) (Extracted from reference 75).

In figure 1.12.B the IV curves for a reference cell and for a cell coupled to a photonic crystal are plotted. It can be seen that the 1DPC causes a significant raise of the photocurrent. The origin of this improvement was also analyzed and it was found that the magnitude of this effect depended on the spectral width and position of the photonic band gap relative to the absorption band of the ruthenium dye and the degree of optical coupling to the dye-sensitized electrode, which depends in turn on the thickness of that electrode.[77,78]

On the other hand, since the Bragg reflection intensity increases with the number of layers, as it was explained before, the performance of the device is also expected to increase. The theoretical effect of coupling 1DPCs having a

different number of unit cells (N) was also studied and it is displayed in figure 1.13.A. However, this behavior is not observed experimentally (Figure 1.13.B). This result, together with the fact that the introduction of a 1DPC within the cell actually decreases the fill factor, suggested that there might be electrolyte diffusion problems through the photonic structure.

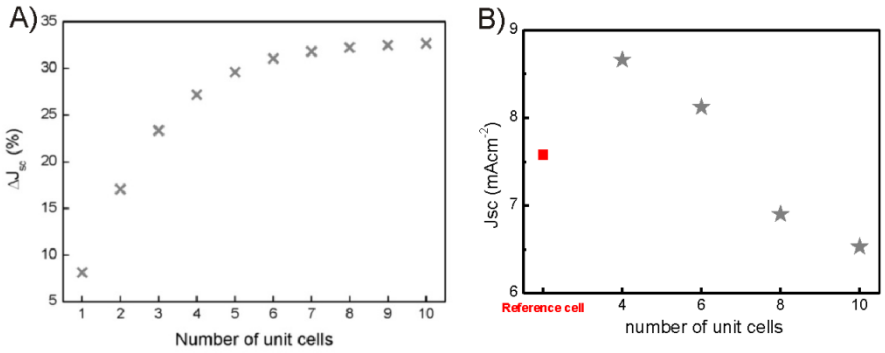

Figure 1.13. A) Theoretical increment of photogenerated current vs the number of layers that constitute the PC structure coupled to a 7.5 µm thick absorbing electrode (Extracted from reference 78). B) Experimental data of photogenerated current vs the number of unit cells of the photonic crystal coupled to a 5 µm thick electrode.

4. Motivation and goals of this thesis

In the wake of the successful result of coupling nanoparticle 1DPCs to dye solar cells as light harvesting enhancers, this thesis project was outlined. Keeping in mind the potential building integration photovoltaic applications of such devices, it seems to be reasonable that alternatives aiming to a better solar cell performance also seek to preserve their main features, i.e. transparency, guideline that is clearly achieved when 1DPC is used to improve solar radiation harnessing of DSCs. However, as it has been pointed out in this introduction, there is still a long way to optimize the performance of DSCs integrating photonic crystals.

In this context, the main challenge was to improve the diffusion of the electrolyte through the multilayer looking for the optimum 1DPC based DSC performance and reviewed all the possibilities that these multilayer offered to improve dye solar cell efficiency. The goals of the thesis herein presented, entitled "*Nanostructured optical materials for dye solar cells*", concern:

- The development of an experimental procedure that allows enlarging both the porosity and pore size distribution of the layers forming the 1DPC with the aim of improving the mass transport through the whole nanoparticle structure. It also implies the development of a porosimetry technique that gives rise to an exhaustive structural characterization of nanoparticle films and the study of the performance of this new design of 1DPC based DSC. These issues will be discussed in detail in Chapter 2.
- The integration of a panchromatic 1DPC, whose reflectance peak covers the whole visible range and that mimics the performance of a scattering layer to improve light harvesting in DSC while preserving semitransparency will be presented in Chapter 3.
- Regarding the possible use of 1DPC based DSCs in Building Integrated Photovoltaics (BIPV), an exhaustive study of the performance of such devices with the incident light angle will be carried out in Chapter 4.
- The use of one dimensional diffraction gratings patterned on the back side of the electrodes will be proposed as optical absorption enhancer in Chapter 5. A novel method to fabricate this structured film will be presented and a study of its diffractive properties and its effect on the photovoltaic properties of DSCs will be discussed.

5. References

[1] M.A. Green, K. Emery, Y. Hishikawa, W. Warta, E.D. Dunlop, Solar cell efficiency tables (version 39), Progress in Photovoltaics: Research and Applications 20 (2012) 12–20.

[2] A. Fujishima, K. Honda, *Nature*, 1972, **238**, 37.

[3] H. Gerisher, H. Tributsch, *Berich. Bunsen Gesell.*, 1968, **72**, 437.

[4] H. Gerischer, M.E. Michel-Beyerle, F. Rebentrost, H. Tributsch, *Electrochim. Acta*, 1968, **13**, 1509.

[5] N. Vlachopoulos, P. Liska, J. Augustynski, M. Grätzel, *J. Am. Chem. Soc*., 1988, **110**, 1216.

[6] B. O'Regan, M. Grätzel, *Nature,* 1991, **353**, 737.

[7] M. K. Nazeeruddin, A. Kay, I. Rodicio, R. Humphry-Baker, E. Müller, P. Liska, N. Vlachopoulos and M. Grätzel, *J. Am. Chem. Soc.*, 1993, **115**, 6382.

[8] Y. Chiba, A. Islam, Y. Watanabe, R. Komiya, N. Koide, L. Han, *Jpn. J. Appl. Phys*., 2006, **45**, 638.

[9] F. Gao, Y. Wang, D. Shi, J. Zhang, M. Wang, X. Jing, R. Humphry-Baker, P. Wang, S. M. Zakeeruddin, M. Grätzel, *J. Am. Chem. Soc*., 2008, **130**, 10720.

[10] C. Chen, M. Wang, J. Li, N. Pootrakulchote, L. Alibabaei, C. Ngoc-le, JD. Decoppet, J.Tsai, C. Grätzel, C.Wu, SM. Zakeeruddin, M. Grätzel, *ACS Nano*, 2009, **3**, 3103.

[11] Y. Cao, Y. Bai, Q. Yu, Y. Cheng, S. Liu, D. Shi, F. Gao, P. Wang, *J Phys Chem C*, 2009, **113**, 6290.

[12] A. Yella, H.W. Lee, H.N. Tsao, C.Y. Yi, A.K. Chandiran, M.K. Nazeeruddin, E.W.G. Diau, C.Y. Yeh, S.M. Zakeeruddin, M. Grätzel, *Science*, 2011, **334**, 629.

[13] T. Trupke, P. Würfel, I. Uhlendorf, *J. Phys. Chem. B*, 2000, **104**, 11484.

[14] L. Han, N. Koide, Y. Chiba, T. Mitate, *Appl. Phys. Lett*., 2004, **84**, 2433.

[15] J. Halme, G. Boschloo, A. Hagfeldt, P. Lund, *J. Phys Chem C*, 2008, **112**, 5623.

[16] R.P. Barnes, A.Y. Anderson, S.E. Koops, J.R. Durrant, B.C. O'Regan, *J. Phys Chem C*, 2009, **113**, 1126.

[17] L. Zeng, Y. Yi, C. Hong, J. Liu, N. Feng, X. Duan, L.C. Kimerling, B.A. Alamariu, *Appl. Phys. Lett*., 2006, **89**, 1111111.

[18] P. Bermel, C. Luo, L. Zeng, L.C. Kimerling, J.D. Joannopoulos, *Opt. Express*, 2007, **15**, 16986.

[19] J.G. Mutitu, S. Shi, C. Chen, T. Creazzo, A. Barnett, C. Honsberg, D.W. Prather, *Opt. Express*, 2008, **16**, 15238.

[20] J. Zhu, C.M. Hsu, Z. Yu, S. Fan, Y. Cui, *Nano Lett*., 2010, **10**, 1979.

[21] D. Ko, J.R. Tumbleston, A. Gadisa, M. Aryal, Y. Liu, R. Lopez, E.T. Samulski, *J. Mater. Chem*., 2011, **21**, 16293.

[22] A.P. Kulkarni, K.M. Noone, K. Munechika, S.R. Guyer, D.S.Ginger, *Nano Let*., 2010, **10**, 1501.

[23] S.A. Haque, E. Palomares, B.M. Cho, A.N.M Green, N. Hirata, D.R. Klug, J.R. Durrant, *J. Am. Chem. Soc*., 2005, **127**, 3456.

[24] A. Usami, *Chem. Phys. Lett.*, 1997, **277**, 105.

[25] J. Ferber, J. Luther, *Sol. Energy Mater. Sol. Cells*, 1998, **54**, 265.

[26] H. C. van de Hulst, Light Scattering by Small Particles, Wiley, New York 1957.

[27] A. Usami, *Sol. Energy Mater. Sol. Cells*, 1999, **59**, 163.

[28] G. Rothenberger, P. Comte and M. Gratzel, *Sol. Energy Mater. Sol. Cells*, 1999, **58**, 321.

[29] A. Usami, *Sol. Energy Mater. Sol. Cells*, 2000, **64**, 73.

[30] W.E. Vargas, G.A. Niklasson, *Sol. Energy Mater. Sol. Cells*, 2001, **69**, 147.

[31] Y. Tachibana, K. Hara, K. Sayama, H. Arakawa, *Chem. Mater*., 2002, **14**, 2527.

[32] F. E. Galvez, E. Kemppainen, H. Miguez and J. Halme, *J. Phys. Chem. C*, 2012, **116**, 11426.

[33] Z. S. Wang, H. Kawauchi, T. Kashima and H. Arakawa, *Coord. Chem. Rev.*, 2004, **248**, 1381.

[34] S. Hore, C. Vetter, R. Kern, H. Smit and A. Hinsch, *Sol. Energy Mater. Sol. Cells*, 2006, **90**, 1176.

[35] H. J. Koo, J. Park, B. Yoo, K. Yoo, K. Kim and N. G. Park, *Inorg. Chim. Acta*, 2008, **361**, 677.

[36] W.Shao, F. Gu, L. Gai, C. Li, *Chem. Comm.*, 2011, **47**, 5046.

[37] S. Hore, P. Nitz, C. Vetter, C. Prahl, M. Niggemann, R. Kern, *Chem. Commun.*, 2005, 2011.

[38] B. Tan, Y.Y. Wu, *J. Phys. Chem. B*, 2006, **110**, 15932.

[39] C. J. Lin, W. Y. Yu, S. H. Chien, *Appl. Phys. Lett.*, 2007, **91**, 233120.

[40] L. H. Hu, S. Y. Dai, J. Weng, S. F. Xiao, Y. F. Sui, Y. Huang, S. H. Chen, F. T. Kong, X. Pan, L. Y. Liang, K. J. Wang*, J. Phys. Chem. B*, 2007, **111**, 358.

[41] L. Yang, Y. Lin, J.G. Jia, X.R. Xiao, X.P. Li, X.W. Zhou, *J. Power Sources*, 2008, **182**, 370.

[42] H. koo, Y.J. Kim, Y.H. Lee, W. I. Lee, K.Kim, N. Park, *Adv. Mater.*, 2008, **20**, 195.

[43] D.H. Chen, F.Z. Huang, Y.B. Cheng, R.A. Caruso, *Adv. Mat.*, 2009, **21**, 2206.

[44] Y.J. Kim, M.H. Lee, H.J. Kim, G. Lim, Y.S. Choi, N.G. Park, K. Kim, W.I. Lee*, Adv. Mat.*, 2009, **21**, 3668.

[45] W.G. Yang, F.R. Wan, Q.W. Chen, J.J. Li, D.S. Xu*, J. Mater. Chem.*, 2010, **20**, 2870.

[46] D. Derkacs, S. H. Lim, P. Matheu, W. Mar, E. T. Yu*, Appl. Phys. Lett.*, 2006, **89**, 093103.

[47] V.E. Ferry , M.A. Verschuuren , H.B.T. Li , E. Verhagen , R.J. Walters , R.E.I. Schropp , H.A. Atwater , A. Polman, *Opt. Express* 2010 , **18** , A237.

[48] K. Nakayama , K. Tanabe , H. A. Atwater , *Appl. Phys. Lett*. 2008, **93**, 121904.

[49] A.J. Morfa , K.L. Rowlen , T.H. Reilly , M.J. Romero , J v.d. Lagemaat , *Appl. Phys. Lett*. 2008, **92**, 013504 .

[50] K. Tvingstedt , N.K. Persson , O. Inganas , A. Rahachou , I. V. Zozoulenko, *Appl. Phys. Lett.* 2007, **91**, 113514 .

[51] K.R. Catchpole, A. Polman, *Opt. Express,* 2008, **16**, 21793.

[52] I.K. Ding, N. Tetreault, J. Brillet, B. E. Hardin, E.H. Smith, S.J. Rosenthal, F. Sauvage, M. Gratzel, M.D. McGehee, *Adv. Funct. Mater*. 2009, **19**, 2431.

[53] H.A. Atwater, A. Polman, *Nat. Mater.*, 2010, **9**, 205.

[54] S. Pan, L.J. Rothberg, *J. Am. Chem. Soc*. 2005, **127**, 6087.

[55] M. Ihara, K. Tanaka, K. Sakaki, I. Honma, K. Yamada,. *J. Phys. Chem. B* 1997, **101**, 5153.

[56] S.D. Standridge, G.C. Schatz, J.T. Hupp, *Langmuir* 2009, **25**, 2596.

[57] S. Standridge, G. Schatz, J. Hupp*, J. Am. Chem. Soc*. 2009, **131**, 8407.

[58] M.D. Brown, T. Suteewong, R.S.S. Kumar, V. D'Innocenzo, A. Petrozza, M.M. Lee, U. Wiesner, H.J. Snaith, *Nano Lett.*, 2011, **11**, 438.

[59] J. Qi, X. Dang, P.T. Hammond, A.M. Belcher, *ACS Nano*, 2011, **5**, 7108.

[60] H. Choi, W.T. Chen, P.V. Kamat, *ACS Nano*, 2012, **6**, 4418.

[61] L. Zheng, P. Bermel, Y. Yi, B.A. Alamariu, K.A. Broderick, J. Liu, C. Hong, X. Duan, J, Joannopoulos, L.C. Kimerling*, Apl. Phys. Let.*, 2008, **93**, 221105.

[62] R. Dewan, D. Knipp, *J. Appl. Phys.*, 2009, **106**, 74901.

[63] J. Kim , J. K. Koh , B. Kim , J. H. Kim , E. Kim , *Angew. Chem. Int. Ed,.* 2012 , **51** , 6864 .

[64] S. Wooh, H. Yoon, JH. Jung, YG. Lee, J.H. Koh, B.Lee, Y.S. Kang, K. Char, *Adv. Mat.*, 2013, **25**, 3111.

[65] A. Baba, K. Wakatsuki, K. Shinbo, K. Kato, F. Kaneko, *J. Mater. Chem.,* 2011, **21**, 16436.

[66] I. K. Ding, J. Zhu, W. Cai, S.-J. Moon, N. Cai, P. Wang, S. M. Zakeeruddin, M. Grätzel, M. L. Brongersma, Y. Cui,M. D. McGehee, *Adv. Energy Mater.*, 2011, **1**, 52.

[67] J.D. Joannopoulos, R.D. Meade, J. N. Winn, *Photonic Crystals: Molding the Flow of Light*; Princeton University Press, 0691-03744-2, 1995, Princeton, NJ, USA.

[68] S. Nishimura, N. Abrams, B.A. Lewis, L.I. Halaoui, T.E. Mallouk, K.D. Benkstein, J. van de Lagemaat, A.J. Frank, *J. Am. Chem. Soc.*, 2003, **125**, 6306.

[69] L.I. Halaoui, N.M. Abrams, T. Mallouk, *J. Phys Chem B*, 2005, **109**, 6334.

[70] A. Mihi, H. Míguez, *J. Phys. Chem. B*, 2005, **109**, 15968.

[71] A. Mihi, M.E. Calvo, J.A. Anta, H. Míguez, (2008). *Journal of Physical Chemistry C,* **112**, 13-17.

[72] S. Guldin, S. Huttner, M. Kolle, M. E. Welland, P. Mueller-Buschbaum, R. H. Friend, U. Steiner, N. Tetreault, *Nano Lett*, 2010, **10**, 2303.

[73] A. Mihi, F.J. López-Alcaraz, H. Míguez, *Appl. Phys. Lett.*, 2006, **88**, 193110.

[74] S. Colodrero, M. Ocaña, H. Miguez, *Langmuir, **24***, 2008, 4430.

[75] S. Colodrero, A. Mihi, L. Haggman, M. Ocaña, G. Boschloo, A. Hagfeldt, H. Míguez, *Adv. Mat.,* 2009, **21**, 764.

[76] A. Yariv, P. Yeh. "Optical Waves in Crystals", 2003, John Wiley and Sons Inc., ISBN 0-471-43081-1.

[77] S. Colodrero, A. Mihi, J. A. Anta, M. Ocaña, H. Miguez, *J. Phys. Chem. C,* 2009, ***113***, 1150.

[78] G. Lozano, S. Colodrero, O. Caulier, M. E. Calvo, H. Miguez, *J. Phys. Chem. C,* 2010, ***114***, 3681.

Chapter 2

Highly Porous Nanoparticle based One Dimensional Photonic Crystals

1. Introduction

Light harvesting strategies based on the use of properly engineered photonic nanostructures to improve solar to electric energy conversion of Dye Solar Cells (DSCs) have demonstrated.[1-4] In this context, S. Colodrero et al. proposed the integration of nanoparticle one dimensional photonic crystals (1DPCs) as light management structures in 2009.[5] Such Bragg reflectors were built by an alternating sequence of layers of amorphous SiO_2 and nanocrystalline TiO_2 nanoparticles, giving rise to a porous network mainly determined by both the degree of aggregation and the individual particle size of the precursor suspensions, [6,7] which allows the electrolyte flow through the entire multilayer. In this cell scheme, photons unharvested reach the photonic structure and they are specularly reflected back to the dyed electrode, increasing their probability to be absorbed. However, the experimental power conversion efficiency (η) increment obtained was lower than it was theorically expected.[8] This difference might be explained by the lower open circuit photovoltage (V_{OC}) and fill factor (ff) attained when using the photonic crystal as scattering layer, which indicated possible electrolyte diffusion problems through its pore network.

One way to optimize the electrolyte flow is to create a more open interconnected network into the photonic structure to reduce the mass diffusion resistance through it. One simple and facile route reported to create large cavities in thin films is that of using pore generated additives (denoted as porogens) dispersed within a matrix containing the precursor material.[9,10] Pores are then the result of volatilizing the sacrificial template at high temperature. Based on that, polyethylene glycol 20000 (PEG) will be used as porogen to improve the porosity of nanoparticle based 1DPCs. In the present chapter, a complete analysis of the effect the incorporation of different quantities of this polymer has on the structural, optical and diffusion properties of the 1DPC under study will be reported. We will find that this method allows controlling both the degree of porosity and the pore size distribution of TiO_2 (np-TiO_2) and SiO_2 nanoparticle (np-SiO_2) layers preserving the optical quality of the multilayered structure. Furthermore, in these newly designed nanoparticle based 1DPCs of increased porosity a reduction of the mass diffusion resistance of above 40% with respect to the standard one will be obtained.

Finally, it will be demonstrated that by coupling these new highly porous 1DPCs to working electrodes of dye solar cells (DSCs) an increase in photocurrent and power conversion efficiency is achieved in comparison with the original 1DPC-based cell, as a result of enhanced mass transport through these optical structures.

Results corresponding to the publication entitled "*Enhanced diffusion through porous nanoparticle optical multilayers*"[11] which has been included in the final list of papers, will be discussed.

2. Preparation of Nanoparticle based Monolayer and Multilayer Films

In this section, the method to stack np-TiO_2 and np-SiO_2 layers as mesostructured Bragg reflectors will be presented, as well as the route followed to tune their pore size distribution.

2.1. Preparation of nanoparticle precursor suspensions

SiO_2 and TiO_2 have been two of the preferred materials to build highly reflecting dielectric mirrors since they present very different refractive indexes, so an intense and broadband reflectance peak can be attained just with a few alternate layers in the stack.[12]

The starting materials considered for the construction of porous monolayers and multilayers were suspensions of SiO_2 and TiO_2 nanoparticles. The structure of layers in which the morphology of these nanoparticles can be appreciated is shown in figure 2.1. SiO_2 nanocolloids (average size of 30 nm) were purchased from Dupont (LUDOX TMA, Aldrich), while TiO_2 nanocrystallites (average size of 10 nm) were synthesized by using a procedure report by Burnside et al. based on the hydrolysis of titanium tetraisopropoxide followed by a peptization process under hydrothermal conditions,[13] which was slightly modified as it is described in what follows. Titanium tetraisopropoxide (20 ml, Aldrich 97 %) was hydrolized after the addiction to Milli-Q water (36 ml) and stirring for 1 hour. Once this stage was completed, the product was filtered through a 1.2 μm RTTP Millipores membrane and washed several times with distilled water to collect the solid formed. Then, it was peptized in a Teflon reactor containing 3.9 ml of an aqueous solution (0.6 M) of tetramethylammonium hydroxide (2.8 M, Fluka) at 120 °C for 3 h. After this, a colloidal suspension of titanium oxide crystallites with anatase structure was obtained. Later centrifugation at 14 000 rpm for 10 minutes allows elimination of some large aggregates from the dispersion, the concentration of the resultant suspension being typically between 24 and 25 wt%. Dynamic light scattering analysis yields an average particle size centred on 5-10 nm. TiO_2 and SiO_2 nanoparticles were diluted in a mixture of water, 21 vol%, and methanol, 79 vol%, in order to prepare the precursors dispersion employed for the deposition process. This alcohol was chosen because no coagulation is observed,[14] and the same time the medium is volatile enough to evaporate quickly. Prior to their deposition each suspension was ultrasonicated for several minutes to re-disperse aggregates.

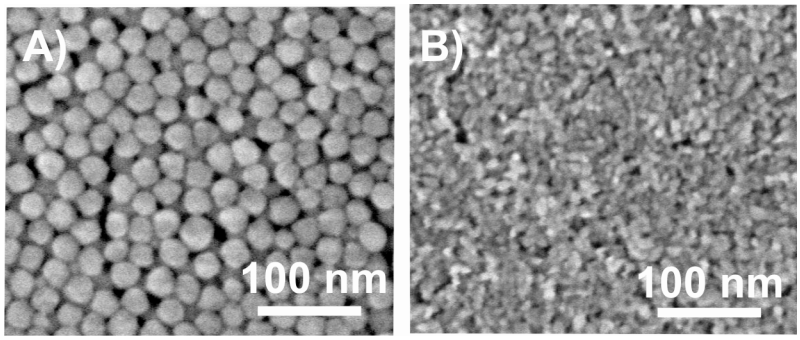

Figure 2.1. *FESEM images showing the morphology of (A) SiO_2 and (B) TiO_2 nanoparticles after being deposited onto a substrate.*

To modify the porous network of the SiO_2 and TiO_2 layers, a controlled amount of a polymeric porogen was mixed with the precursor suspensions of these nanoparticles before their deposition. The polymer chosen was polyethylene glycol 20000 (PEG) because it exhibits good film forming properties, and reduces the density of defects present in the film made by spin-coating.[15] It should be mentioned that there are other methods that allow controlling the porosity of nanocrystalline TiO_2 films, which involve the synthesis of particles within polyelectrolyte multilayers.[16] Also, the increase of particle size to enlarge the average pore size was discarded since it could give rise to unwanted diffuse scattering, as it has been proven before.[17] To study the influence that the addition of PEG to the TiO_2 and SiO_2 precursor suspensions has on the mesostructure of these nanoparticle Bragg reflectors, different PEG : nanoparticle weight ratios ranging from 0 to 0.75 were employed.

2.2. Film deposition method

The procedure employed to build TiO_2 and SiO_2 nanoparticle films herein presented was spin coating. This method consists on the deposition of an excess amount of a nanoparticle precursor suspension on the substrate chosen, which is then rotated at high velocity. During the formation of the layer, several steps can be distinguished: deposition and spin up, spin off and film drying, figure 2.2 outlines this procedure.

The first one takes place during the acceleration ramp, γ, in this stage the majority of excess suspension is spread out like big drops due to centrifugal forces until to the sample reaches the final speed rotation, ω. The followed

phase occurs at constant speed. In this step, the film is thinned as the result of the combination of convection and solvent evaporation. This later phenomena is produced in the whole process but takes more importance at the final stage of the film formation, when the viscosity of the liquid is higher and thinning due to spreading is hindered. In the final step, fluid flow has essentially stopped and further shrinkage of the film arises from solvent evaporation until a dry film is obtained. By repeating this cycle, it is possible to grow multilayer structures in which each films was created by packing nanoparticles of different composition. To obtain uniform films an acceleration ramp and a final rotation speed suitable have to be employed. In previous work[18], the relationship between the spin coating parameters, such as final rotation speed and acceleration ramp, and the uniformity of nanoparticle based films obtained by spinning process were exhaustively analyzed, and it was found that the optimum conditions are high acceleration ramp, to decrease the formation of comets (abrupt disruptions of the film uniformity caused by the presence of large particle aggregates), and rotation speed higher than 3000 rpm, to achieve good uniformity of the layer.

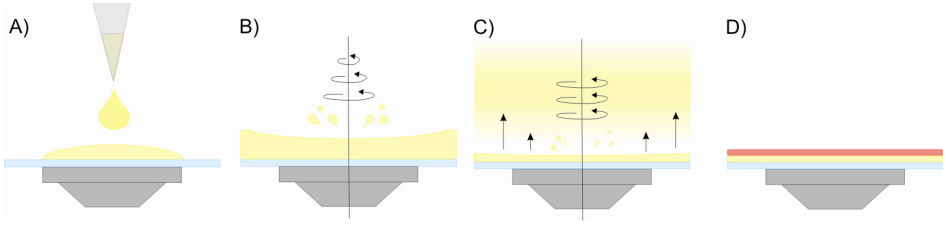

Figure 2.2. *Description of the spin coating process. A) Deposition of the precursor suspension on the substrate. B) Acceleration ramp. In this phase the excess amount of suspension is removed and the film begins to slim. C) Rotation at constant speed. The slimming continues, the evaporation of the solvent becomes the main factor in the formation of the film. D) Stacked films by spin coating deposition.*

Both np-TiO_2 and np-SiO_2 films and np-TiO_2/np-SiO_2 stacks with 1DPC properties employed in this work were built by the deposition of the diluted TiO_2 and SiO_2 suspensions using a spin coater (Laurell WS-400E-6NP), in which the final speed, ω, was 5000 rpm, and the acceleration ramp, γ, 9180 $rpms^{-1}$. The total process was completed in 60 s. The substrates used to deposit monolayers and multilayers were silicon and glass, respectively. Both substrates were previously treated to enhance their hydrophilicity and, consequently, improve the first layer deposition.

2.3. Thermal annealing

In order to build the films using the np-SiO_2/PEG and the np-TiO_2/PEG precursor suspensions, we also employed the spin coating protocol described above, although in this case it was necessary to stabilize them thermally after each layer was deposited. This heat treatment was performed on a hot plate at 300 °C for 15 minutes in air after each deposition to eliminate the pore polymer porogene from the structure. Without this intermediate treatment, it was not possible to create a new layer on top, since the newly deposited film did not adhere properly. To monitor the process of PEG removal, we performed a thermogravimetric analysis of both the np-TiO_2 and the np-TiO_2/PEG layers. Curves of weight loss versus temperature are drawn in Figure 2.3. An abrupt loss was observed at 300 °C for the np-TiO_2/PEG layer resulting from the deposition of the precursor suspension containing the np-TiO_2 : PEG weight ratio of 1:0.5, which was absent in the curve of the np-TiO_2 layer. This is the temperature at which thermal degradation of PEG starts, hence the weight drop measured can be associated to the elimination of the polymer from the np-TiO_2 matrix. A much less significant gradual loss is observed in the case of the np-TiO_2 layer used as reference, and it can be attributed to the removal of water and the organic capping agents of the nanocrystals, which must be also present in the np-TiO_2/PEG layers. Thereby, it was confirmed that after heating at 300 °C during 15 min all PEG present in both the films has been removed. Finally, all samples were annealed at 450 °C with heating rate of 15°C/min for 30 min in air. Moreover, this treatment provides the films with mechanical stability, as it favours nanoparticle sintering and removes organic remains.

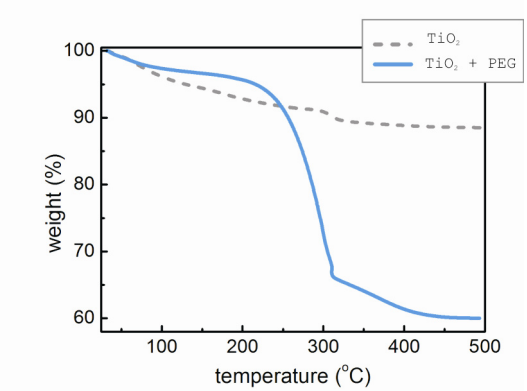

Figure 2.3. *Thermogravimetric analysis of a np-TiO_2 packing (grey dashed line) and the same nanocrystals mixed with 50% of PEG with respect to the TiO2 weight (blue solid line).*

3. Characterization

In this section, experimental details of the characterization of the nanoparticle structures will be presented.

3.1. Pore Size Distribution and Porosity Characterization

To carry out this characterization a new optical technique was developed in my research group called *Specular Reflectance Porosimetry (SRP),* which is based on the analysis on the specular reflectance spectra of thin films when such layers are exposed to different concentrations of a volatile solvent.[19] A further description of this technique is presented in the appendix 1.

3.2. Optical Properties

In order to check the dependence of the quality of the photonic crystal built by stacking highly porous SiO_2 and TiO_2 layers, an optical study was performed by measuring and analyzing the reflectance spectra that were taken using a Fourier Transform infrared spectrophotometer (Bruker IFS-66 FTIR) attached to a microscope and operating in reflection mode with a 4X objective with 0.1 of numerical aperture (light cone angle ±5.7º). Transmittance and total reflectance spectra were performed using an ultraviolet-visible scanning

spectrophotometer (SHIMADZU UV-2101PC). All the optical spectra presented in this thesis were carried out using these spectrophotometers operating under the conditions described in this section.

4. Analysis of Highly Porous Films by Specular Reflectance Porosimetry

Prior to the fabrication of the highly porous 1DPCs, a study of the porosity of the nanoparticle layers forming such structures (np-TiO_2 and np-SiO_2) was realized by Specular Reflectance Porosimetry. Firstly, the degree of porosity was extracted from the specular reflectance spectra from the np-TiO_2/PEG and np-SiO_2/PEG at vacuum (P_0=0.06 Torr), taken as the refractive index of the material composing the pore wall n_{SiO2}=1.45 or n_{TiO2}=2.4, this result is summed in Table 2.1. As it is presented in this table, as the PEG : np-TiO_2 weight ratios increase from 0 to 0.75 the effective refractive index decreases from 1.7 to 1.5, which implies that the accessible porosity of this layers rises from 47 to 60%. In the case of SiO_2 films, the refractive index varies from an already low 1.25 to 1.22 when the PEG : np-SiO_2 weight ratio is 0.50, with the porosity changing from 44% to 50%.

On the other hand, the response of these nanoparticle films *versus* the gradual increase of the vapor pressure of isopropanol provide us with the optical isotherms, these curves are shown in figure 2.5 and figure 2.6. Noteworthy, all adsorption–desorption isotherms measured can be classified as type IV,[20,21] following a standard classification of the capillary condensation response of mesoporous materials (pore size between 2 and 50 nm). This type of isotherms present a rounded knee at lower pressure region, which indicates the formation of a monolayer of solvent on the wall of the solid, a low slope region in middle of the curve as the solvent layer increases and at high partial pressures, the hysteresis loop as the result of the pore filling and emptying.

Material	PEG:np (wt %)	n_{eff} monolayer	Porosity (%) monolayer	n_{eff} of np-film in multilayer	Porosity (%) of np-film in multilayer
TiO_2	----	1.70	47	1.69	47
	25	1.58	55	1.59	54
	50	1.55	57	1.54	57
	75	1.49	60	1.49	60
SiO_2	----	1.25	44	1.27	42
	50	1.22	50	1.22	50

Table 2.1. *Refractive index and porosity of the different nanoparticle monolayers and multilayers, as estimated from the analysis of the optical reflectance*

The reversible behaviour of this sort of isotherm is the result of different facts such as pore geometry, the presence of blocked pores, changes of the contact angle with the bubble radius in the interface solid-liquid-vapor, the effect of the liquid surface tension, roughness in the solid surface, loss of the solid shape… to describe the hysteresis loop considering all these factors is a complicated task. Here, we only consider the pore size and geometry as the most revelant contribution to the sorption behaviour of the multilayer isotherms. We can consider, as a first approximation, a porous solid composed by spherical nanoparticles in some form of close-packing to explain the origin of the hysteresis observed. In the scheme drawing in Figure 2.4, condensation begins by the absorbed molecules at the contact point between adjancent spheres, forming a torus of liquid, which continues growing as the pressure increases until coalescence between neighbouring torus. At a certain vapor pressure, the cavities of radius r_c suddenly fills up. Then the absorption branch of the isotherm give information about the size of the radius of the inner cavity between spheres (r_c). However, the gas desorption process is conditioned by the smallest-possible space that the gas has to jump to leave the solid. This distance corresponds to the radius of a circle inscribed in the windows between spheres (r_w).

This model based on the sorption behaviour of packed spheres is very similar to the SiO_2 nanospheres based film analyzed in the present chapter, nevertheless, this approach can be also applied to explain the isotherm

measured from the TiO_2 films despite the its shape is not spherical, because the absorption and desorption mechanisms are limited by two types of pores.

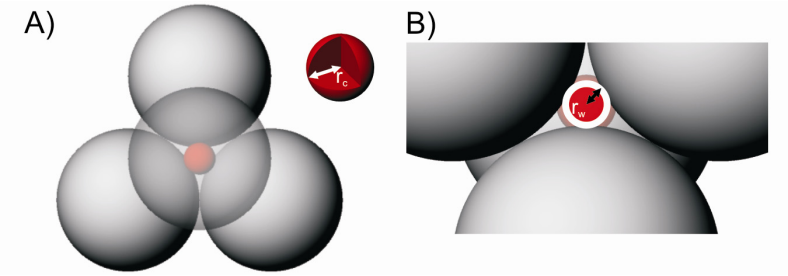

Figure 2.4. Model of pore filling and pore empty for a spherical nanoparticle based layer.

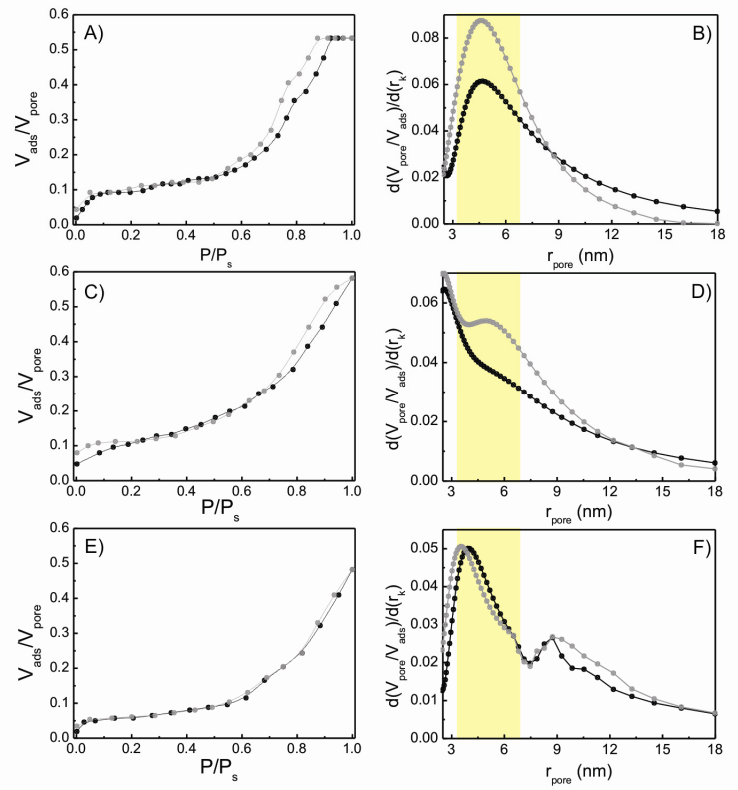

Figure.2.5. Adsorption (black circles and lines) and desorption (grey circles and lines) isotherms and pore size distribution measured by specular reflectance porosimetry from uniform monolayers made of (A and B) np-TiO_2 and np-TiO_2/PEG mixtures in which the weight ratio between the porogen and the nanoparticles is (C and D) 25% and (E and F) 50%. The yellow region signs the size of the pore created when np-TiO_2 are stacked.

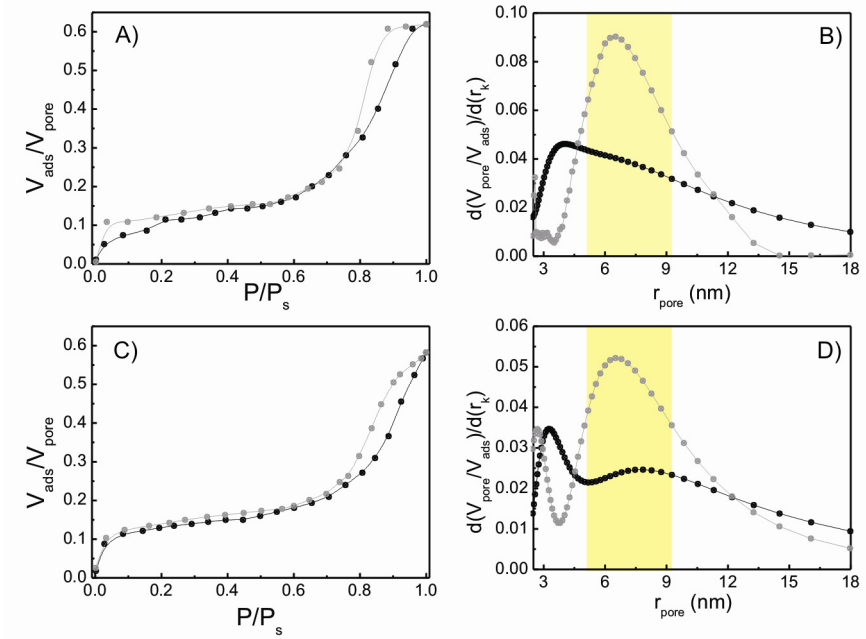

Figure.2.6. *Adsorption (black circles and lines) and desorption (grey circles and lines) isotherms and pore size distribution measured by specular reflectance porosimetry from uniform monolayers made of (A and B) np- SiO_2 and (C and D) np-SiO_2/PEG mixtures in which the weight ratio between the porogen and the nanoparticles is 50%. The yellow region signs the size of the pore created when np-SiO_2 are stacked.*

By analyzing the isotherm curves attained from the np-TiO_2 layer (Figure 2.5.A) by the SRP technique it can be observed that the volume of solvent infiltrated within the structure increases as the pressure goes up to a specific value of $P/P_s = 0.93$, where P_s is the saturation vapor pressure of isopropanol at room temperature, with the filled pore volume remaining constant for higher pressures. This fact indicates that the accessible porosity of the layer is completely filled with the solvent employed. However, this trend is not observed for the case of the isotherms measured from the layers in which PEG is used to change their internal porous structure of the TiO_2 film (Figure 2.5.C and 2.5.E), which is in consonance with the expected effect of the porogen on the mesostructure, namely, the creation of large cavities in which condensation of the vapor is prevented. Besides, as the porogen amount mixed with the TiO_2 precursor suspension increases, the hysteresis loop is lost, which means that r_w (radio of the window between adjacent spheres, please see figure 2.4) increases, opening the whole porous network. Pore size distributions (PSD) of the

different np-TiO_2 and np-TiO_2/PEG films are extracted from the isotherm data, as it is explained in appendix 1. They are presented in Figure 2.5.B, 2.5.D and 2.5.F. Please notice that the np-TiO_2 PSD is calculated from the 55% of the void volume of the sample, which means that internal pores higher than 20 nm and isolated pores cannot be characterized by SRP technique. This percentage increases when PEG is used to modify the porosity, mainly due to the more open interconnectivity. On the other hand, as it can be seen in the pore size distribution of these films, the TiO_2 packing obtained from the nanoparticles deposited by spin coating gives rise to an average pore radius of 5 nm. There is still a maximum of the PSD curve at this pore size when PEG is mixed with the suspension. However, as the amount of this polymer increases new pores of size higher than 7.5 nm are created after removing it. Pore size distributions demonstrate that both the porosity and the average pore size are increased when PEG is used as porogen. Similarly, adsorption–desorption isotherms and pore size distributions of both np-SiO_2 and np-SiO_2/PEG layers are shown in Figure 2.6. In this case, the most noteworthy difference is the increase of the radius of necks between nanoparticles of the sample when PEG is used, as it can be seen when Figure 2.6.B and 2.6.D (grey circles and lines) are compared. Also, the pore size distribution becomes wider and the average pore size shifts towards higher values. As expected, since layers formed by SiO_2 nanoparticles have larger pores than TiO_2 films to start with, the effect of porogen on the SiO_2 pore size is less noticeable, although in both types of layers the porosity rises with the concentration of porogen used in the precursor suspensions. Hence more effort was devoted to improve the pore network of the TiO_2 layer since the bottleneck for optimized electrolyte flow must be the narrowest pores of the multilayer, present in the np-TiO_2 layers.

5. Highly Porous Layers in Bragg Reflectors

Having demonstrated that both the porosity and the average pore size of np-TiO_2 and np-SiO_2 films are increased when PEG is added to the precursor suspensions, 1DPCs were built in order to prove that these new highly porous layers can also be piled up to form photonic crystals. For that purpose, np-SiO_2 and np-TiO_2 precursor suspensions with different concentration of PEG were employed. Field-emission scanning electron microscope (FESEM, Hitachi S-4800 operating at 2 kV) images of cross-sections of multilayers made by alternating films deposited from these suspensions are shown in figure 2.7.

The samples whose images are displayed were prepared using suspensions containing PEG : np-TiO_2 weight ratios of 0 (Figure 2.7.A) and 0.75 (Figure 2.7.B), while the same np-SiO_2 suspension containing no PEG was used for both samples.

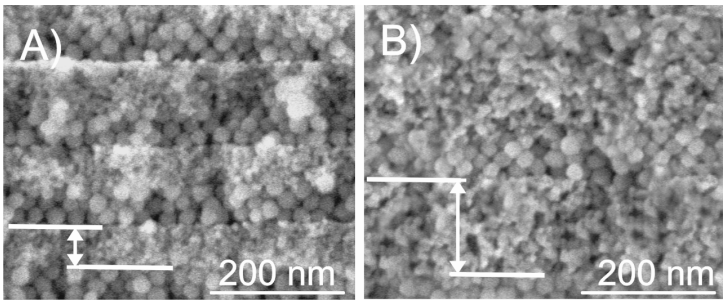

Figure 2.7. *FESEM images of cross-sections corresponding to Bragg reflectors made of alternate layers of spherical silica particles and titania nanocrystals. The latter was mixed with PEG in weight relations of (A) 0% and (B) 75% with respect to the weight of np-TiO_2 in the precursor suspension.*

The different porous structure of the TiO_2 layers can be clearly distinguished in these pictures. The clear definition between the interfaces of np-TiO_2 and np-SiO_2 layers presents in the originally made nanoparticle multilayers (Figure 2.7.A) fades when the polymer is used to modify the pore network (Figure 2.7.B), mainly due to the SiO_2 particle interpenetration within the large superficial pores of the TiO_2 layers. However, it is interesting to notice that the periodicity at long distances is preserved, which is fundamental to obtain a good optical response of the photonic crystal. Furthermore, it can be readily observed that the thickness of the TiO_2 layer also increases with the PEG concentration in the precursor suspension, thicknesses comprised between 60 nm and 130 nm being attained for PEG : np-TiO_2 weight ratios ranging from 0 to 0.75.

In the same way that it was done for monolayers, the values of the effective refractive index and the porosity of each layer within the periodic stack are also estimated minimizing the difference between the simulated and the experimental reflectance spectra and using the Bruggeman equation, respectively. In Figure 2.8, experimental reflectance spectra (grey solid line) and the corresponding theoretical fittings (blue dashed line) of an example of the newly designed PC are plotted. Table 2.1 summarizes the results obtained from these fittings. Interestingly, it can be seen that the porosity of both the np-

TiO_2 and np-SiO_2 layers remains practically unaltered after being integrated in the Bragg reflector when compared to that measured for monolayers. It should be also remarked that control over the porosity of the films, like the one herein demonstrated, opens the possibility of designing the optical properties of the multilayers built with them with great precision, as it has actually been proven for other optical filters in which porosity, although not accessible, can be tailored to measure.

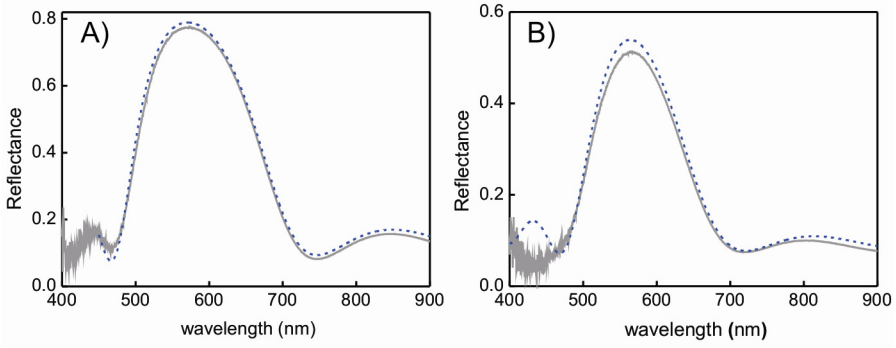

Figure 2.8. *Simulated (blue dashed line) and experimental (grey solid line) specular reflectance spectra of 1DPCs made using (a) np-TiO_2 and of (b) np-TiO_2: PEG. The latter was deposited from a precursor suspension containing a PEG weight relation of 50% with respect to that of np-TiO_2.*

To evaluate the influence that the new pore network structure may have on the control of the optical properties, 1DPCs of different porosity having their Bragg peaks located in the same spectral range in their reflectance spectra were built.

As it was explained in the introduction chapter, the Bragg peak of a 1DPC is centered at $\lambda_B = 2\Delta n_{eff}$, where Δ is the unit cell thickness and n_{eff} the effective refractive index of the structure. So, to built these photonic crystals the concentrations of TiO_2 and SiO_2 precursor suspensions have to be tuned for this end, since, as shown in Figure 2.7, the thickness of the layers is increased when the same concentrations of nanoparticles are mixed with increasing amounts of PEG. The specular reflectance spectra of these samples are displayed in Figure 2.9. The comparison between the different spectra reveals that the presence of larger pores does not affect adversely the performance of the multilayers as Bragg reflectors. In all cases, the number of layers deposited is similar (N = 10) and primary maxima present intensities above 80%. Slightly higher peaks are achieved for 1DPCs in which the pores are finer. The reason for this effect is

the lower refractive index contrast existing between the layers of np-TiO_2 and np-SiO_2 in those multilayers showing enhanced porosity, which diminishes the scattering strength of the lattice. Also, a clear narrowing of the peak spectral width is observed as the porosity increases. The photonic gap to midgap ratio, estimated as the ratio between the spectra full width at half maximum and the spectra position of such maximum in terms of frequency, $\Delta\omega/\omega_0$, decreases from 25% in the original nanoparticle 1DPC to 20% in those with higher porosity. In fact, it can be shown that $\Delta\omega/\omega_0$ depends on the dielectric contrast, $\Delta n = |n_1-n_2|$, like[22]

$$\Delta\omega/\omega_0 = \frac{2}{\pi}\frac{\Delta n}{\langle n\rangle} \qquad 2.1$$

The generation of a more open pore network yields both lower Δn and n, as it can be estimated from the data shown in Table 2.1.

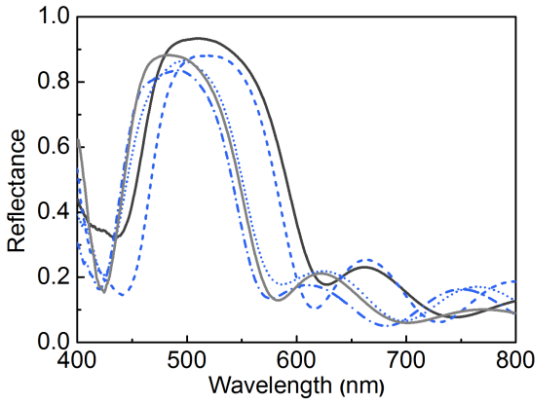

Figure 2.9. *Specular reflectance spectra of 1DPCs in which different weight ratios of PEG were added to the precursor suspensions, namely, 0% (black solid line), 25% in TiO_2 (blue dashed line), 50% in TiO_2 (blue dotted line), 75% in TiO_2 (blue dashed-dotted line) and 50% in TiO_2/50% in SiO_2 (light grey solid line) with respect to that of nanoparticles.*

6. Enhanced Diffusion through Bragg Reflectors

Once we probed that both the porosity and the pore size distribution of a nanoparticle layer can be improved by employing PEG as porogen to create large cavities inside the film, the effect that this more open network has on the mass transport was investigated by impedance spectroscopy measurements. This analysis was realized in collaboration with Professor Francisco Fabregat Santiago and Professor Juan Bisquert from Department de Física (Universitat Jaume I , Castelló, Spain).

4.1. Impedance Spectroscopy Measurements

The diffusion of a liquid through the modified pore network of nanoparticle based 1DPCs were evaluated by impedance spectroscopy measurements (IS). The photonic crystals analyzed were constructed of 4 unit cells, and the concentration of the precursor suspensions employed were adjusted in order to obtain the spectral position of the Bragg peak centered at 500 nm, as it is shown in Figure 9.

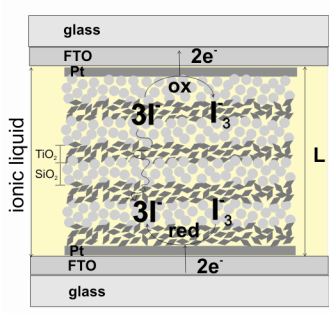

Figure 2.10. *Scheme of the sandwich cells measured in this study*

The IS measurements were performed in a two-electrode configuration containing 0.13 M iodine in 1-butyl-3-methylimidazolium iodide (Figure 2.10). Each cell was composed of two platinized FTO electrodes, one of them with an np-SiO_2/np-TiO_2 multilayer, for which different quantities of PEG were employed, deposited over the Pt-coated glass. An area of 1 x 1 cm^2 was drawn over conductive glass leaving a 2 mm wide strip on one of the sides to evacuate the charge and make the contacts. FTO out of this area was removed via etching with Zn powder and diluted HCl. Then the electrodes were electroplatinized by submerging them into a diluted chloroplatinic acid aqueous solution using a Pt sheet as a counter-electrode and applying a potential of 1.5 V for 1 minute. After this process, dark FTO electrodes were

obtained, indicating that a high concentration of Pt was deposited over the surface. The cells were mounted after drop casting the electrolyte in one of the electrodes and fixing the second by pressing it strongly with a clamp. Pressing electrodes together with a clamp ensures to reach a distance between electrodes equal to the photonic crystal thickness. The removal of external FTO avoids both short circuiting of the cells and direct diffusion of iodide between uncovered FTO layers, minimizing edge effects. The conductive strips of the opposed electrodes were oriented in contrary faces also to prevent short circuits. The iodine concentration used in the electrolyte is lower than that found in the literature because the short distance between electrodes makes it more difficult to reach the current saturation regime.[23] Furthermore, a pure ionic liquid was necessary in this experiment both to avoid evaporation during measurements and to be able to appreciate the differences in diffusion due to porosity. Electrochemical measurements were carried out in this sandwiched configuration and collected after letting the electrolyte penetrate into the pores of the nanoparticle 1DPC.

To assess the effect that the modified pore network of 1DPCs has on mass transport, curves of current density vs. potential (jV curves) between 0 and 1.5 V were measured to obtain the limiting currents reached as a function of the average pore size (Figure 11). As it can be seen, as the increase of the layer porosity and pore size with the addition of PEG produces a rise both in the slope at low potentials and in the value of the limiting current (j_{lim}) plateau of the jV curves. These results constitute the first evidence of enhancement of mass transport of an electrolyte embedded in 1DPC as a result of the control of porosity.

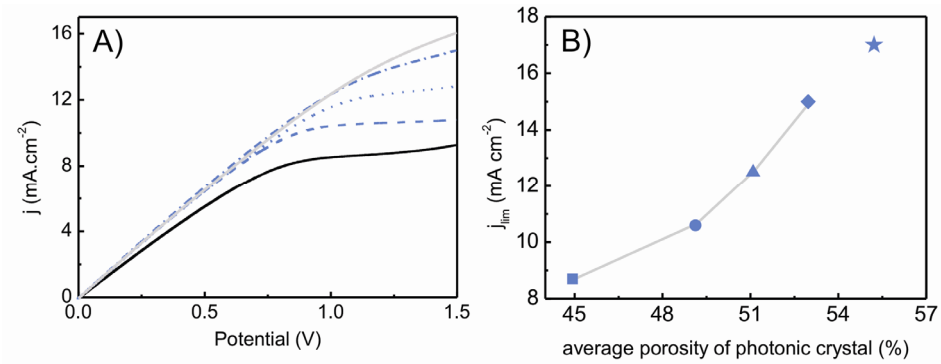

Figure 2.11. A) jV curves for the 1DPCs prepared from precursor suspensions containing different amounts of PEG in the np-TiO_2 layer: weight ratios of 0 (black solid line), 0.25

(blue dashed line), 0.5 (blue dotted line), and 0.75 (blue dashed-dotted line) while keeping the PEG : np-SiO_2 weight ratio constant and equal to 0. Results for a sample made using both PEG : np-TiO_2 and PEG : np-SiO2 weight ratios of 0.5 are also shown (solid grey line) and B) limit current obtained by extrapolating the values of the plateau on jV curves versus average porosity of the multilayer.

For a more detailed analysis of these results, each sample was measured by impedance spectroscopy at four different currents between 0 mA and the limiting current for each cell. An example of the Nyquist plots obtained from the porous 1DPC is shown in Figure 2.12.A. Within a very good approximation, these impedance spectra may be modeled by a standard Randles equivalent circuit, schematized in Figure 2.12.B. It allows analyzing separately the physical processes of carrier transport and charge transfer that take place in our device. The equivalent circuit elements have the following meaning:

- R_s is a series resistance accounting for the transport resistance associated with FTO, contacts and wires.
- R_{Pt} is the charge-transfer resistance at the platinized electrode/electrolyte interface.
- C_{Pt} is the double-layer capacitance from the platinized electrodes.
- Z_d is the diffusion impedance, which represents the resistance to mass transfer through the porous structure.

From the expression of Z_d given by Equation 2.6, where ω_d is the characteristic diffusion frequency in a finite layer, ω is the frequency of the measurement and i is the imaginary unit,

$$Z_d = R_d \frac{\tanh\left[(i\omega/\omega_d)^{1/2}\right]}{(i\omega/\omega_d)^{1/2}} \qquad 2.2$$

we obtain R_d, which is the resistance associated with diffusion of triiodide ions in the electrolyte and is the parameter that will be more affected by variations of the pore network in the multilayers.

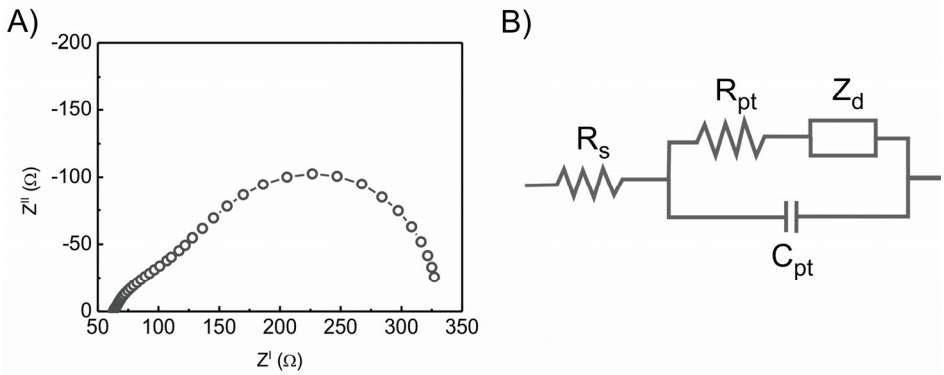

Figure 2.12. *A) Impedance spectrum of a device made by sandwiching a photonic crystal and the electrolyte solution between two platinized electrodes. Galvanostatic measurement was performed at 10 mA over a sample made with 25% PEG in np-TiO_2. B) Randles circuit used to fit experimental data.*

From the diffusion frequency and film thickness, L , the diffusion coefficient may be obtained using

$$D = \omega_d L^2 \qquad 2.3$$

that yielded values comprised between 1.5 and 2.5 x 10^{-8} cm^2 s^{-1}, in good agreement with data obtained from j_{lim} calculations.[24] These values are one order of magnitude lower than those obtained in the free electrolyte,[23] indicating certain difficulties in the transport of I^{3-} through the 1DPC. This result is presumable ascribable to the increased tortuosity and constrictivity introduced by the 1DPC relative to the free electrolyte. In practical terms, the diffusion resistance is the most relevant parameter of Z_d since its value determines, together with R_s and R_{Pt}, the total series resistance of the device. Thus it may influence the performance of the photo-electron, mainly through the loss of fill factor, but eventually also by a drop in short circuit current.[25,26] We thus focus our study on R_d in what follows.

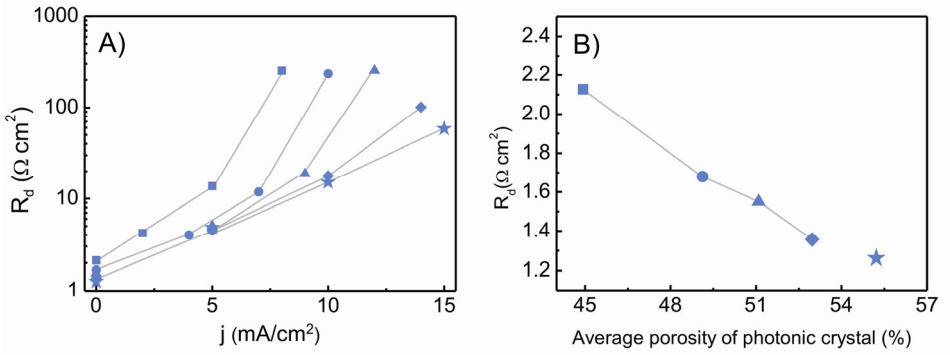

Figure 2.13. *A) Diffusion resistance (R_d) versus current density (j) as extracted from the impedance spectroscopy analysis. B) Diffusion resistance obtained at j = 0 mA versus average porosity of the 1DPC prepared using different PEG : np-TiO_2 weight ratios, namely, 0 (squares), 0.25 (circles), 0.5 (triangles), 0.75 (rhombus). Data for the multilayer prepared using both PEG : np-TiO2 and PEG : np-SiO2 weight ratios of 0.5 are also shown (stars).*

Figure 2.13.A displays R_d as obtained from the analysis of the impedance spectra measured at several current densities, j. The different symbols (lines are just guides for the eye) correspond to photonic crystals possessing different pore networks. In all cases, R_d increases as the current does, reaching rather large values when j_{lim} is approached. It can be readily seen from Figure 2.13.A that samples with higher porosity present lower diffusion resistance, reaching values similar to those commonly found in optimized devices for R_s (1–5Ω cm^2) and R_{Pt} (1–3 Ω cm^2).[26-29] Figure 2.16.B clearly shows the dependence of R_d measured at 0 mA *versus* the average porosity within the multilayer structure.

Again a clear decay of R_d as porosity is increased can be observed while, consequently, the opposite trend is observed for j_{lim}, as shown in Figure 2.11.B. It should also be noticed that this enhanced mass transport must be caused by the combined effect of both larger porosity and average pore size. However, these two effects cannot be analyzed separately: each time porosity is increased (see Table 2.1), the bottlenecks, responsible for the hindering of diffusion, are also enlarged, thus also contributing to a better flow of species through the multilayer. The observation of these properties leads us to foresee that these materials will present improved performance when integrated in photoelectrochemical devices.

7. Dye Solar Cell Based in Highly Porous 1DPC

After demonstrating that PEG allows tuning the porous structure of SiO_2 and TiO_2 nanoparticle films, and that these new open void network layers can be stacked displaying intense Bragg reflections as well as improved mass transport through them, we explored the effect of coupling the new designed porous 1DPCs to working electrodes of Dye Solar Cells, for which the enhancements are expected to be larger than the one obtained from original 1DPC-based DSC. It must be pointed out that the result herein presented were carried out in collaboration with the group of professor E. Palomares from the Electronic Materials and Devices Section (Institute of Chemical Research of Catalonia, ICIQ, Tarragona, Spain).

7.1. Preparation and Assembly of DSCs

The transparent TiO_2 photoelectrode is deposited on conducting glasses (Nippon Sheet Glass Co, 10 Ω cm^{-2}), which are first soaked into a 0.04 M $TiCl_4$ aqueous solution at 70 °C for 15 min and washed with ethanol. Dyesol paste (18NRT) was deposited by a screen printing method to obtain 5 μm TiO_2 films for a deposited active area of 0.16 cm^2. The resulting electrodes are gradually heated under airflow at 325 °C for 5min, 375 °C for 5 min, 450 °C for 15 min and 500 °C for 15 min. The heated electrodes are soaked again into a 0.04 M $TiCl_4$ aqueous solution at 70 °C for 15 min and then washed with ethanol and dried in air. In order to fabricate the 1DPC structure on such TiO_2 active layers, an alternated deposition of silica and titania nanoparticles by using a spin-coater is employed. Both nanoparticle precursors are suspended in a mixture of water (21 vol%) and methanol (79 vol%) using concentrations of 2 wt% SiO_2 and 4 wt% TiO_2, the latter containing a 2 wt% of PEG, and concentrations of 2 wt% SiO_2 and 5 wt% TiO_2 for the originally reported photonic crystal. For most cells, Bragg reflectors containing four SiO_2/TiO_2 repeated units are made using 150 μL drops of their respective colloidal suspensions. In this case, both the acceleration ramp and the final rotation speed are fixed at 9180 rpm s^{-1} and 5000 rpm, respectively. Because the spin-coated TiO_2 layers contain a certain amount of organic material incorporated in the dispersion, a thermal stabilization was necessary to avoid dissolving such layer after a subsequent deposition. This heat treatment is performed on a hot plate at 300 °C during 15 min and is repeated following every bilayer

(SiO_2/TiO_2) deposition during the multilayer structure formation. After that, all samples are annealed at 450 °C for 30 min to remove organic remains and mechanically stabilize the entire structure.

TiO_2 photoelectrodes are immersed into a 10^{-3} M C101 dye solution, (Na-cis-Ru(4,4'-(5-hexyltiophen-2-yl)-2,2'-bypyridine)(4-carboxylic-acid-4'-carboxylate-2,2'-bipyridine)(thiocyanate)(2), using as a solvent a mixture of acetonitrile:tert-butanol (1:1). The counter electrodes were made by spreading a drop of 5×10^{-3} M solution of H_2PtCl_6 in ethanol onto a conducting glass substrate and heated under air flow at 390 °C for 15 min. Both electrodes were sealed using a thermo-polymer (Surlyn). The cells were finally filled with the liquid electrolyte, Z960, through a hole made previously at the back of the platinized counter electrode. Then, the hole was sealed with a thermoplastic polymer and a glass cover slide.

7.2. Photovoltaic Characterization

The current-voltage (IV) curve measurements were carried out with a 150 W xenon lamp from ABET Instruments with the appropriate filter for the correct simulation of the 1.5 AM G solar spectrum. The incident light power was calibrated using a silicon photodiode previously calibrated at 1000 W m^{-2} at 1.5 AM G.

7.3. Performance of DSCs Coupled to 1DPCs of Enhanced Porosity

Figure 2.14 displays both a scheme and field emission scanning electron microscope images of a cross section of the dye solar cell employed to perform the experiments herein analyzed. The 1DPCs deposited onto the electrode act as a back reflector, which increases the time of residence of photons within the active layer of a specify wavelength range determined by the spectral width of the photonic band gap. In this way the photons residence time through the electrode (and thus the probability of being absorbed) is improved, which leads to the consequent higher photocurrent values. At the same time the interconnected porosity allows the liquid electrolyte flow through it.

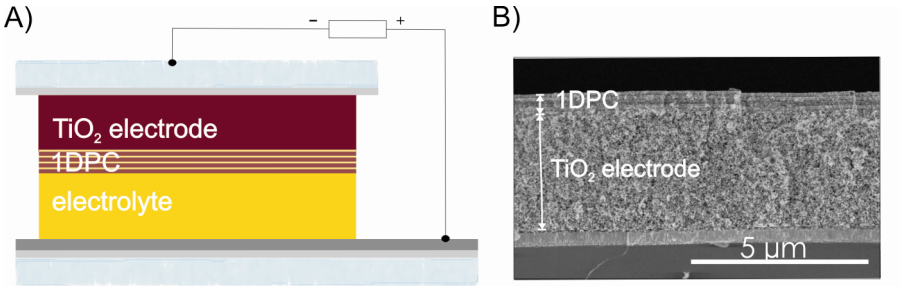

Figure 2.14. Design and structure of a DSC coupled to a porous nanoparticle-based 1DPC. A) Scheme of the solar cell based on the 1DPC. B) FESEM image showing a cross-section of a dye-sensitized nc-TiO2 electrode onto which a TiO2–SiO2 nanoparticle multilayer has been deposited.

Herein, the performance of DSCs is evaluated after the incorporation of several light reflector structures, namely standard and highly porous 1DPCs made of nanoparticles as well a reference cell without any photonic structure. Thereby, the effect over the device operation of the improved mass transport through the optical structure can be studied. The characteristic IV curves were measured from these cells and are presented in Figure 2.15.

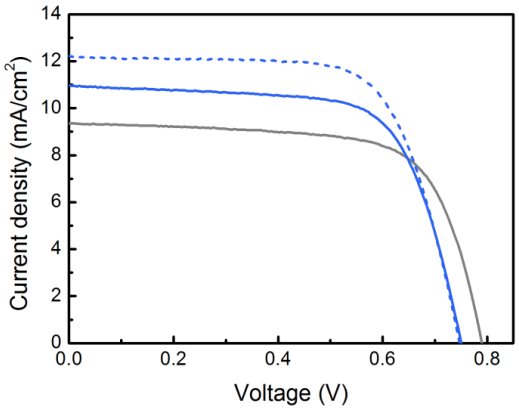

Figure 2.15. A) IV for DSSCs in which a 5 µm thick TiO_2 layer was coupled to a non-modified 1DPC (blue line), and a highly porous 1DPC (dashed blue line) and results corresponding to a reference cell (black solid line) are also plotted.

It can be easily concluded that the multilayer whose porous network has been modifyed by infiltration and after removal of PEG gives rise to a larger enhancement of the photocurrent. Power conversion efficiency (η) of the set of

cells was calculated from the IV curve displayed in figure 2.15 and listed in table 2.2 with the values of all relevant parameters obtained from this set of cells.

DSC	Jsc ($mAcm^{-2}$)	Voc (V)	ff (%)	η (%)
Reference DSC	9.35	0.79	69	5.10
PC based DSC	10.9	0.75	69	5.6
Highly porous PC based DSC	12.13	0.76	68	6.22

Table 2.2. *Values attained for the short circuit photocurrent density (J_{SC}), the open circuit photovoltage (V_{OC}), the fill factor (ff), and the power conversion efficiency (η) for the set of solar cells.*

As it was demonstrated in the section 6 of this chapter, the use and removal of PEG during the stacking of the optical multilayers give rise to a reduction of the diffusion resistance through these structures. This fact yields better performance of the cell in which they have been introduced. These results open the route to optimize the performance of photo-electro-chemical devices by means of interplay highly porous nanostructured photonic lattices.

8. Conclusions

A method for controlling the porosity of nanoparticle-based Bragg Reflectors through the addition of different concentration of polyethylene glycol to the precursor suspensions has been developed.

Bragg mirror with these new highly layers have been stack without losing the high optical quality of these assembles. At the same time, mass transport through the highly porous photonic crystal has been improved, as confirmed by impedance spectroscopy.

Higher power conversion efficiency has been observed coupling the new designed photonic crystal to the electrode of a Dye Solar Cell.

9. References

[1] S.Nishimura, N.Abrams, B. A. Lewis, L. I. Halaoui, T. E. Mallouk, K. D. Benkstein, J. van de Lagemaat, A.J. Frank, J. Am. Chem. Soc., 2003, 125, 6306.

[2] A. Mihi, M.E. Calvo, J.A. Anta, H. Míguez, *J. Phys. Chem. C*, 2008, **112**, 13.

[3] A. Mihi, C. Zhang, P. Braun, *Angw. Chem. Int. Ed*., 2011, **50**, 5712.

[4] C.T. Yip, H. Huang, L. Zhou, K. Xie, Y. Wang, T. Fenq, J. Li. W.Y. Tam*, Adv.Mater.*, 2011, **23**, 5624.

[5] S. Colodrero, A. Mihi, L. Häggman, M. Ocaña, G. Boschloo, A. Hagfeldt, H. Míguez, *Adv. Mat.*, 2009, **21**, 764.

[6] S. Colodrero, M. Ocaña and H. Míguez, Langmuir, 2008, **24**, 4430.

[7] M.E. Calvo, S. Colodrero, T.C. Rojas, J.A. Anta, M. Ocaña, H. Míguez, *Adv. Funct. Mater.*, 2008, **18**, 2708.

[8] G. Lozano, S. Colodrero, O. Caulier, M. E. Calvo, H. Miguez, *J. Phys. Chem. C,* 2010, **114**, 3681.

[9] M.V. Badiger, M.E. McNeill, N.B. Graham, *Biomaterials*, 1993, **14**, 1059.

[10] E. Della Gaspera, A. Antonello, M. Guglielmi, M.L. Post, V. Bello, G. Mattei, F. Romanato, A. Martucci, *J. Mater. Chem.*, 2011, **21**, 4293.

[11] C. López-López, S. Colodrero, S.R. Raga, H. Lindström, F. Fabregat-Santiago, J. Bisquert, H. Míguez, *J. Mater. Chem.,* 2012, **22**, 1751

[12] H.A. Macleod, Thin Film Optical Filters, 3rd Edition, 2001, Institute of Physics Publishing, London.

[13] S. D. Burnside, V. Shklover, C. Barbe, P. Comte, F. Arendse, K. Brooks, M. Grätzel, *Chem. Mater*., 1998, **10**, 2419.

[14] I. Thomas, *M. Appl. Opt*., 1987, **26**, 4688.

[15] D. P. Puzzo, L. D. Bonifacio, J. Oreopoulos, C. M. Yip, I. Manners and G. A. Ozin, J. *Mater. Chem*., 2009, **19**, 3500.

[16] M. Logar, B. Jancar and D. Suvorov, *J. Am. Ceram. Soc.*, 2010, **93**, 3679.

[17] T. Druffel, O. Buazza, M. Lattis, S. Farmer, M. Spencer, N. Mandzy and E. A. Grulke, *Proc. SPIE*, 2008, 7030, 300.

[18] M. E. Calvo, O. Sánchez-Sobrado, S. Colodrero, and H. Míguez, *Langmuir*, 2009, **25**, 2443.

[19] N. Hidalgo, C. López-López, G. Lozano, M E. Calvo, H. Míguez, *Langmuir*, 2012, 28, 13777.

[20] S. J. Gregg, K. S. W. Sing, Adsorption, Surface Area and Porosity; Harcourt Brace and Co.: Orlando, FL, 1997.

[21] S. Brunauer, L. S. Deming, W. S. Deming, E. Teller, J. Am. Chem. Soc. 1940, 62, 1723.

[22] A. Yariv and P. Yeh, Optical Waves in Crystals, John Wiley and Sons Inc., ISBN 0-471-43081-1, 2003.

[23] F. Fabregat-Santiago, J. Bisquert, E. Palomares, L. Otero, D. Kuang, S. M. Zakeeruddin and M. Grätzel, *J. Phys. Chem. C,* 2007, **111**, 6550.

[24] A. Hauch and A. Georg, *Electrochim. Acta*, 2001, **46**, 3457.

[25] F. Fabregat-Santiago, J. Bisquert, G. Garcia-Belmonte, G. Boschloo and A. Hagfeldt, *Sol. Energy Mater. Sol. Cells*, 2005, **87**, 117.

[26] F. Fabregat-Santiago, G. Garcia-Belmonte, I. Mora-Seró and J. Bisquert, *Phys. Chem. Chem. Phys.*, 2011, **13**, 9083.

[27] T. Hoshikawa, M. Yamada, R. Kikuchi and K. Eguchi, *J. Electrochem. Soc.*, 2005, **152**, E68.

[28] Y. Chiba, A. Islam, Y. Watanabe, R. Komiya, N. Koide and L. Han, *Jpn. J. Appl. Phys.*, 2006, **45**, L638.

[29] J. Liu, R. Li, X. Si, D. Zhou, Y. Shi, Y. Wang, X. Jing and P. Wang, *Energy Environ. Sci.*, 2010, **3**, 1924.

Chapter 3

Panchromatic Photonic Crystal for Efficient Transparent Dye Solar Cells

1. Introduction

The use of back diffuse scattering layers have become the most widespread technique to largely increase light harvesting efficiency in the field of dye solar cells (DSC)[1-5],but unfortunately this approach renders the cell completely opaque due to the lack of spectra selectivity of the multiple scattering phenomena.[6,7] Keeping in mind that transparency is probably the most attractive feature of these devices for building integration and outdoor applications,[8] the search for different approaches to provide much more efficient and stable solar cells while maintaining this asset continues being a major challenge in the field. Concerning this topic, optical designs based on photonic nanostructures that could overcome this drawback have been proposed,[9-14] but so far none of them show efficiency enhancements comparable to those attained with a packing of disordered submicrometric particles. Although, higher efficiencies could be reached by stacking PCs of different period, as it has been previously proposed and realized for 3DPCs,[15] which would also imply that thicker back mirrors are coupled to the absorbing electrode, no nanoparticle multilayers presenting highly reflections covering the whole visible range had been reported up to this work. Experimentally, the

fact that difficults the realization of these panchromatic back reflectors coupled to electrodes of DSCs was the increased of the diffusion resistance of the electrolyte within the cell, since thicker unit cells are required.

In the work presented in this section, we demonstrate that the obstacles found before have been overcome and layered structures with multiple periodicities that behave as panchromatic back reflectors showing wider reflection peaks can be integrating in DSCs. As it will be shown next, this nanostructure material allows to obtain efficiency enhancements similar to those attained coupling standard scattering layers, yet preserving transparency. Strict control over the porosity and the pore size distribution in the nanoparticle based 1DPC, as it was described in the previous chapter, was the key factor leading to this improvement. These results were reported in the publication entitle: "*Panchromatic Porous Specular Back Reflectors for Efficient Transparent Dye Solar Cells*", which has been included in the final list of papers.

2. Device fabrication

In this section, the production step following to prepare the cells studied in this thesis is described. The cell preparation includes the deposition of a nanoporous TiO_2 layer on a conducting glass substrate by screen-printing, the sensitization of the nanoparticles with a ruthenium dye followed by the use of a liquid electrolyte based on an iodide/iodine mixture to put into electrical contact both electrodes. The coupling both nanoparticle photonic crystal and scattering layer to the working electrode is also explained.

2.1. Preparation of TiO_2 Electrodes

In DSCs, photoelectrodes play an important role as electron conductive media besides being a high surface area support for dye molecules to be anchored.[16]

Transparent TiO_2 electrodes made of 20 nm sized particle paste (18-NRT, Dyesol®) were coated via screen printing on top of a glass substrate coated with fluorine-doped tin oxide (FTO, TEC 11 □ /cm^2 , Nippon Sheet Glass), in order to efficiently control the thickness and roughness of these films.

Screen printing is a reliable, versatile and cost-effective method currently used as a deposition technique for thick films of particulate materials. The process is illustrated in figure 3.1 and involves a screen (which is the image carrier) and a

rubber squeegee. The screen uses a porous mesh that has been glued to a metal frame under tension, this characteristic is essential to accurate printing. The pattern is formed by blocking off areas of the screen with a resin where no image should appear.

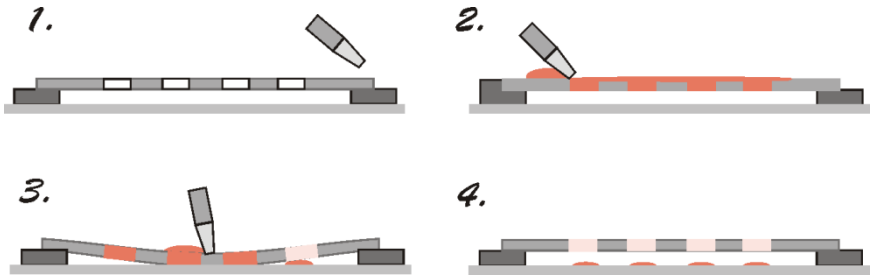

Figure 3.1. Schematic diagram of the screen printing process.

The TiO_2 paste is spread on top of the screen with the squeegee applicator, then the paste is forced into to screen bringing it into contact with the substrate and thereby the paste will pass through the screen reproducing the pattern. Many factors such as paste composition, screen mesh, angle pressure and speed of the squeegee determine the printing quality of the electrode. After the printing process twelve electrodes of TiO_2 were coated on the FTO substrate with dimensions 5 x 5 mm. Once printed, the freshly deposited material must be dried at ambient atmosphere for several minutes, so that the paste can relax to reduce the surface irregularity. (This screen printing procedure will be also employed to deposit the scattering layer onto the electrode.)

After this, films were thermally treated using successive annealing steps. First, they were heated for 15 min at 180 ºC. Temperature was then increased at a rate of 15 ºC/min up to 450 ºC and held for 15 min. A final annealing treatment at 500 ºC was carried out for 15 min. The sintering is needed to burn out organic binders and surfactants as well as to establish a good electrical contact between adjacent TiO_2 particles. Since a strict control of the TiO_2 film is essential to attribute any beneficial outcome on the device performance to possible photonic effects, which allowed us to build reference cells with exact same characteristics that those coupled to optical structures, the layer thickness and the roughness of the electrodes were measured with a profilometer (Mahr®-perthometer PGK). Figure 3.2 shows the profile of a sintered screen-printed TiO_2 layer.

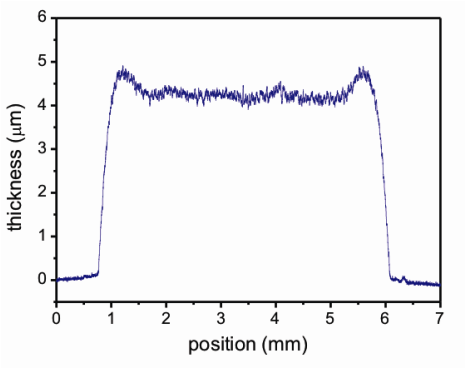

Figure 3.2. Thickness profile of a screen-printed TiO_2 electrode. The average layer thickness was 4.5 □m.

2.2. $TiCl_4$ treatments

Two consecutive titanium tetrachloride ($TiCl_4$) treatments were performed when preparing the TiO_2 photoanodes for dye solar cells, one prior to and one following the deposition method of the nanocrystalline TiO_2 electrodes, to improve the DSC performance.[17] The purpose of the pre-treatment is to form a compact TiO_2 layer by hydrolysis of $TiCl_4$ aqueous solution on top of the transparent-conducting oxide (TCO) in order to blocking the charge recombination at the interface between the conduction glass TCO and the electrolyte, as well as to decrease the bonding strength between the substrate and the porous TiO_2 electrode.[18] Additionally, the result of the second $TiCl_4$ treatment is grown onto the TiO_2 nanoparticles constituting the electrode an extra layer of TiO_2, resulting in an enhancement of the surface roughness factor and necking the TiO_2 particles, thus a higher dye adsorption can be reached. Furthermore, it was also reported that the post-treatment leads to a shift of the conduction band edge in the TiO_2 resulting in an optimized electron injection and a higher photocurrent.[19]

Firstly, an aqueous stock solution of 2 M $TiCl_4$ was prepared by adding slowly titanium tetrachloride (Aldrich) to pre-cooled distilled water in an ice bath in a constant temperature (0 °C). This solution was diluted in aqueous solution with a final concentration of 0.04 M. The pre-treatment was carried out over the FTO glass and the post-treatment after the TiO_2 electrode sintering step. Both were processed by immersing the samples into the $TiCl_4$ and storing in an oven 70 °C for 15 min in a closed vessel. Then, the films were rinsed with

distilled water and ethanol and dried at room temperature in a vertical position. Following the post-treatment, the electrodes were annealed at 450 °C for 30 min.

2.3. Preparation of 1DPC coupled to TiO_2 Electrodes

1DPC structures were built by spin coating deposition of SiO_2 and TiO_2 nanoparticle suspensions on top of the working electrodes following the protocol described in the previous chapter. The spin coating parameter chosen to stack these layers was final speed, ω, 5000 rpm, and acceleration ramp, □, 9180 $rpms^{-1}$, the total process was completed in 60 s. In order to prepare the precursor suspensions to employ during the deposition process, both types of nanoparticles were suspended in a mixture of water (21 vol %) and methanol (79 vol %). The lattice parameter of the periodic stack, that is the thickness of the unit cell, is modified by means of the concentration of the TiO_2 precursor suspensions.[20] TiO_2 dispersions also contained a certain amount of polymer (PEG 20000, Fluka) following the weight relationship of PEG : TiO_2 = 0.5.

Panchromatic 1DPC is built staking three mirrors, each one having different lattice parameter, one on top of each other, in this way, this structure is able to reflect light in a wide wavelength range. The unit cell thickness of the 1DPCs forming the hierarchical architecture was firstly calculated and carefully designed using a MatLab[21] code to find the optimized combination.

2.4. Preparation of a scattering layer coupled to TiO_2 Electrodes

A paste containing TiO_2 large particles (WER2-O, Dyesol®) was used to build 4.5 μm scattering layers. This layer was superimposed via screen printing on top of the transparent electrodes. The two double layers were heated to 450^0C and sintered for 30 min with heating rate of 15^0C/min.

2.5. Preparation and assembly of DSC

The platinum catalyst was obtained after spreading a drop of H_2PtCl_6 (Platisol T, Solaronix®) onto the FTO followed by a heat treatment at 400 ºC for 15 min. A layer of highly catalytic platinum clusters was formed by reduction.

To sensitize the electrodes, they were immersed overnight into a 0.2 mM dye solution (N719, Solaronix®) using ethanol as solvent and kept at room temperature after being heated at 120 ºC for 3 hours in order to assure a proper adsorption of the dye on the TiO_2 surface. After the immersion they were rinsed with ethanol and dried.

The electrolyte used in the cells consists of iodine (I^-) and triiodide (I^{3-}) as a redox couple in 3-methoxy propionitrile (Fluka, ≥99%) as a solvent, furthermore to enhance not only the performance but also the stability of the DSC can be introduced various additives, i.e. specific cations or compounds, to this redox pair. These additives in the electrolytes are expected to be adsorbed onto the TiO_2 surface, thus affecting the conduction band in the TiO_2 strongly associated with the photocurrent and photovoltage. The final electrolyte composition was 100mM I_2 (Aldrich, 99.999%) and 100mM LiI (Aldrich, 99.9%), 600mM $[(C_4H_9)_4N]I$ (Aldrich, 50 98%), and 500mM 4-tert-butylpyridine (Aldrich, 99%).

Both electrodes were assembled and bound by heating to 130° using a thermo-polymer (Surlyn 30, Dyesol®). Finally, they were put into electrical contact by filling the internal space with the liquid electrolyte, which was injected through two small holes made previously at the back of the platinized counterelectrode. Then, the holes were also sealed with the same thermoplastic polymer and a glass cover slide.

3. Photovoltaic Characterization

In this section, the basic characterization of the solar cells used along this thesis, i.e. current-voltage (IV) curve and incident photon to collected electron efficiency (IPCE), is described. Furthermore, these measurements were performed using a black mask covering the device[22,23] otherwise spurious light reflections and refractions, might lead to erroneous interpretations and prevent the comparison of the light harvesting effect.

3.1. IV Curves

The power conversion efficiency of a solar cell is determined from the current versus applied voltage (IV) characteristics under illumination. IV curves were determined by using a solar simulator (Sun 2000, Abet Technologies) applying an external bias to the cell and measuring the generated photocurrent with a

digital source meter (Keithley 2400). Illumination conditions corresponding to the standard AM1.5G spectrum were simulated by the combined use of a 150 W arc xenon lamp and the appropriate filter. The incident light power was periodically confirmed to be 100 $mWcm^{-2}$ using calibrated silicon solar cells.

3.2. IPCE Efficiency

IPCE efficiency measurements were performed used a home-built setup to test the devices analyzed during the present thesis. This system is composed by a broadband light from a 300W xenon lamp, a monochromator with 1140 lines per mm grating (Model 272, Mcpherson) controlled by a digital scan drive system (Model 789A-3) and a picommeter (Keithley 6485). A UV filter with a cut-off wavelength of 400 nm was used to remove the second order harmonics exiting the monochromator. The photonflux of monochromatic light incident on the devices is measured using a calibrated silicon photodiode (D8-Si-100 TO-8 Detector, Sphere Optics).

4. Panchromatic Photonic Crystal based Dye Solar Cells

The use of nanoparticle based photonic crystal coupled to the back side of the TiO_2 electrode of DSCs has been proven to largely improve both light harvesting efficiency (LHE) and power conversion efficiency of these solar devices.[15,14,24] Enhancement in this case results from the intense reflection of unabsorbed radiation back into the photoactive electrode in a specific wavelength range determined by the spectral width of its photonic bandgap. So, the main drawback of these 1D structures when they are compared with a standard scattering layer as back reflector is the narrow spectral region at which photocurrent generation is improved. In this section a multiple period multilayer reflecting in the whole visible range and denoted as panchromatic photonic crystal is presented as a real alternative to these scattering layers, achieving efficiency improvements similar to this latter approach, while guarantees the cell transparency in the visible region of the spectrum.

4.1. Structural and Optical Properties

In order to elucidate the effect the integration of a panchromatic one dimensional photonic crystal has on the cell characteristics, two sorts of light harvesting amplifiers such as two highly reflecting photonic structures and a diffuse scattering layer are built onto the TiO_2 electrodes. Among the former, one of them is a nanoparticle based one dimensional photonic crystal (1DPC) fabricated by stacking a total of eight porosity enhanced SiO_2-TiO_2 nanoparticle bilayers, in which the unit cell thickness (220 nm) is kept constant throughout the multilayer. The other is a hierarchical structure organizer into three different four unit cell 1DPCs deposited one on top of each other. In this case, the thickness of the SiO_2 layer is held for the entire multilayer at 75 nm, while the TiO_2 layer thickness decreases along the direction of incident light from 125 nm in the first Bragg stack to 95 nm and 60 nm in the second and third ones. It should be remarked that the same dielectric mirrors inversely arranged, so that the lattice constant increases in the direction of incoming light, would result in a lower reflectance structure even with narrow transmission windows located at highly absorbing spectral ranges of the dye. To show the structure of this type of stack, image obtained by FESEM (field-emission scanning electron microscope Hitachi S-4800 operating at 2 kV) by backscattered electron detection are presented in figure 3.3.A. The smooth interface between the two types of porous films that form the broad band dielectric mirror as well as the different thickness of the SiO_2 (dark) and TiO_2 (bright) layers can be clearly observed in this picture. This multilayered configuration allows attaining highly reflecting structures covering almost the whole visible range and hence displaying a strong white reflection, as it can be seeing in figure 3.3.B.

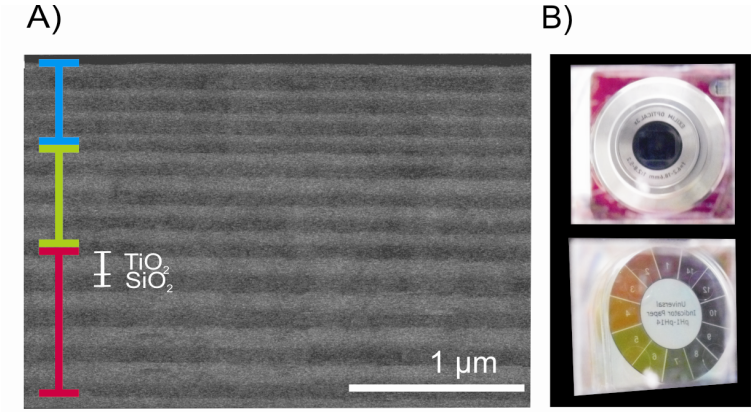

Figure 3.3. A) Magnified view attained by backscattered electron detection of the panchromatic reflector, which allows to distinguish the three different periodicities (colourled lines). B) Pictures of this white light reflecting photonic multilayer.

Moreover, since this multilayered system is designed to present a wide Bragg peak that matches the absorption band of the ruthenium dye but has little effect on longer wavelengths, the cell transparency is preserved. This feature could be of major interest for building integrated photovoltaics (BIPV) in which decorative aspects are also taken into consideration. This characteristic can be readily seen in the picture displayed in figure 3.4.A. For the sake of comparison, a picture of a cell made of a similar nanocrystalline electrode but coupled to a diffuse scattering layer is also shown in figure 3.4.B. Please notice that the underlying text can only be seen through the cell coupled to the photonic multilayer. This fact is mainly a consequence of the radically different mechanism by which the light trapping takes place for both scattering approaches.

FESEM images corresponding to cross-sections of a TiO_2 nanocrystalline electrodes of the same thickness onto which a white-light reflecting photonic crystal and a diffuse scattering layer made of large polyhedral particles of TiO_2 are deposited are displayed in figure 3.4.C and figure 3.4.D, respectively. Please notice that the total thickness of the heterogeneous photonic crystal structure herein proposed is around 2 µm, which is significantly thinner than that of the typical diffuse scattering layer (around 4 µm).

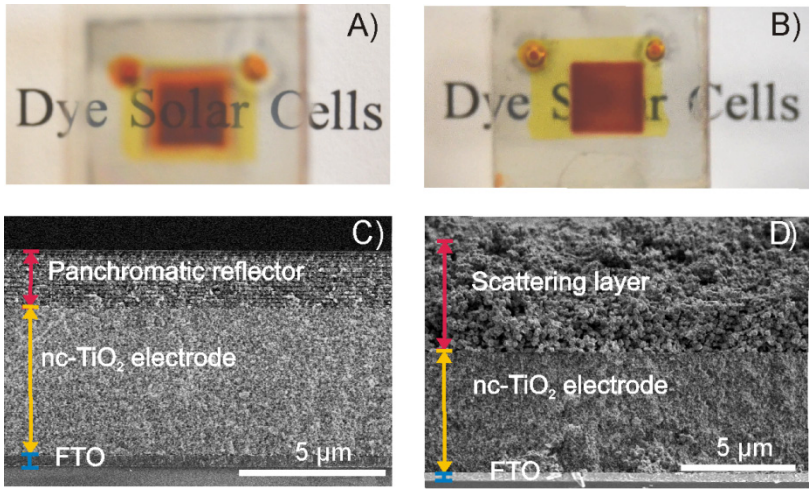

Figure 3.4. *Optical pictures of A) a cell in which a TiO_2–SiO_2 nanoparticle white light reflecting photonic multilayer has been integrated and B) a diffuse scattering TiO_2 layer based cell. The underlying text can only be distinguished through the former. FESEM image of the cross-section of C) a nanocrystalline TiO_2 electrode onto which a white reflecting multilayer has been deposited and, D) a diffuse scattering layer coupled to a TiO_2.*

Optical characterization of such samples was also performed putting special emphasis on the cell transparency. Total reflectance spectra measured for both the PC structures and the diffuse scattering layer after being coupled to the TiO_2 electrodes are plotted in figure 3.5. In all cases, samples are infiltrated with ethanol (n=1.37) to approximate the actual DSC operation conditions, in which the liquid electrolyte (n=1.433)[21] is filling the pores of the whole ensemble. The latter effect gives rise to lower reflected intensities as the dielectric contrast is decreased and, in the case of the 1DPCs, to a red-shift of the Bragg reflectance peak position. Such peak displacement was taken into account when designing both the single and triple period photonic lattices to be integrated in the cells. Since photons are reflected by the diffuse scattering layer with a broad angular distribution, spectra were collected in all cases using an integrating sphere, in this way the specularly reflected beams, as well as the forward diffuse light was measured. For the case of the 1DPC structures, the measured total reflectance shows minimum deviations with respect to the specular one, which evidences their low density of imperfections. The single periodicity structure (dashed line) presents a well-defined Bragg peak in the green region of the spectrum (λmax=530 nm), whereas the second one yields a

broader reflectance bandwidth (solid line) like the one displayed by the standard TiO_2 scattering layer (dashed-dotted line).

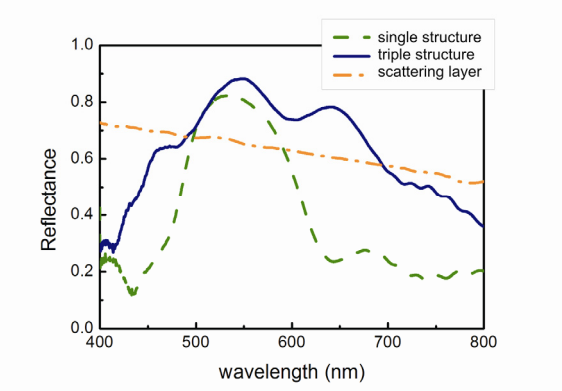

Figure 3.5. Total reflectance spectra of the optical multilayers (dashed and solid lines for the single and triple period structure, respectively) and the diffuse scattering layer coupled to TiO_2 electrodes (dashed-dotted line).

As mentioned before, the multilayered structures are designed to present a highly reflections peak but no effect on larger wavelengths, leaving the semitransparency of the cell. In figure 3.6.A, ballistic transmittance spectra for the 1DPC based solar cells are plotted (dashed and solid lines for single and triple period structures, respectively), together with the spectra obtained from a cell coupled to the diffuse scattering layer (dashed dotted line). Results obtained for a reference cell made with the same TiO_2 electrode thickness (short dashed line), as confirmed by profile measurements, but without any optical back material is also plotted, hence allowing a proper comparison. Please notice that, while the multilayer based cells present an optical transmittance window at the longest visible wavelengths, the diffuse scattering layer turns the cell opaque due to the lack of spectral selectivity of random light scattering. The overall transparency of the whole set of DSC is calculated from the transmittance spectra in the wavelength range of 380 to 780 following the expression based on the methodology prescribed in ISO 9050:2003, applicable to all transparent materials:

$$\tau_v = \frac{\sum_{\lambda=380}^{780} \tau_v(\lambda) D_\lambda V(\lambda) \Delta\lambda}{\sum_{\lambda=380}^{780} D_\lambda V(\lambda) \Delta\lambda}$$

, where V(λ) is the photopic spectral luminous efficiency function that describes the average spectral sensivity of human visual perception (ISO/CIE 10527), D_λ corresponds to the AM1.5 solar spectral irradiance and τ_v (λ) is the spectral transmittance of the sample. Device transparency data (ISO 9050:2003 standard) are plotted in figure 3.6.B and collated in table 1.

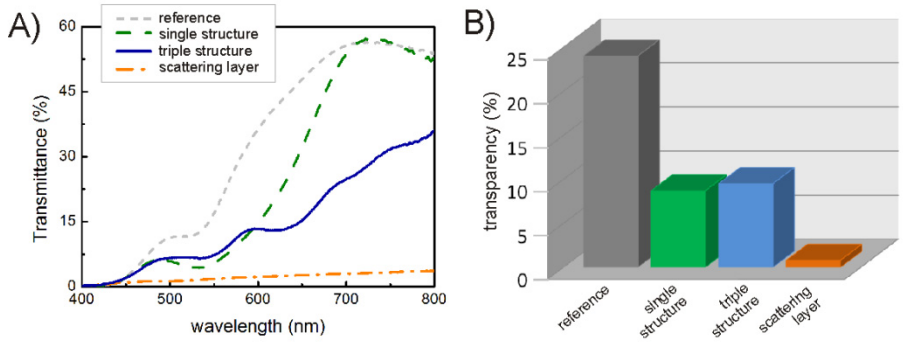

Figure 3.6. A) Transmittance spectra for DSCs coupled to single and triple period photonic structures. For the sake of comparison the transmittance curves of a reference cell and scattering layer based cell is also plotted. B) Histogram showing the transparency values for the same set of cells (same color code).

Whereas semitransparency of DSCs decreases from around 25% down to 1% when diffuse scattering layers are employed, values close to 10% are obtained after coupling single and triple period multilayers. Please notice that, in the case of the samples chosen as example, the transparency of the triple period multilayer is somewhat higher than that of the single period 1DPC, since the overall response of human vision (under bright lighting or photopic conditions) is maximal to light around 550 nm, wavelength range in which the transmittance of the single photonic crystal is lower than that measured for the hierarchical structure. These data are important for future outdoor applications.

5.2. Comparative Performance of DSC coupled to Panchromatic Back Reflector

The effect of selective light trapping of the so fabricated cells were compared after the incorporation of porous 1DPCs reflecting both in a narrow selective wavelength region and in the whole visible spectrum and a scattering layer.

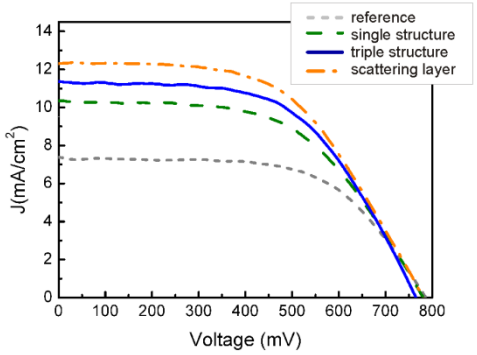

Figure 3.7. IV curves measured from a reference cell (dotted line)and cells integrating a diffuse scattering layer (dashed-dotted line) and two photonic crystal multilayers (dashed and solid lines for the single and triple period structure, respectively).

Photocurrent–voltage (IV) curves were measured for the whole set of samples under standard AM1.5 illumination conditions of 100 mW/cm^2 , which is equivalent to the standard unit of power flux of 1 sun, and are shown in figure 3.7. The main device parameters determinated from theses curves are summarized in table 3.1. Comparatively, the multilayer based DSCs shows better photovoltaic performance than the reference and, among them, the panchromatic dielectric mirrors gives rise to higher short circuit photocurrent density (Jsc), as expected from its broader reflection band. By comparing the power conversion efficiency, η, calculated for these cells, one can see that the efficiency obtained from the white light reflecting PC based cell (4.9 %) is very similar to the value attained for the scattering-based cell (5.2 %). In the former case, this implies an enhancement in the efficiency of 40% with respect to the reference cell, which is the highest enhancement achieved by coupling a non-disordered porous back reflector to a standard thickness electrode. Whereas the improved performance in the case of the photonic structure approach is based on the partial confinement of light within the absorbing layer, the increase in Jsc for the case of the diffuse scattering one is based on the random and non selective scattering of visible frequencies in all directions. This fact that reflections arising from a random packing of large particles are oblique give rise to an extra enlargement of the optical path and thus of the probability of absorption with respect to those achieved with a specular reflector, which explains the stronger reinforcement of efficiency observed for the diffusor.

To scrutinize the origin of the Jsc increase, the incident photon to collected electron (IPCE) efficiency was measured for the whole set of cells, in this way, spectral features of the cell performance were analysed. Both the IPCE curves and the corresponding IPCE enhancement factors, calculated as the ratio between the IPCE of the cells under study and that of the reference cell, are plotted in figure 3.8.A and B respectively. The spectral region at which photocurrent generation is improved coincides, as expected with those at which reflectance is maximum for each type of mirror integrated in the cell. In this case, the periodic structure whose photonic band gap cover the entire visible region gives rise to a higher enhancement and presents similar profile to the diffuse scattering based cell which is consistent with the observation of comparable conversion efficiencies from both devices.

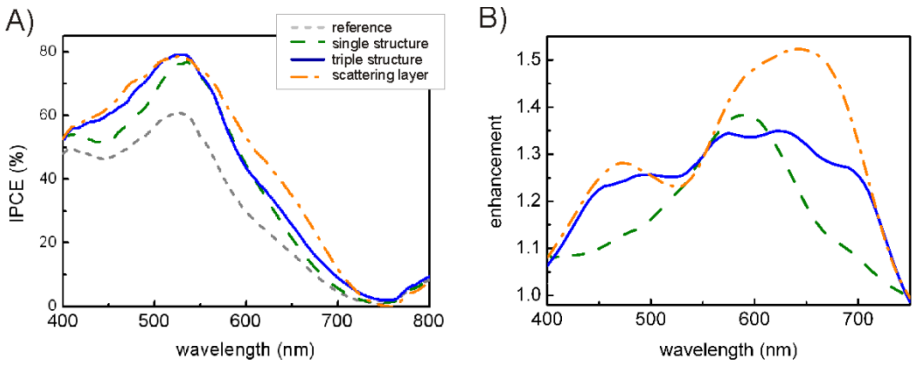

Figure 3.8. A) Incident Photon to Collected Electron (IPCE) efficiencies measured from a reference cell (dotted line) and cells integrating a diffuse scattering layer (dashed-dotted line) and two photonic crystal multilayers (dashed and solid lines for the single and triple period structure, respectively). B) IPCE enhancement factors obtained for the different cells (same colour code).

Optical back scattering material	Transparency (%)	Jsc ($mAcm^{-2}$)	Voc (mV)	ff (%)	η(%)
None (reference DSC)	24	7.5	785	60	3.5
1 unit cell multilayer	8.5	10.5	780	55	4.5
3 unit cell multilayer	9.5	11.5	765	56	4.9
Diffusor	1	12.5	780	54	5.2

Table 3.1. *Values attained for transparency, short circuit photocurrent density (Jsc), open circuit photovoltage (Voc), fill factor (ff), and power conversion efficiency (η) for the different optical back scattering materials tested.*

5. Conclusions

In this chapter we have demonstrated that by integrating a panchromatic photonic crystal into a dye solar cell it is possible to yield efficiency values similar to those attained with diffuse scattering-based cells, as a result of the broader reflectance bandwidth presented by this hierarchical optical multilayer. Though efficiency enhancement have been achieved before by implement photonic structures in DSC, none as high as those reached using a white reflecting PC as light harvesting enhancer in this type of cell has been reported.

This highly reflecting and porous structure covering the whole visible range can be built by stacking three nanoparticle based PCs with different unit cells deposited one on top of each other. This advance has been possible due to the strict control over the overall porosity and pore size distribution of the layers forming the photonic crystal.

Also, since this multilayered system has been also designed to have no effect on larger wavelengths, the semitransparency of the cells is almost unaltered. It constitutes one of the main advantages with respect to the diffuse scattering layer, approach that has been explored the most to increase the photogenerated current in DSCs until now, thus making these devices suitable for building integrated photovoltaics (BIPV) application.

6. References

[1] S. Ito, S.M. Zakeeruddin, R. Humphry-Baker, P. Liska, R. Charvet, P. Comte, M.K. Nazeeruddin, P. Péchy, M. Takata, H. Miura, S. Uchida, M. Grätzel, *Adv.Mater.* 2006, **18**, 1202.

[2] Y. Chiba, A. Islam, Y. Watanabe, R. Komiya, N. Koide, L. Han, *Jpn. J.Appl. Phys.*, 2006, **45**, 25.

[3] C. Chen, M. Wang, J. Li, N. Pootrakulchote, L. Alibabaei, C. Ngoc-le, JD. Decoppet, J.Tsai, C. Gra□tzel, C.Wu, SM. Zakeeruddin, M. Gra□tzel, *ACS Nano*, 2009, **3**, 3103.

[4] Y. Cao, Y. Bai, Q. Yu, Y. Cheng, S. Liu, D. Shi, F. Gao, P. Wang, J *Phys Chem C*, 2009, **113**, 6290.

[5] A. Yella, H. W. Lee, H. N. Tsao, C. Yi, A. K. Chandiran, M. K. Nazeeruddin, E. W. G. Diau, C. Y. Yeh, S. M. Zakeeruddin, and M. Grätzel, *Science*, 2011, **334**, 629.

[6] S. Hore, C. Vetter, R. Kern, H. Smit, A. Hinsch, *Sol. Energy. Mater. Sol. Cells*, 2006, **90**, 1176.

[7] F.E. Gálvez, E. Kemppainen, H. Míguez, J. Halme, *J. Phys. Chem. C*, 2012, **116**, 11426.

[8] S. Yoon, S. Tak, J. Kim, Y. Jun, K. Kang, J. Park, *Build. Environ.*, 2011, **46**, 1899.

[9]S. Colodrero, A. Mihi, L. Häggman, M. Ocaña, G. Boschloo, A. Hagfeldt and H. Míguez, *Adv. Mater.*, 2009, **21**, 764.

[10] C.T. Yip, H. Huang, L. Zhou, K. Xie, Y. Wang, T. Fenq, J. Li. W.Y. Tam, *Adv.Mater.*, 2011, **23**, 5624.

[11] A. Mihi, C. Zhang, P. Braun, *Angew. Chem. Int. Ed.*, 2011, **50**, 5712.

[12] S.Nishimura, N.Abrams, B. A. Lewis, L. I. Halaoui, T. E. Mallouk, K. D. Benkstein, J. van de Lagemaat, A.J. Frank, *J. Am. Chem. Soc.*, 2003, **125**, 6306.

[13] S. Guldin, S. Huttner, M. Kolle, M.E. Welland, P. Müller-Buschbaum, R.H. Friend, N. Steiner, N. Tetreault., *Nano Lett.*, 2010, **10**, 2303.

[14]S. Colodrero, A. Forneli, C. López-López, L. Pellejà, H. Míguez, E. Palomares, *Adv. Funct. Mater.* 2012, **22**, 1303.

[15]A. Mihi, F. J. López-Alcaraz, H. Míguez , *Appl. Phys. Lett.*, 2006, **88**, 193110.

[16] Q.Zhang and G. Cao, *Nano Today*, 2011, **6**, 91.

[17] L. Vesce, R. Riccitelli, G. Soscia, T. M. Brown, A. Di Carlo, A. Reale, *Journal of Non-Crystalline Solids,* 2010, **356**, 1958.

[18] S. Ito, P. Liska, P. Comte, R. Charvet, P. Péchy, U. Bach, L. Schmidt-Mende, S.M. Zakeeruddin, A. Kay, M.K. Nazeeruddin, M. Graetzel, *Chem. Comm.*, 2005, 4351.

[19] B.C. O'Regan, J.R. Durrant, P.M. Sommeling, N.J. Bakker, *J. Phys. Chem. C.*, 2007, **111**, 2007, 14001.

[20] S. Colodrero, M. Ocaña, H. Míguez *Langmuir*, 2008, **24**, 4430.

[21] G. Lozano, S. Colodrero, O. Caulier, M.E. Calvo, H. Míguez, *J. Phys. Chem. C,* 2010, **114**, 3681.

[22] H.J. Snaith, *Energy & Environ. Sci.*, 2012, **5**, 6513.

[23] S. Ito, M. Nazeeruddin, P. Liska, P. Comte, R. Charvet, P. Péchy, M. Jirousek, A. Kay, S. Zakeeruddin, M. Grätzel, *Progr. Photovolt.: Resp. Appl.*, 2006, **14**, 589.

[24] D. Colonna, S. Colodrero, H. Lindström, A. Di Carlo and H. Míguez, *Energy & Environ. Sci.*, 2012, **5**, 8238.

Chapter 4

Angular Response of One Dimensional Photonic Crystal based Dye Solar Cells

1. Introduction

Dye Solar Cells (DSC) are one of the most promising new generation photovoltaic technology as it can generate electricity with low production cost. Moreover, a critical advantage of such DSC over current technologies is its adaptability for Building Integrated Photovoltaic (BIPV) applications, since possess intriguing properties such as transparency and colour tunability and good performance retention at different conditions of illumination.[1-5]

In previous chapter, nanoparticle one dimensional photonic crystals (PC) have been reported as an optical back scattering material to integrate in this sort of photovoltaic devices. This approach not only improve their performance but also preserve the cell transparency and achieve different look of the cell without the needed of changing the sensitizer by mean of introducing PC reflecting in different wavelength ranges.[6] These features could be of major interest for BIPV in which decorative aspects are also taken into consideration.

Since these PC based solar cells are presented as ideal case of a building integrated module, it becomes important to carry out systematic angular studies of power conversion efficiency and incident photon-to-current

conversion efficiency (IPCE), in view of outdoor devices receive photons that rarely hit their surface at normal incidence, due to differing placement upon installation and daily and seasonal variations of the sun's position.[7] This analysis is expected to become particularly complex because PCs present intrinsic optical anisotropy.

In the present chapter it will be analyzed the performance of photonic crystal based dye solar cells as the incident light angle moves away from the normal with respect to the cell surface. The interplay between optical and photovoltaic properties with the incident light angle will be discussed. We demonstrate that an efficiency enhancement is attained for PC-DSCs at all angles measured, and that rational design of the photonic crystal back mirror leads to a reduction of the photocurrent losses related to the tilt angle of the cell, usually labeled as "cosine losses". Angular variations of the cell transparency are also reported and discussed.

2. Photonic crystal based Dye Solar Cells

In photonic crystal, light reflection results from interferometric effects and therefore its intensity and spectral features are dependent on the direction of propagation of light, as it was explained in the introduction chapter. The spectral position of the reflection maximum, λ_B, of a PC made of two types of alternating films of thicknesses t_1 and t_2 and refractive indexes n_1 and n_2, respectively, depends on the incident angle with respect to the surface normal, , as expressed in the equation:

$$\lambda_B = 2d\sqrt{n^2 - (\sin\theta)^2} \qquad 4.1$$

, where d is the unit cell size and n is the average refractive index of the multilayer, which is in turn given by:

$$n = \frac{t_1 n_1 + t_2 n_2}{d} \qquad 4.2$$

Since the relative position between the dye absorption spectrum and the Bragg peak of the reflector is actually the source of the different photovoltaic performance of PC based DSC, as it was reported in previous work,[6,8] it was needed to carry out a complete angular study of such devices. For that end, two sort of PC based DSC are considered. On the one hand, photonic crystals operating in different narrow and well defined spectral ranges, on the other a

panchromatic PC, whose reflection peak cover the whole visible range (400-800 nm). The former are composed by four SiO_2-TiO_2 unit cells, in which the thickness of the TiO_2 layers was slightly varied from one sample to other, by means of the use of different concentrations of the nanoparticle precursor suspensions (3 wt%, 4 wt% and 5 wt%). From now on the criterion used to denominate each one of these PC based cells is its colour reflected, DSC-B for blue-reflecting, DSC-G for green-reflecting and DSC-R for red-reflecting. This set of PC-DSC was prepared as Chapter before describes, but the $TiCl_4$ treatments was not employed, for that reason a reference cell (without photonic crystal) was also fabricated to compare the photovoltaic properties.

The other photonic structure is the result of stack three multilayered structures with different lattice parameter one on top of each other as it was explained in the previous chapter. Furthermore, a nanoparticle TiO_2 scattering layer based DSC (scattering layer-DSC) and a reference cell (without any back optical material) were also prepared for the sake of comparison. These devices were fabricated following the experimental procedure as stated previously in Chapter 3.

Total reflectance spectra of the abovementioned cells attained under rear illumination conditions (in this experimental configuration light comes into contact with the counterelectrode, travels through the electrolyte to reach the scattering material inside the cell) are shown in figure 4.1. Superimposed, the absorption curve of a sensitized TiO_2 film (after anchoring N719 dye on the TiO_2 nanoparticles) with similar thickness than the electrodes employed in the solar devices is drawn (black solid line) to show explicitly the degree of overlap between the spectral regions in which high optical scattering and absorption occur. As it can be seen, both the panchromatic PC-DSC and scattering layer-DSC the total yield a broader reflectance bandwidth in the range matching with the absorption spectrum of the dye. Regarding the single period PC, the highest overlap between the reflectance and absorption spectra takes place in the case of the cell that incorporates the PC that reflects in the green (reflection peak centered at 550 nm), DSC-G (green dot line), whereas the reflectance peak of DSC-B is located at shorter wavelength and that of DSC-R at longer ones in comparison with the maximum of the ruthenium dye absorption. It should be taken into account that the much lower reflectance of these structures at shorter wavelengths (400-450 nm) is due to the presence of the I^-/I^{3-} electrolyte whose absorption peak is located in this range.

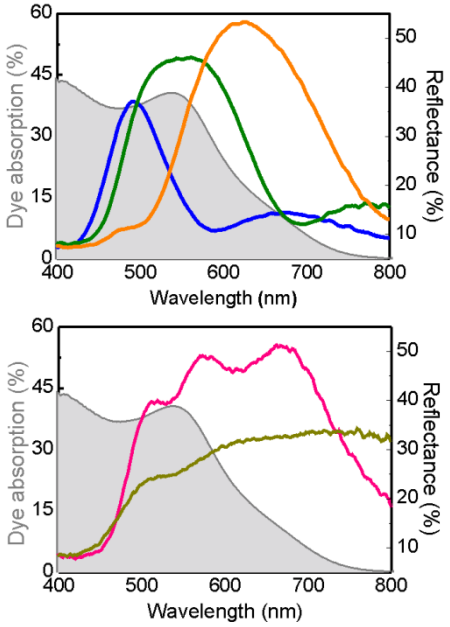

Figure.4.1. A) Reflectances spectra of the DSCs coupled to different 1DPC infiltrated with electrolyte under rear illumination conditions, namely DSC-B (blue dash line), DSC-G (green dot line), DSC-R (orange dash dot line), panchromatic PC-DSC (pink solid line) and scattering layer-DSC (grey short dashed-dotted line). The absorption of the sensitized cell is also plotted (black line).

3. Optical Properties *vs* light incident angle

As it was exposed in the introduction of the present chapter, the main added value of the photonic crystal based DSCs to be used in Building Integrated Photovoltaic (BIPV) projects as high efficiency solar devices is their decorative properties. Therefore, in this section the look presented by these DSCs as the light incident angle tilted from the normal to the cell surface will be evaluated.

Ballistic transmittance spectra corresponding to the same DSCs presented in the previous section are plotted in figure 4.2.A. From this data, the overall transparency (τ_v) of the whole set of DSC is estimated following the expression based on the methodology prescribed in ISO 9050:2003 and presented in the section 4.1 of the previous chapter. Whereas at normal light incident the perceived transparency for a reference cell is around 23%, when a PC is implemented in the device the τ_v take values comprised between 9 and 17%. It

should be reminded that τ_v is dependent on the overall response of human vision, which is maximal to light around 550 nm, so the transparency of PC-DSC is the result of the different overlap between the human eye optical sensitivity curve, the dye aborption spectrum and the Bragg peak of the optical structures. On the other hand, the weighted transparency decreases down to 1% for a DSC in which bigger TiO_2 particles are stacked on top of the dyed layer as a standard diffuse layer. In what follows, we shall only consider the transparent DSCs of the whole set of samples to carry out the optical characterization.

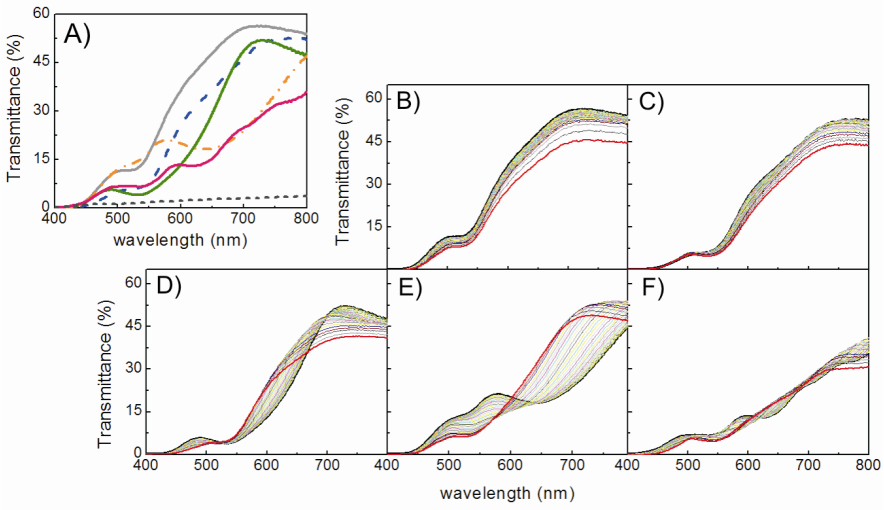

Figure 4.2. *A) Transmittance spectra of a reference DSC (grey curve) and for three DSCs coupled to different 1DPC, namely DSC-B (blue dash line), DSC-G (green dot line), DSC-R (orange dash dot line) and panchromatic PC-DSC (pink line). For comparison, the transmittance spectra of a DSSC with a diffuse scattering layer coupled to the electrode (black short dash). (B-F) Transmittance spectra measured for reference DSC (B), and different PC-DSC, namely DSC-B (C), DSC-G (D), DSC-R (E) and panchromatic PC-DSC (F) from 0 degree (thick grey line) to 60 degrees (thick red line).*

To evaluate the effect of the different incident light angle over the appearance of the transparent cells under study, transmittance spectra from 0 degree to 60 degrees were taken (Figure 4.2.B-F). The evolution of the spectral dependence of the transmittance of the cell used as reference clearly indicates that it gradually loses transparency as the angle varies from 0 degree to 60 degrees (Figure 4.2.B), which is a direct consequence of the increase of both the reflectance at the air/glass interface according to Fresnel laws and the optical

path through the active layer. On the other hand, the changes observed in the transmittance curves of the PC-DSC (Figure 4.2.C-F) are more complex, being mainly determined by the shift to shorter wavelengths of the Bragg peak given by equation 4.1. For the transmittance spectra corresponding to DSC-B (Figure 4.2.C), the effect of the spectral downshift of the Bragg peak is screened by the absorption of other components of the cell, such as the TiO_2 and the electrolyte. However, gradual modifications are clearly observed for the others PC-DSCs.

This spectral change observed at different angles is also noticeable by the naked eye, as it can be clearly seen in figure 4.3. These images show how, as the illumination angle varies, the reflected structural colour turns from green (Figure 4.3.A) to blue (Figure 4.3.B) for DSC-G, and from orange (Figure 4.3.C) to yellow (Figure 4.3.D) in the case of DSC-R.

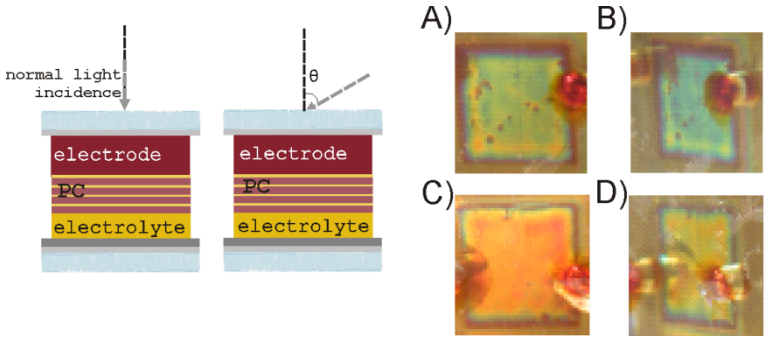

Figure 4.3. Images showing the colour change when DSC-G (A-B) and DSC-R (C-D) were exposed at two different incident light angles.

The exposition of the PC-cells to different illumination angle not only changes the cell colour but also the transparency of such devices. This latter effect is evaluated by using the expression based on the methodology prescribed in ISO 9050:2003 shown in Chapter 3. In Figure 4.4.A the transparency of the cells as a function of the incident light angle is plotted. Regarding the trends observed as the angle increases, the reference cell transparency decreases monotonically as expected from the larger absorption caused by an increment of the light path inside the active layer and by the decrease of the light coupling resulting from the higher reflection at the air-glass interface. On the other hand, focusing on the results obtained from the PC-DSCs, it should be remarked that the low transparency corresponding to the DSC-G and the panchromatic PC-DSC is related to the high grade of overlapping between the reflection peak of these

photonic structures and the absorption band of the ruthenium dye and t. However, the behaviour of these two types of cells as the incident light angle increase is different due to the different bandwidth of their respective Bragg peaks (Figure 4.1.A). For the case in which a single period photonic crystal reflecting in the green region is coupled to the DSC (DSC-G), the device undergoes a rise of transparency because the Bragg peak position is shifted with respect to the absorption band of the dye as a result of tilting. This also explains the opposite trend found for DSC-R. In the other case, in which the reflection peak covers the whole visible spectrum at normal incidence, a slight fall of transparency is observed since the panchromatic photonic crystal is designed to its Bragg peak matches the maximum absorption of the ruthenium dye (close to 530 nm) at any angle. To show this different behaviour more clearly, transparency is normalized to its value at normal incidence (□=0 degree), Figure 4.4.B.

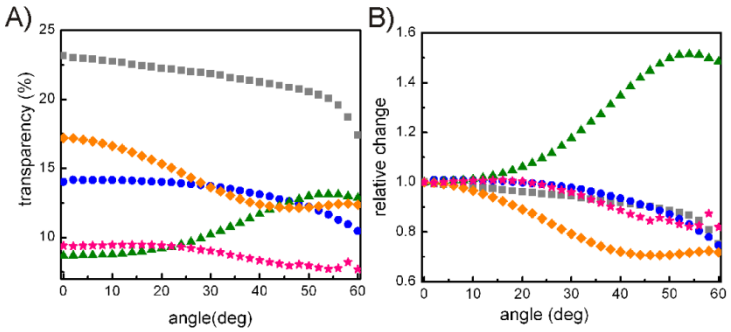

Figure 4.4. A) Transparency data obtained from transmittance curves versus incident light angle and B) normalized transparency to its value at normal incident for reference DSC (grey squares), DSC-B (blue circles), DSC-G (green triangles), DSC-R (orange rhombi) and Panchromatic PC-DSC (pink stars).

4. Photovoltaic Properties *vs* light incident angle

The above mentioned effect of spectral shift of the Bragg peak towards shorter wavelength, caused by the tilt of the illumination angle, is expected to have a significant influence on the photovoltaic properties of these solar devices. To deeper investigate the angular effect over these features, the current intensity-voltage (IV) characteristic curves were acquired at different illumination angle

using the experimental procedure described in chapter 3. Since this analysis were carried out for two sets of DSCs, each of them will be presented in separate graphs with their respective reference cell to establish a proper comparison of the effect the angle radiation have on the photovoltaic properties of such devices.

Several examples of IV curves extracted at different light incident angle are displayed in Figure 4.5, from where it can e concluded that, a clear photocurrent density (J_{SC}) increase for all the angles measured (0 to 60 degrees) is attained for those devices in which the 1DPC have been integrated. Resulting the largest photocurrent enhancement at normal light incidence the PC-DSC whose photonic band gap has a larger overlap with the absorption band of the ruthenium dye, whereas at larger incoming light angles the photocurrent generated by these DSCs is similar. This behavior is again the result of the downshift of the spectral position of the reflectance peak of the PCs as the incident light angle moves away from the normal incidence expressed in equation 4.1.

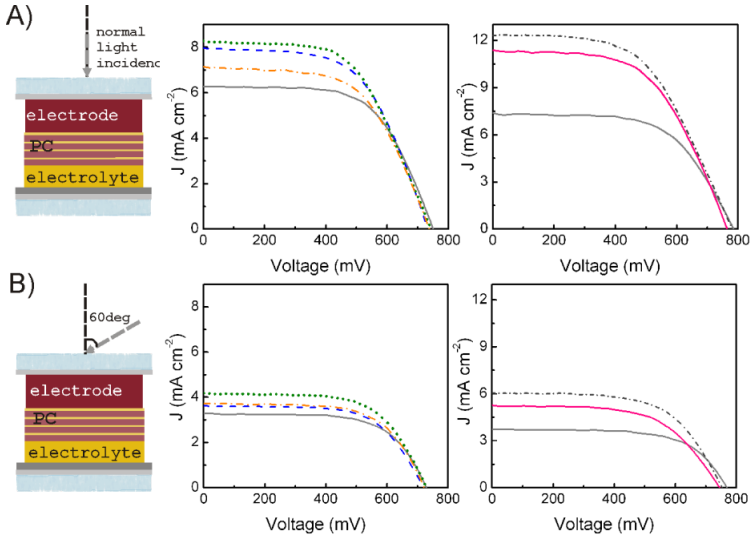

Figure 4.5. IV curves for DSC coupled to different highly porous 1DPC, namely DSC-B (blue dash line), DSC-G (green dot line), DSC-R (orange dash dot line) and a panchromatic PC-DSC (pink solid line). Results for reference cells (grey solid line) and scattering layer-DSC (grey dash dot line) are also plotted for the sake of comparison at different illumination angles ((A) 0, (B) 60 degrees).

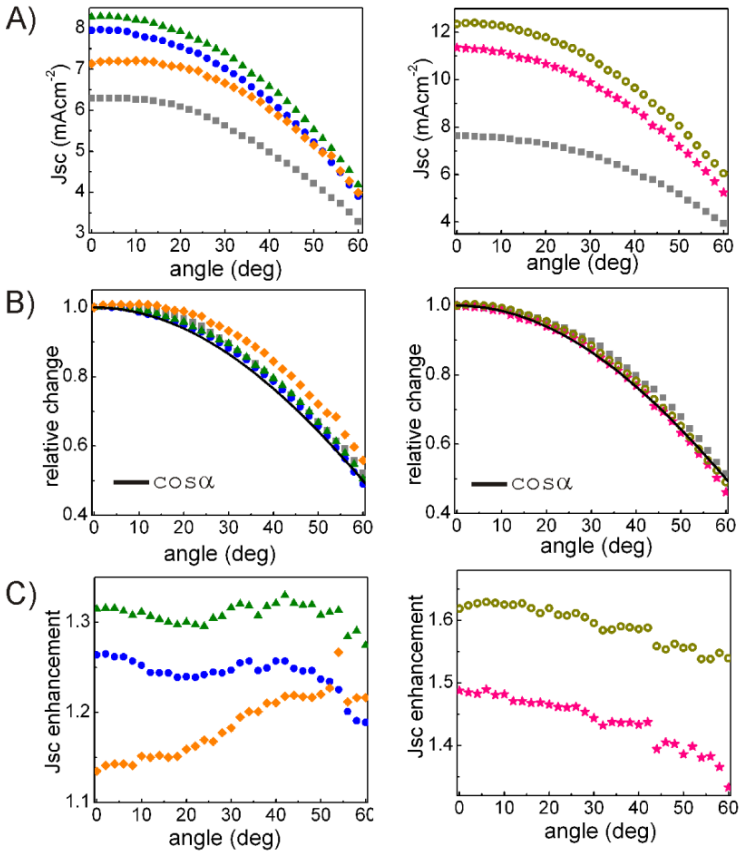

Figure 4.6. A) J_{SC}, B) normalized J_{SC} and cosine curve (solid line), as a function of the angle for reference DSC (grey squares), DSC-B (blue circles), DSC-G (green triangles), DSC-R (orange rhombi) and Panchromatic PC-DSC (pink stars) and a scattering layer-DSC (yellow open circles). C) J_{SC} enhancement for the different PC-DSC with the same color code.

More detailed analysis of the variation of J_{SC} with incident light angle for the cells under study can be seen in figure 4.6; these data were extracted for the corresponding IV curve. As the cell is tilted with respect to the incident beam the effective cross section or apparent surface of the device decreases. The intensity of light, I, from a collimated beam impinging on an inclined plane follows Lambert's cosine law:

$$I(\theta) = I(0)\cos(\theta) \qquad 4.3$$

This is the origin of the well-known performance "cosine losses" that occur for solar cells operating at a tilted angle. However, the drop of J_{SC} observed experimentally will not be exactly fitted by equation (4) (black solid line in

Figure 4.6.B), as light path within the electrode is also larger when it is tilted, which contributes to enlarge the absorption. At the same time, for large angles, some transmittance losses as a result of larger reflections at the glass substrate surface must also be taken into account. These effects are present in all devices herein presented.

For the case of the PC-DSC, the main reason for this clear disagreement with values obtained for the reference cell is the different absorption enhancement attained as a consequence of the overlap between Bragg peak and the dye absorption band. This explains the interest effect observed for those PC-DSC in which the overlap increases with the angle, as it is the case of DSC-R (orange rhombi in Figure 4.6.B). The origin of this compensating effect of the red light reflecting PC can be clearly seen in Figure 4.6.C, in which the Jsc enhancement for the different PC-DSC at different illumination angle is plotted. On the contrary, the photocurrent enhancement obtained for DSC-G is higher at any given angle and shows a steady angular response, while that of DSC-B decreases at larger angles as the Bragg reflection peak enters the absorption region of the TiO_2 nanocrystals. On the other hand, focusing on the panchromatic PC-DSC, it clearly observed that the integration of this three unit cell multilayer provides an improvement of light harvesting almost as independent of the illumination for light beams impinging between the normal to the cell and approximately 45 degrees, above that incidence angle, the blue-shift of the 1DPC reflectance gives rise to lower enhancements at red light frequencies comparing with the scattering layer-DSC. Another interesting feature is the similarity between the angular behaviour of this scattering layer based and the theoretical predictions (Figure 4.6.B), this fact is the result of the randomness in the direction of light scattered back into the absorbing layer, which compensate the effect of enlarge the optical path through the electrode when the cell is tilted to the light incident.

On the other hand, if one look at the open circuit voltage (V_{OC}) data measured, one will note that a minor photovoltage drop of approximately 1.5% is attained when the photonic structure is coupled to the cell. The dependence of Voc *versus* the illumination angle is also studied and summed in Figure 4.7.A. Theory predicts that Voc gradually decreases with increasing angles. The Voc can be analyzed following the equation 4.4 based in a diode model,[9] in which the nanostructure TiO_2 is treated like the n-material and the p-material is the redox electrolyte.

$$V_{OC} = m\frac{KT}{e}\ln\left(\frac{\mathrm{Isc}}{I0}\right) \qquad 4.4.$$

Where m is an ideality factor, whose value varies between 1 and 2, T the cell temperature, k the Boltzman's constant and e the electron charge. The angular behaviour of Voc can be understood in a first approximation, neglecting second order effects, by considering the effect of Lambert's cosine law on the photovoltage:[10]

$$V_{OC}(\theta) = V_{OC}(0) + m\frac{KT}{e}\ln\left(\frac{\mathrm{I}(\theta)}{I(0)}\right) = V_{OC}(0) + m\frac{KT}{e}\ln(\cos\theta) \qquad 4.5$$

Where $V_{oc}(0)$ is the open-circuit voltage at normal irradiance. A normalized curve of V_{oc} versus θ is plotted in Figure 4.7.B by considering T=300K and m=1. It can be seen that stronger deviations from this simple equation are observed for PC-DSC, for which the electromagnetic power within the electrode depends strongly on the relative position of the Bragg peak with respect to the ruthenium dye absorption band.

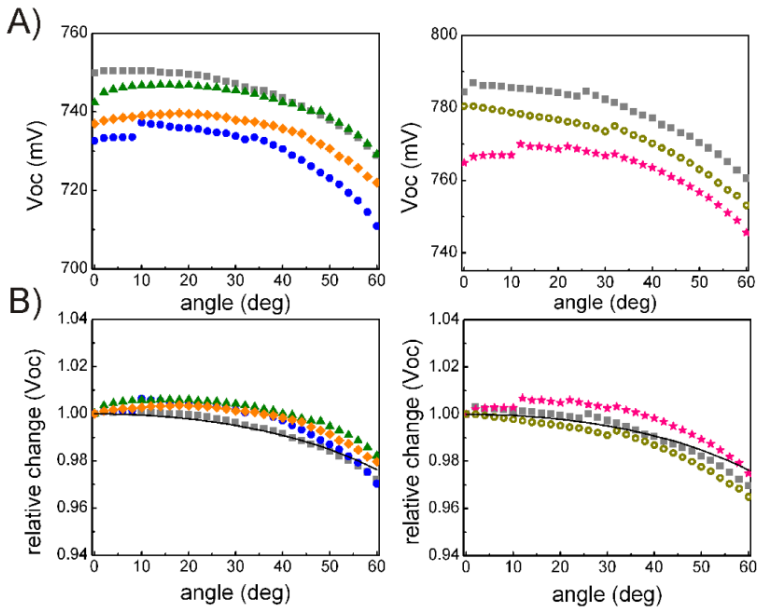

Figure 4.7. A) Angular dependence of V_{OC}, and B) normalized V_{OC} for reference DSC (grey squares), DSC-B (blue circles), DSC-G (green triangles), DSC-R (orange rhombi) and Panchromatic PC-DSC (pink stars) and a scattering layer-DSC (yellow open circles). Solid line in B) is attained from equation 4.5 considering T=300K and m=1.5.

Regarding the fill factor (Figure 4.8.A, the integration of a back scattering material in the cell gives rise to a small resistance to electrolyte flow, and therefore to slightly lower fill factors. In this case, as the tilt angle is higher, the irradiance that reaches the surface of the cell is smaller, which lowers the internal resistances that depend on the amount of current,[11] reducing the charge recombination and increases ff, whose angular change relative to its value at □ =0 is displayed in Figure 4.8.B. A secondary effect to take in account caused by the reduce of the amount of current is the decrease of the mobility of the electrons in the semiconductor network due to the increase of the probability of the electron to be in traps (energy states below the conduction band), leading to reduce the ff. However, this lowering in conductivity is less than the drop in the internal resistances.

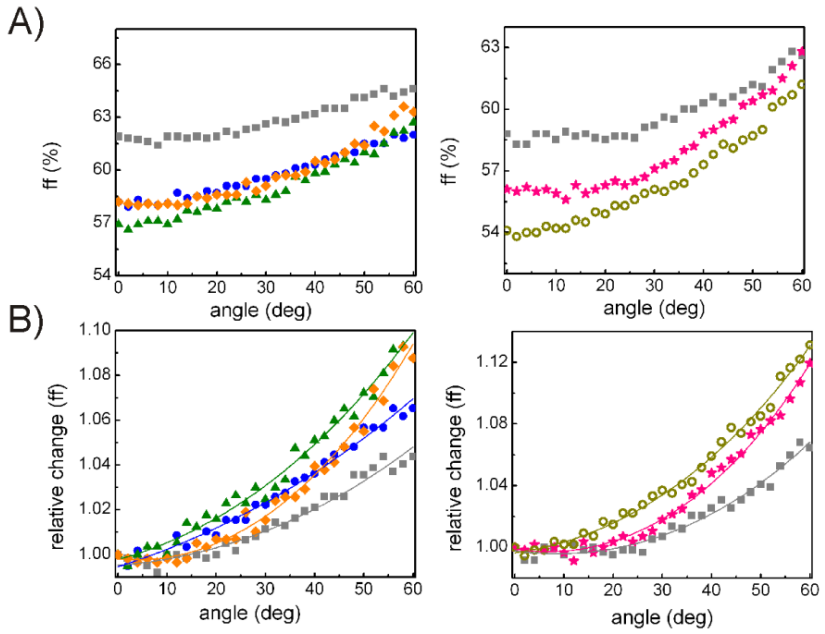

Figure 4.8. A) Angular dependence of ff and B) normalized ff for reference DSC (grey squares), DSC-B (blue circles), DSC-G (green triangles), DSC-R (orange rhombi) and Panchromatic PC-DSC (pink stars) and a scattering layer-DSC (yellow open circles). Solid lines in B) are just a guide to the eye.

The variation of the power conversion efficiency, η, with incident angle is also plotted in Figure 4.9. The angular evolution of the relative change (Figure 4.9.B) mimics that observed by the J_{SC}, with minor deviations caused by the opposite angular trends of V_{OC} and ff.

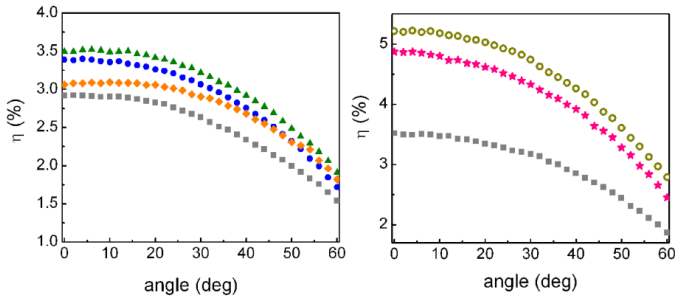

Figure 4.9. A) Angular dependence of power conversion efficiency (□) for reference DSC (grey squares), DSC-B (blue circles), DSC-G (green triangles), DSC-R (orange rhombi) and Panchromatic PC-DSC (pink stars) and a scattering layer-DSC (yellow open circles).

Finally, the selective spectral enhancement of light harvesting is analyzed by acquisition of incident photon to collected electron (IPCE) efficiency measurements (Figure 4.10). It allows a better understanding on how the mechanism of DSC operation could be affect by the illumination angle. In principle, when a 1DPC is introduced in the cell, the IPCE efficiency increases for all angles measured, in good agreement with the IV curve analysis. It can also appreciated from these graphs that, as expected, each PC-DSC performs better at the spectral range at which the photonic crystal is back reflecting.

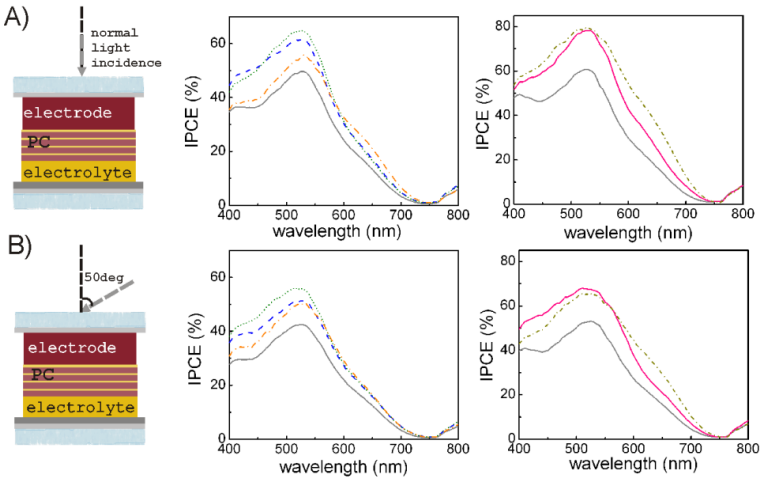

Figure 4.10. IPCE curves for DSC coupled to different highly porous 1DPC, namely DSC-B (blue dash line), DSC-G (green dot line), DSC-R (orange dash dot line) and a panchromatic PC-DSC (pink solid line). Results for reference cells (grey solid line) and scattering layer-DSC (yellow dash dot line) are also plotted for the sake of comparison at different illumination angles ((A) 0, (B) 50 degrees).

In each case, an IPCE enhancement factor was calculated as the ratio between the IPCE of the cell coupled to the scattering material and that of the standard one (Figure 4.11). In this way, it is clearly seen that the enhancement factor calculated for the DSC coupled to the photonic crystals shifts towards shorter wavelengths as the cell is tilted, while IPCE enhancement corresponded to that obtained for the scattering-DSC remains spectrally unaltered as the incident irradiance angle change. Again, it should be remarked that the presence of the photonic crystal not only enhances the photo-generated current but also varying the spectral photoelectric response of such devices in a control manner.

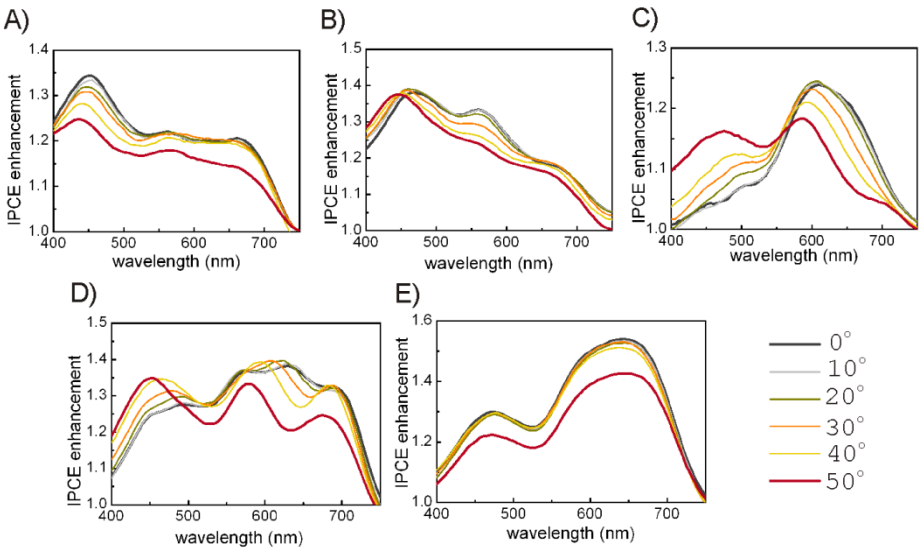

Figure 4.11. IPCE enhancement factor curves for DSC-B (A), DSC-G (B), DSC-R (C), panchromatic PC-DSC (D) and scattering layer-DSC (E). The figure caption appears on the right of the graphs.

5. Conclusions

In this chapter, we have analysed the interplay between optical and photovoltaic response as the incident light angle varies for dye solar cells in which different light harvesting amplifiers are integrated. In this way, we have demonstrated that the optical absorption enhancement effect that gives rise to higher photocurrent, and thus to higher power conversion efficiency, is maintained for all angles measured.

We show that the characteristic cosine losses of these angular measurements can be partially compensated by the interplay of this effect with the angular variations of the Bragg peak position when a photonic crystal is implemented in DSC. The effect the incident radiation angle has on the cell appearance both in colour and transparency has also been studied a strong dependence with the angle of illumination having been described.

Of further relevance is the characterization of the angular performance of photonic crystal based DSC herein presented opening a promising route to highly efficient while transparent modules to evaluate its potential for building integrated photovoltaics.

6. References

[1] G. E. Tulloch, *J. Photochem. Photobiol A,* 2004, **164**, 209.

[2] J. Kawakita, *Science & Technology Trends*, Quarterly Review Nº 35, 2010.

[3] A. Hinsch, H. Brandt, W. Veurman, S. Hemming, M. Nittel, U. Würfel, P. Putyra, C. Lang-Koetz, M. Stabe, S. Beucker, K. Fichter, *Sol. Energy. Mater. Sol. Cells*, 2009, **93**,820.

[4] S. Yoon, S. Tak, J. Kim, Y. Jun, K. Kang, J. Park, *Build. Environ*., 2011, **46**, 1899.

[5] W.J Lee, E. Ramasamy , D.Y. Lee, J.S. Song , . *J Photochem Photobiol A-Chem*, 2008, **194**, 27.

[6] D. Colonna, S. Colodrero, H. Lindström, A. Di Carlo and H. Míguez, *Energy & Environ. Sci*., 2012, **5**, 8238.

[7] D. D'Ercole, L. Dominici, T.M. Brown, F. Michelotti, A. Reale, A. Di Carlo, *Appl. Phys. Lett*., 2011, **99**, 213301.

[8] G. Lozano, S. Colodrero, O. Caulier, M.E. Calvo, H. Míguez, *J. Phys. Chem. C*, 2010, 114, 3681.

[9] F. Fabregat-Santiago, G. García-Belmonte, I. Mora-Seró, J. Bisquert, *Phys. Chem. Chem. Phys*., 2011, **13**, 9083.

[10] J.L. Balenzategui, F. Chenlo, *Solar Energy Materials & Solar Cells*, 2005, **86**, 53.

[11] B.C. O´Regan, J.R.Durrant, *Acc.Chem.Res.*, 2009, **42**, 1799.

Chapter 5

One Dimensional Diffraction Grating to Improve Light Harvesting in Dye Solar Cells

1. Introduction

Along this thesis the use of one dimensional photonic crystals (1DPC) to improve dye solar cell (DSC) performance has been thoroughly studied and analyzed, reaching conversion efficiencies similar to those obtained coupling diffuse scattering layers to the cells while preserving the cell semitransparency and their application as building integrated photovoltaics (BIPV).

This last chapter addresses the use of diffraction gratings patterned on the backside of TiO_2 electrode to enhance light harvesting in DSCs. This light trapping strategy has been successfully employed in other types of thin film solar cells.[1-6] But, its implementation in dye solar cell is still in infancy and only a reduced number of works have been reported.[7-9] Resulting from the presence of this grating, light is scattered covering longer oblique trajectories in the electrode and, consequently, increasing the probability of photon absorption and the photocurrent generation efficiency.

One of the most relevant goals herein presented herein is the use of a stamping process based on the combination of soft-lithography the micro patterning.

Furthermore, the use of stamps based on vinyl and hidrosilane end-linked polymer, called "hard PDMS" (h-PDMS) allows transfering the pattern with high fidelity. Finally, for the first time, it will be reported that using this light-trapping scheme efficiency improvement of the cells is achieved when these photovoltaic devices are illuminated from both sides, that is, under frontal and rear illumination conditions, since these transparent nanopatterned electrodes act as both reflection and transmission gratings.

2. Preparation of Patterned Electrodes

Diffraction gratings were formed on the TiO_2 nanocrystalline electrode by means of combined soft-lithographic and micropatterning approach that uses commercial structures with blazed profile as masters and a polymeric composite based on vinyl and hidrosilane end-linked polymer, called "hard PDMS" (h-PDMS) as stamp. Further detailes of the patterned process is described in what follows.

1.1. Fabrication of the Stamp

The composite h-PDMS stamps is composed of two layers: a thin, stiff h-PDMS layer supported by a thick, flexible Sylgard 184 layer, that supports easier handling and manipulation.[10] h-PDMS is used to obtain a high fidelity replica of the topology of the master grating.[11]

First of all, the h-PDMS blend is prepared. For that end, 3.4 g of (7–8% vinylmethylsiloxane)–(dimethylsiloxane) (Gelest) copolymer is mixed with two drops of a modulator (1,3,5,7-tetramethylcyclotetrasiloxane) (Gelest) and one drop of platinum divinyltetramethyldisiloxane (Fluorochem Ltd) as catalyst in a Petri dish, then 1 g of (25–30% methylhydrosiloxane)–(dimethylsiloxane) copolymer (Gelest) is added to the mixture, which is gently stirred. The bubbles generated during this process are removed by placing the Petri dish in a dessicator and connect to the vacuum line for 5 min. Immediately, a thin layer of h-PDMS is spin coating over the commercial grating, adjusting the parameters of the spin coater to 500 rpm for 5 s, followed by 1000 rpm for 40 s and cured at 60 °C for 30 min.

The Sylgard 184 (Down Corning) was mixed in a 10:1 ratio of prepolymer and curing agent. Before casting the mixture, it was degassed in a vacuum, and the

two layer stamp is finally cured at 90 °C during 1-2h. After taking the composite mould out of the oven, the stamp is carefully peeled off the master. The mechanical properties of this elastomeric stamp are critical to its ability to transfer a pattern with high fidelity.[12,13]

1.2. Fabrication of Patterned Electrodes based Dye Solar Cells

The sequence for fabricating patterned TiO_2 electrodes is illustrated in figure 5.1. The elastomeric stamp was put into conformal contact with a nanocrystalline titania paste (Dyesol DSL 18NR-T®) deposited onto a transparent conducting substrate. TiO_2 paste was previously softened by heating at 60° during 15 min to improve the imprinting process and to avoid the adherence to the elastomer. Then, the polymer replica was put in contact with the paste and heated up to 130ºC during 15 min while being subjected to a pressure. Next, pressure is maintained other 15 min without heat treatment. Since this technique is a damage-free process for patterning films, the elastomeric stamp could be successfully reused several times for subsequent patterning processes. After the mechanical removal of the template, the nanocrystalline titania film was sintered at 500 ºC to entirely remove the organic components of the paste yielding a surface relief patterned electrode of 4.5 µm thickness.

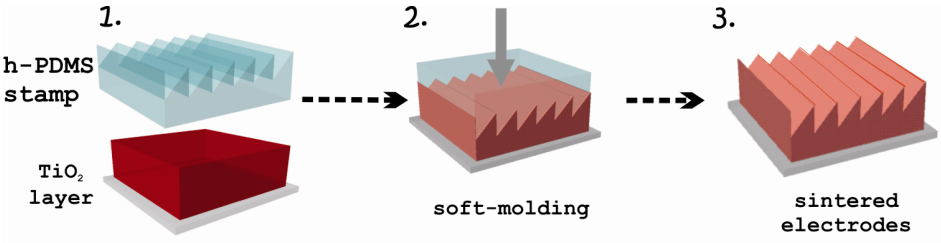

Figure 5.1. Schematic illustration of the fabrication sequence for a 1D optical grating onto TiO_2 layer (1. mold release from master template and TiO2 treated at 60°, 2. pattern transfer to TiO_2 at elevated temperature and pressure and 3. Final sintered electrode).

The solar device fabrication was carried out following the protocol described in the chapter 3.

3. Characterization

The patterned surface of the structures herein presented was characterized by atomic force microscopy (AFM, Park Systems XE-100) working in tapping mode and by field-emission scanning electron microscopy (FESEM, Hitachi S-4800 operating at 2 kV).

Diffraction efficiency was measured using a home-built setup shown in figure 5.2. mounted on an optical bench. A supercontinuum white source (Fianium WhiteLaser) coupled to an acousto-optic tunable filter provides the monochromatic incident radiation. Circularly polarized light beam impinges to patterned electrode with normal incident to the substrate. Several irises are placed between the source and the sample to obtain a small illumination area. Angular resolution of the detection was achieved by selecting the size of the iris and its distance with a collimator lens that focus on an optical fiber. Measurements were performed between 400 and 700 nm, since it is the effective working range of the polarizing filter. Reflectance values are given as the ratio of the diffracted intensity by the periodic structure to the intensity falling directly on the detector from the light source.

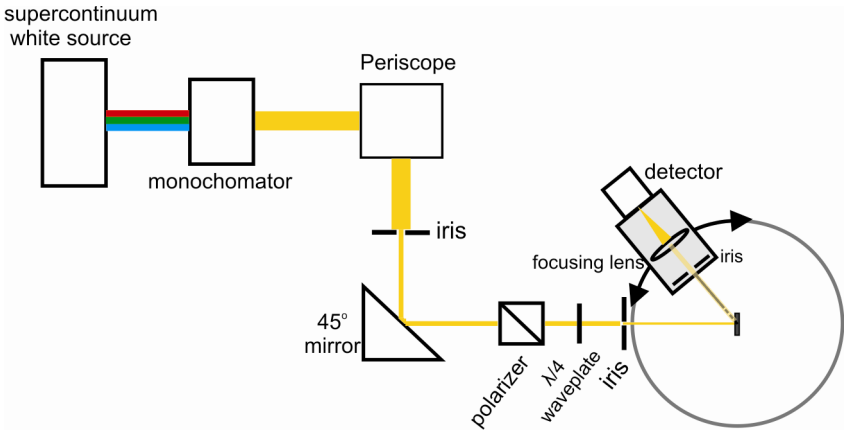

Figure 5.2. Scheme of the home-built setup to measure diffraction efficiency.

The angular measurements were taken using an angular reflectance accessory (Bruker) attached to a Fourier transform spectrophotometer operating in the NIR-Vis region (Bruker IFS-66 FTIR). The diffracted light was harvested by a collection mirror ($\theta=\pm10$ degrees). This study is realized between 15 degrees and 70 degrees due to the limitation in the angular collected setup.

Photovoltaic characterization of the cells was performed as it was explained in chapter 3.

4. Nanopatterned electrodes as diffractive elements

Blazed profile gratings are molded in the back surface of TiO_2 electrodes to behave as light trapping strategy. This shape has been chosen because it favors the channeling of energy to modes diffracted at large angles with respect to the incident direction. The period of the grating (833 nm) was also selected to yield diffraction effects at frequencies matching the absorption band of the dye (lamba max at 533nm) that sensitized the porous electrode, i.e., a ruthenium based dye (N-719). In Figure 5.3, an image of the patterned surface of the TiO_2 electrodes obtained by FESEM is displayed. It can be clearly seen that after the printing process is completed, a periodic arrangement of grooves is created on the electrode surface. In the upper side of the figure a photograph of a diffracted grating patterned electrode is displayed.

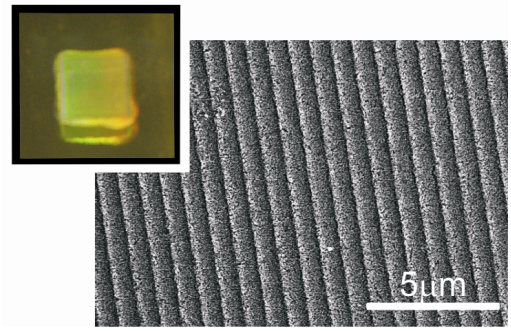

Figure 5.3. Photograph and FESEM image of blazed shape patterned TiO_2 electrode.

However, this one dimensional order is not aware about the profile or the depth of the structure created on top of TiO_2 layer. For analyze this aspect, in figure 5.4 (left) the relief of the grating of both bi-layered stamps and nanocrystalline electrodes obtained by AFM analysis is compared. These images demonstrate that triangular grooves are accurately transferred from the polymeric master to the electrodes. In other words, the patterning of the TiO_2 electrodes has an identical period to it was transferred to the polymeric copy by soft-lithography. Also, it can be distinguish in the height profile plots Figure

5.4 (right) that the depth of the patterns in the electrodes is a little bit shallower than those recorded for the master, which can be due to the sintering process at high temperature after the stamping process. Both features demonstrate the precision and the accuracy of the method employed to obtain one dimensional optical grating onto nanoparticle based TiO_2 layers.

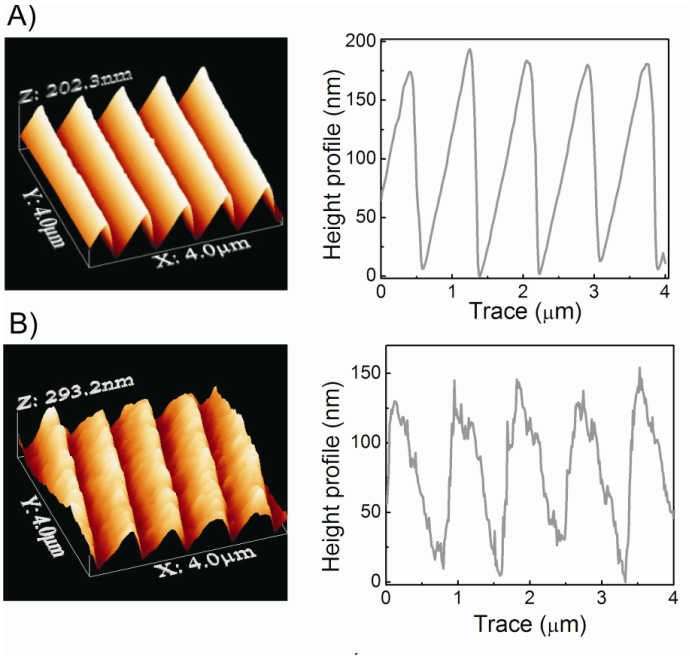

Figure 5.4. AFM images of (A) elastomeric stamp and (B) patterned electrode. Left: 3D representation, right: cross-sectional analysis.

To demonstrate that the patterned electrodes act as diffraction gratings, optical studies were carried out. When monochromatic light incidents on a periodic grating surface it will be diffracted into a finite number of directions, called diffraction orders. The directions of the diffracted orders are independent of the geometry of the modulation and depend only on the ratio of the lattice period to the wavelength of light. . Diffraction from a 1D diffraction grating is illustrated in figure 5.5.A. The diffraction spectrum is created by two distinct phenomena: interference and diffraction, and it can be calculated from the general grating equation which governs the angles of diffraction of a light beam of wavelength λ from a grating of groove spacing, l:[14]

$$m\lambda = l(\sin\theta\, i + \sin\theta r) \qquad 5.1$$

where, m is the diffraction order (or spectral order) of interest, and Θi and Θr are the incidence and reflected angles measured from the grating normal, respectively. In our case (l=833nm), measurements of the first order mode (m=1) were performed with the incident angle fixed at Θi=0º and the patterned electrodes oriented in such a way that diffracted beams were collected. This phenomenom can be appreciated in figure 5.5.B, where four different wavelengths were shone simultaneously on the sample. The observed colored spots belong to the reflected diffracted beams projected on a screen that arise from the patterned sample located at the front of the picture. The angle of the light diffracted is registered by the detector supported at the end of the arm of a rotating stage whose center coincides with the plane of the sample (see experimental). Experimental and theoretical results are plotted in figure 5.5.C. As it can be seen, diffracted light is collected at very oblique angles (>30 degrees). This means that the light reflected by this optical structure travels a large trajectory within the electrode. On the other hand, the dependence of the grating efficiency with the incident wavelength is also studied. The experimental data collected as it was explained in the characterization section was compared with the theoretical efficiency calculated using a code based on a rigorous coupled wave analysis (RCWA) that allows us to model the optical response of the nanocrystalline titania gratings. This analytical method is typically applied to solve scattering from periodic dielectric structures on the scale of a wavelength.[15] The wavelength distribution of the incident field power diffracted by a grating depends on many parameters: power and polarization of the incident light, angle of incidence and diffraction, the (complex) refractive index of the grating, and the groove spacing. For the reflectance efficiency calculus we assume that light hits perpendicularly the blazed profile patterned TiO_2 (n=1.71) and the height of the triangular grooves is 130 nm, as obtained from AFM images. The comparison between experimental and theoretical data is shown in Figure 5.5.D, where the spectral dependence of the relative intensity of the first diffraction orders that are back reflected from the nanocrystalline titania film is displayed. It can be seen, a full agreement between the theory and the experimental data, demonstrating that the electrodes analyzed have grating diffraction properties in the spectral range in which the ruthenium dye absorbs. We have to remark that, as expected from a diffracted structure with a blazed profile, the diffracted efficiency is greatest for that wavelength that is diffracted by the grating in the same direction as it would be reflected by the facets.

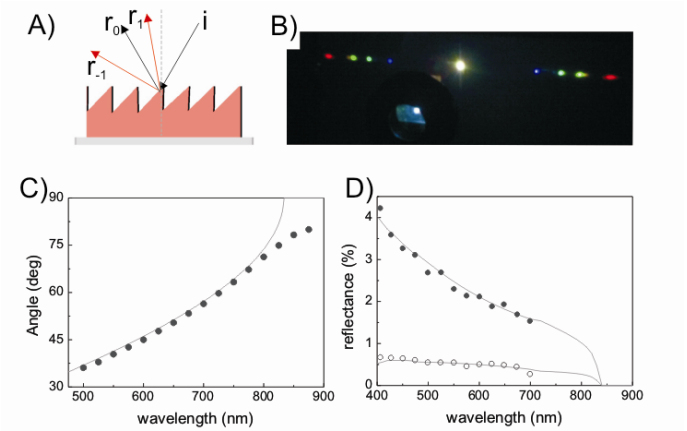

Figure 5.5. A) Diffraction from a 1D periodic structure. B) Photograph of diffraction pattern illuminating the electrode with four different wavelengths simultaneously. C) Angular dependence of the light diffracted. D) Theoretical (grey line) and experimental data (m=-1 black dots, m=1 black open dots) of the spectral reflectance efficiency.

5. Diffractive Grating Electrodes to Improve Dye Solar Cell Performance

The main idea, behind integrating a diffraction grating is increased the path length of waves. The light that propagates to the backside surface of the TiO2 electrode is diffracted in different beam travelling in direction with an angular spread. Hence, the residence time of diffracted photons through the photoanode (and thus their probability of being absorbed) is increased, which leads to the consequent higher photocurrent values.

DSCs containing these periodic nanopatterned electrodes were prepared and their photovoltaic properties characterized to investigate their light harvesting ability. DSCs without any pattern treatment in TiO2 layer, i.e., with flat electrode with the same thickness were fabricated for the sake of comparison. Figure 5.6.B and 5.6.C show the photocurrent-voltage (IV) characteristics and the incident photon to collected electron (IPCE) efficiency spectra of different representative devices employed for this analysis respectively. It can be seen that the patterned TiO2 photoanode presents the highest short circuit photocurrent Furthermore, not only the open circuit photovoltage but also the fill factor of this type of solar device remains unaltered, what showing that surface patterning, has no effect on electron recombination or charge transport.

Cell parameters determined from the IV curves are summarized in table 5.1. IPCE efficiency owing to the diffraction induced by such interface increases the distance that light must travel to return to the front side of the cell.

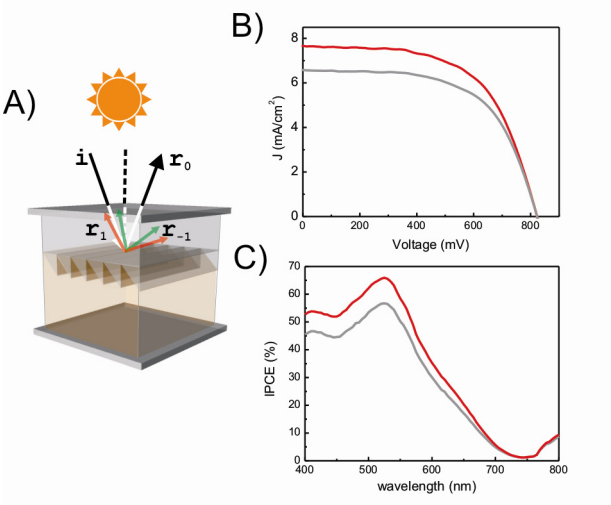

Figure 5.6. A) Scheme of the illumination conditions. B) IV curves and C) incident photon to collected electron (IPCE) efficiencies measured from a flat electrode based cell (grey line) and cells integrating a nanopatterned electrode (red line).

In addition, we would also like to emphasize that these nanopatterned electrodes act as both reflection and transmission gratings. To analyze this latter behavior, IV curves and IPCE efficiency were also measured by irradiating the cells from the counter-electrode side (Figure 5.7). In this configuration light firstly reaches the backside grating, then it is diffracted and finally it abandons the DSC through the photoanode. It can be observed that the cell efficiency is also improved under this illumination condition owing to the angular spread of the transmitted beams within the photoactive TiO2, which elongates the optical path, and thus the probability of the photons to be absorbed. The much lower IPCE measured for shorter wavelength (λ<500 nm) is due to the large optical absorption of the electrolyte in that range. The values of all relevant parameters of the DSCs analyzed here are provided in Table 1. It is worth mentioning that these 1D grating patterned on the electrode surface are the first light trapping structures which gives rise to improve performance of the cells when those are illuminated from both sides.

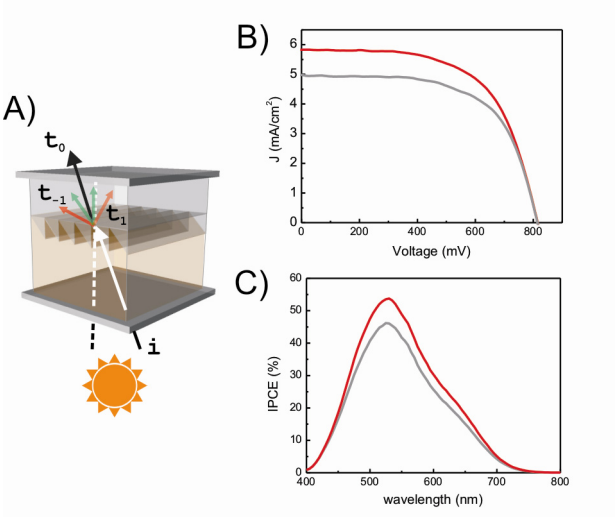

Figure 5.7. A) Scheme of the illumination conditions. B) IV curves and C) incident photon to collected electron (IPCE) efficiencies measured from a flat electrode based cell (grey line) and cells integrating a nanopatterned electrode (red line).

Illumination Side	Electrode type	Jsc (mA/cm2)	V_{oc} (V)	ff (%)	η (%)
Front side	Flat electrode	6.6	823	61	3.3
	Patterned electrode	7.7	822	60	3.8
Rear side	Flat electrode	5	814	63	2.5
	Patterned electrode	5.8	815	61	2.9

Table 5.1. Values attained for the short circuit photocurrent density (Jsc), the open circuit photovoltage (Voc), the fill factor (ff), and the power conversion efficiency (□) for the set of DSCs.

6. Conclusions

In this chapter, a simple light trapping strategy is presented by fabricating novel one dimensional optical grating on the backside of TiO_2 electrodes in the shape of blazed profile.

A new technique to obtain the 1D TiO2 photoanode structures has been developed by means of a combined soft-lithography and micro-contact printing

approach. AFM studies confirm the suitability of this method to pattern TiO2 nanocrystalline films.

Comparison between different experimental techniques and theoretical results show excellent agreement and demonstrate that the patterned electrodes show diffraction grating properties.

Efficiency of casted electrode based DSCs increased primarily as a result of the enhancement of Jsc, indicating that these periodic structures induce further photon absorption in photoactive layers by increasing the optical path length and light trapping compared to that of a solar cell on a smooth surface. Finally the behavior of these transparent electrodes as transmission grating has been evaluated achieving also an improvement in the performance of the cell.

7. References

[1] P. Bermel, C. Luo, L. Zeng, L.C. Kimerling, J.D. Joannopoulos, Opt. Express, 2007, **15**, 16986.

[2] L. Zheng, P. Bermel, Y. Yi, B.A. Alamariu, K.A. Broderick, J. Liu, C. Hong, X. Duan, J, Joannopoulos, L.C. Kimerling*, Apl. Phys. Let.*, 2008, **93**, 221105.

[3] L. Zeng, Y. Yi, C. Hong, J. Liu, N. Feng, X. Duan, L. C. Kimerling, B.A. Alamariu, *Appl. Phys. Lett.* 2006, **89**, 111 111.

[4] S.I. Na, S.S. Kim, J. Jo, S.H. Oh, J. Kim, D.Y. Kim, *Adv. Funct. Mater.*, 2008, **18**, 3956.

[5] M. Wellenzohn, R. Hainberger, *Opt. Express*, 2012, **20**, 20.

[6] R. Dewan, D. Knipp, *J. Appl. Phys.*, 2009, **106**, 74901.

[7] J. Kim , J. K. Koh , B. Kim , J. H. Kim , E. Kim , *Angew. Chem. Int. Ed,.* 2012 , **51** , 6864 .

[8] S. Wooh, H. Yoon, JH. Jung, YG. Lee, J.H. Koh, B.Lee, Y.S. Kang, K. Char, *Adv. Mat.*, 2013, **25**, 3111.

[9] D. Barettin, A. Di Carlo, R. De Angelis, M. Casalboni, P. Prosposito, *Optics Express*, 2012, **20**, 889.

[10] D. Quin, Y. Xia, G.M. Whitesides, *Nature protocols*, 2010, **5**, 491.

[11] H. Schmid, B. Michel, *Macromolecules*, 2000, **33**, 3042.

[12] T.W. Odom, J.C. Love, D.B. Wolfe, K.E. Paul, G.M. Whitesides, *Langmuir,* 2002, **18**, 5314.

[13] TW. Lee, O. Mitrofanov, J.W.W. Hsu, *Adv. Funct. Mater.*, 2005, **15**, 1683.

[14] C. Palmer and E. Lowen, *Diffraction Grating Handbook (*Richardson Grating Laboratory, Rochester, NY, 2002).

[15] M.G. Moharam, T.K. Gaylord, *J. Opt. Soc. Am.* 1981**, 71**, 811.

Specular Reflectance Porosimetry

Appendix 1

Specular Reflectance Porosimetry (SPR) is an optical technique for investigating the porous mesostructure of thin films, which is based on the analysis of the variations of the specular reflectance of such films when they are exposed to different vapor concentrations in a closed chamber. SRP requires, as in the case of ellipsometric porosimetry, plane parallel and optically homogeneous films in order to avoid offaxis reflections caused by variations in the surface curvature or diffuse scattering, respectively.

Experimental SRP setup is schematized in Figure 1.A. The chamber where the sample is situated possesses a flat quartz window through which the reflectance spectra at quasi-normal incidence were recorded. A white light source and a Fourier transform visible□ near-infrared spectrophotometer (Bruker IFS-66), equipped with a Si photodiode detector, attached to a microscope operating in reflection mode were employed to carry out all of the optical characterization herein presented. A 4× objective with a 0.1 numerical aperture (light cone angle ±5.7°) was used to illuminate the films and collect the light reflected by them. To control the vapor pressure in the sample chamber, a bulb containing isopropyl alcohol is connected to it through a needle valve. The internal pressure of the chamber was measured with a dual capacitance manometer (MKS model PDR 2000). A second needle valve connects a vacuum pump to the sample chamber. Samples have to be annealed at 120 °C overnight to remove any moisture from the voids in the porous structures before carrying out the gas adsorption-desorption process. Then, samples are introduced into the chamber and keep under dynamic vacuum (10^{-2} Torr) for half an hour. After that, the system is closed and pressure in the chamber monitored to confirm that there are no leaks. The first reflectance spectrum is obtained at the lowest pressure value achievable (P_0) in the chamber. Then, the pressure in the chamber is gradually increased by opening the needle valve that connects it to the bulb containing the isopropanol until the desired pressure is reached. Once equilibrium is reached, reflectance spectra are measured at each fixed pressure, P. This process was repeated sequentially at different solvent vapor pressures until saturation pressure (P_s) was reached. Desorption experiments are

conducted following the same protocol, with a gradual decrease in the pressure being obtained by opening the valve connected to the vacuum pump. Again, spectra are taken at slowly decreasing pressures until the initial value is attained.

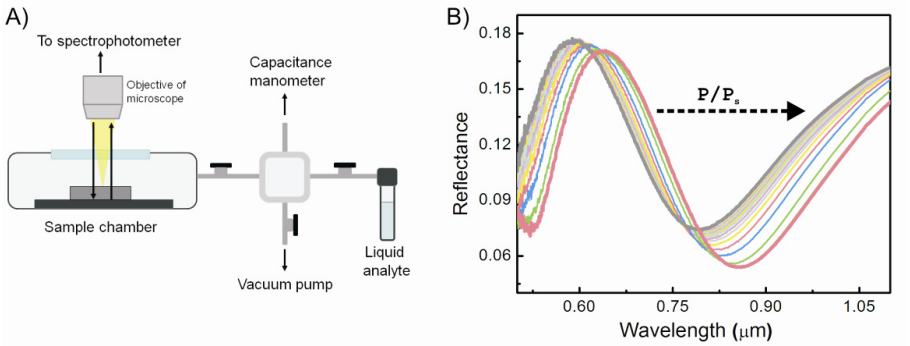

Figure 1. *A) Scheme of the specular reflectance porosimetry setup. B) Reflectance spectra of a mesoporous SiO_2 nanoparticle film exposed at different pressures of isopropanol vapor in the chamber. The direction of the spectrum shift caused by the pressure increase is indicated by an arrow.*

The evolution of the specular reflectance spectra, measured at normal incidence when relative pressures of isopropanol are varied from 0 to 1, is shown in Figure 1.B. As the vapor pressure in the chamber increases, gas molecule adsorption onto the pore walls occurs. Eventually, capillary condensation within the pores takes place. Both phenomena lead to an increment in the effective refractive index of the film, shifting the intensity oscillation to higher wavelengths, as can be readily seen in Figure 1.B, the direction of the spectrum shift caused by the pressure increase is indicated by an arrow. All measurements were made at room temperature. We used isopropanol as an adsorbate to characterize the mesostructure of the samples. This low-molecular-weight alcohol has been previously proven to yield excellent results for the analysis of the vapor sorption properties of nanoparticle based multilayers.[1]

To calculate the effective refractive index of the film from its specular reflectance spectrum attained at each pressure step, a code written in MatLab based on the transfer matrix formalism[2] was employed to fit the experimental data and extract information from the optical constants. We consider the thickness and the effective refractive index of the thin film as fitting parameters

and a linear least-squared method to fit the experimental reflectance. An example of an experimental curve obtained from the np-SiO_2 at a specific isopropanol partial pressure (P/Ps=0.65) and the corresponding fitted reflectance spectrum is shown in Figure 2.

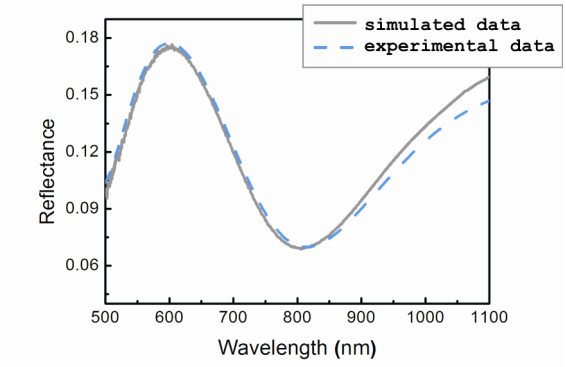

Figure 2. *Simulated (blue dashed line) and experimental reflectance spectrum of a SiO_2 monolayer at partial pressure (P/Ps) 0.65.*

The fittings of the set of reflectance spectra allow us to calculate the variation of the refractive index as the vapor pressure in the chamber increases and, therefore, the evolution of the free pore volume fraction, as explained in what follows. When the spatial inhomogeneity of the dielectric constant in the film is small compared to the wavelength of light, the concept of the effective refractive index is meaningful as far as far-field transmission and reflection coefficients are concerned. Thus, the effective refractive index of an inhomogeneous medium can be determined given the properties of its constituents under certain assumptions. There exist a vast collection of choices in the scientific literature to find the effective dielectric function. In our case, we apply the Bruggeman equation for a three-component dielectric medium,[3] which is based on an effective medium theory.[4] We consider our inhomogeneous medium to be composed of inclusions of two different constituents, namely, the material of which the pore walls are made, with refractive index n_{wall}, and the adsorbed solvent present in the pores when the pressure starts increasing, $n_{solvent}$, embedded in an otherwise homogeneous matrix of $n_{medium} = 1$. The effective refractive index of the composite material, n, can then be obtained from Equation 1.

$$f_{wall}\frac{n_{wall}^2-n^2}{n_{wall}^2+2n^2}+f_{solvent}\frac{n_{solvent}^2-n^2}{n_{solvent}^2+2n^2}+f_{medium}\frac{n_{medium}^2-n^2}{n_{medium}^2+2n^2}=0 \qquad 1$$

Where f_{wall}, $f_{solvent}$ and f_{medium} are the volume fractions of the material composing the pore walls, the solvent and the surrounding medium, respectively. Knowing n_{wall}, (taken as n_{SiO2}=1.45) and $n_{solvent}$ ($n_{isopropanol}$=1.37), and extracting the effective refractive index of the film, n, from the fittings of the specular reflectance measured under vacuum ($f_{solvent}$=0) and by means of Equation 1, we can estimate f_{wall} and thus the total pore volume (f_{medium}=f_{pore}=1-f_{wall}) of the starting material.

Then, from the effective refractive index of the film obtained at different pressures, we can estimate the volume fraction occupied by the adsorbed, and eventually condensed, species, $f_{solvent}$, since we can write f_{medium}=1-f_{wall}-$f_{solvent}$, leaving $f_{solvent}$ as the only unknown parameter. The ratio $f_{solvent}/f_{pore}$ is the ratio between the volume occupied by the adsorbed species, V_{ads}, and the originally free pore volume, V_{pore}. The refractive index of the interstitial sites, n_{pore}, and the quotient V_{ads}/V_{pore} are plotted *versus* the solvent partial pressure, P/P_S, in Figure 3, for increasing (adsorption) and decreasing (desorption) pressure in the chamber. The values taken from the adsorption cycle are drown as black dots, and those extracted from desorption measurements are plotted as gray ones.

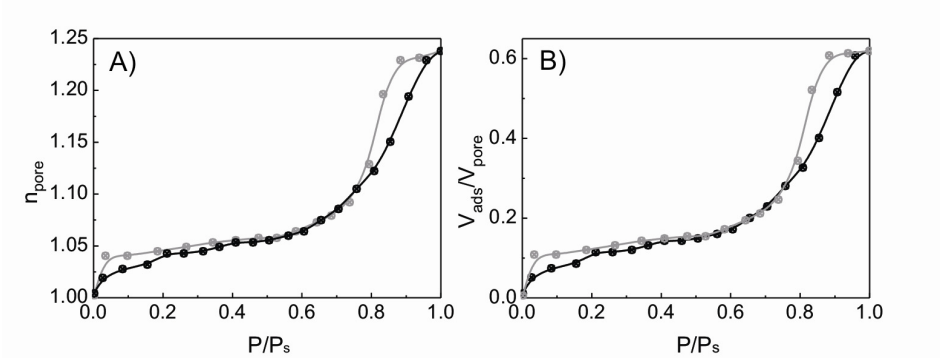

Figure 3. *Adsorption (black dots) and desorption (gray dots) isotherms showing the variation of the refractive index (A) and the volume fill fraction of solvent (B) in the porous network for films made of packed SiO_2 nanoparticles.*

The pore size distribution (PSD) of a mesoporous film is obtained using this technique, which is based on the assumption that a layer of adsorbed molecules of the alcohol is formed at low partial pressures and its condensation is governed by Kelvin's law,[5] which has the form,

$$\ln\left(P/P_s\right) = -\frac{2\gamma V_L}{RT}\frac{1}{r_K} \qquad 2$$

where P/P_s is the ratio between the condensation pressure in a pore of radius r_K and the saturation pressure at a defined temperature T, V_L and γ are the molar volume and the surface tension of the adsorbed liquid, respectively, and R is the gas constant. This equation is considered to be valid for analyzing pore ratios of between 1 and 20 nm. This upper value limits the validity of Kelvin's law to $P/P_s < 0.95$. Corrections to this model to include the effect of pore shape and liquid-solid phase interactions have been thoroughly discussed.[6] For the purpose of this chapter, we will restrict ourselves to the standard model, although modifications based on more precise assumptions could be implemented. The PSD of a specific film can be obtained from the analysis of the adsorption□desorption curves like the presented in Figure 3. After Equation 2, at each P/P_s value, the fraction of pores with the corresponding Kelvin radius, r_K, is filled by solvent condensation, so large variations in the volume occupied by adsorbed species at a given P/P_s indicate the presence of a large fraction of pores of the corresponding r_K. Therefore, there is a direct correlation between the fraction of pores of a given Kelvin radius present in the film and the slope of the V_{ads}/V_{pore} versus P/P_s curve plotted in Figure 3. The Kelvin equation does not take account of any fluid-walls interaction. The consequence of this latter is that there exists an absorbed liquid like layer on the pore wall, which thickness is known t. The actual pore radius, r_{pore}, is the result of adding r_K to t, the thickness of a layer adsorbed on the walls of the porous network at low pressures ($P/P_s < 0.3$). The expression chosen to calculate this parameter is based on the BET (Brunauer, Emmet, and Teller) equation:[5,7]

$$t = \frac{d_0\, KC\left(\frac{P}{P_S}\right)}{\left[1-KC\left(\frac{P}{P_S}\right)\right]\left[1+K(C-1)\left(\frac{P}{P_S}\right)\right]} \qquad 2.3$$

In this expression, K is a fitting parameter that varies between 0.7 and 0.76 depending on the solvent used, and its estimation is based on the assumption that the number of molecular layers at P_s in an open porous material is finite (five or six monolayers),[5] C is the BET constant, and d_0 is the thickness of a monolayer of solvent molecules. In this analysis, we consider that d_0 is equal to the diameter of a single molecule of the vapor used as a test probe, which is

estimated from the molar volume.[8] The *C* constant depends on the interaction between the solvent and the wall of the film, and it is extracted from the BET plot,[9] which can be expressed as

$$\frac{P}{V_{ads}(P-P_s)} = \frac{1}{V_m} + \frac{C-1}{V_m C}\frac{P}{P_S} \qquad 2.4$$

where Vm is the ratio between the volume of a monolayer adsorbed on the pore walls and the total porous volume of the sample. This linear relation is valid for the ratio pressures (P/P_s) in the range of 0.05□ 0.3, where no capillary condensation occurs.

The PSD of a film is the result of represented the fraction obtained of pores related with the isotherm slope versus $r_{pore} = r_K + t$.

References

[1] S. Colodrero, M. Ocaña, A. R. González-Elipe, H. Míguez, Langmuir, 2008, 24, 9135.

[2] G. Lozano, S. Colodrero, O. Caulier, M. E. Calvo, H. Míguez, J. Phys. Chem. C 2010, 114, 3681.

[3] H.C. van de Hulst, Light Scattering by Small Particles; Dover Publications: New York, 1981.

[4] N. Nagy, A. Deak, Z. Horvolgyi, M. Fried, A. Agod, I. Barsony, Langmuir, 2006, 22, 8416.

[5] S. J. Gregg, K. S. W. Sing, Adsorption, Surface Area and Porosity; Harcourt Brace and Co.: Orlando, FL, 1997.

[6] C. Boissiere, D. Grosso, S. Lepoutre, L. Nicole, A. Brunet Bruneau, C. Sanchez, Langmuir, 2005, 21, 12362.

[7] M. R. Baklanov, K. P. Mogilnikov, V. G. Polovinkin, F. N. Dultsev, *J. Vac. Sci. Technol., B,* 2000, **18**, 1385.

[8] CRC Handbook of Chemistry and Physics, 88th ed. Lide, D. R., Ed.; CRC Press: Boca Raton, FL, 2008.

[9] S. Brunauer, L. S. Deming, W. S. Deming, E. Teller, J. Am. Chem. Soc. 1940, 62, 1723.

General Conclusions

A method to increase both the porosity and the pore size distribution of nanoparticle films has been developed. This goal is achieve by the use of polyethylene glycol 2000 as porogen, which after be removed creates large cavities inside the film. Multilayered structures composed of these highly porous layers have proved that present photonic crystal properties. Furthermore having a more open interconnectivity porous network gives rise to a decrease of the diffusion resistance of species through the photonic structure. The integration of these new designed 1DPCs to DSCs improves the performance of the cells.

By coupling a 1DPC whose Bragg peak covers the whole visible range to a DSC similar values of photocurrent and efficiency to those obtained with a scattering layer are obtained, with the added value of preserving the semitransparency of these cells, which is of great interest for building integrated photovoltaic (BIPV) applications.

The behavior of these 1DPC based DSCs as the incident light angle was implemented thinking about their future outdoor applications. We show that the characteristic cosine losses as a result of the angular illumination can be partially compensated by the interplay of this effect with the angular variations of the Bragg peak position when a photonic crystal is implemented in DSC.

A simple light trapping strategy has been also presented, consisting on the fabrication of novel one dimensional optical grating on the backside of TiO2 electrodes in the shape of blazed profile. Achieving an improvement of the performance of the cell when it is illuminated not only under front side but also under rear side.

Materiales Ópticos Nanoestructurados para Celdas Solares de Colorante

Resumen en Español

1. Introducción a las Celdas Solares de Colorante

La gran demanda energética mundial, así como la escasez de combustibles fósiles han impulsado el desarrollo de alternativas energéticas, tales como la tecnología fotovoltaica, basadas en el aprovechamiento de fuentes de energía renovables. La mayoría de instalaciones fotovoltaicas usadas hoy en día para transformar la energía solar en eléctrica están integradas por celdas de unión de estado sólido de silicio cristalino. Sin embargo, el elevado coste de producción e instalación de este tipo de celdas solares ha motivado la búsqueda de nuevas alternativas basadas en tecnologías más baratas y que implican una reducción en la cantidad de material empleado.

Entre las principales propuestas, cabe destacar las celdas solares de colorante o DSCs, del inglés Dye Solar Cells. Estos dispositivos son distinguidos por su bajo coste de producción, por la posibilidad de ser construidas sobre soportes flexibles y diseñadas en una gran variedad de colores sin perder su transparencia. El valor estético que ello supone es la clave para futuras aplicaciones en el campo de la tecnología fotovoltaica para integración arquitectónica. Estos dispositivos se presentaron por primera vez en 1991 por M. Grätzel y B. O´Regan.[1]

Las DSCs combinan los procesos de absorción óptica y separación de carga a través de la asociación de un colorante y un semiconductor de amplio band gap. La clave de estos dispositivos es la combinación de moléculas de colorante ópticamente activas y el uso de capas meso-porosas formadas por nanocristales de TiO_2, con un tamaño de partícula en torno a 20 nm con alta superficie activa. En la figura 1 está esquematizada la configuración estándar de estas DSCs basadas en electrolito líquido. Como electrodo de trabajo se emplea una lámina porosa de TiO_2 depositada sobre un sustrato de vidrio que posee una lámina de óxido conductor y transparente de FTO (del inglés

Fluorinated doped Tin Oxide), sobre la superficie de esta película se ancla una monocapa de moléculas de colorante, típicamente basado en complejos de rutenio. Como contra-electrodo del dispositivo se utiliza el mismo tipo de sustrato conductor recubierto, en este caso, de una película delgada de platino coloidal, el cual actúa como catalizador de la reacción de oxido-reducción del par redox yoduro/triyoduro que compone el electrolito líquido y que finalmente embebe toda la estructura porosa.

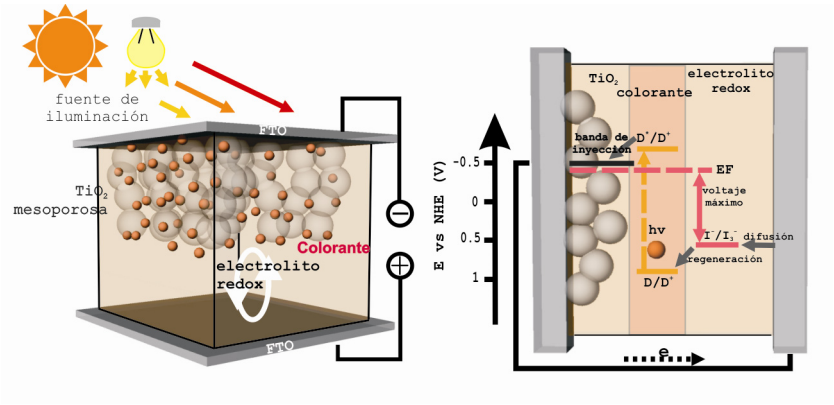

Figura 1. A) Esquema y B) diagrama de los niveles energéticos de los distintos componentes implicados en el funcionamiento de una DSC basada en electrolito líquido.

El funcionamiento de una DSC viene determinado por los niveles energéticos de sus distintos componentes (Figura 1.B).[2,3] Los fotones que llegan a la celda excitan los electrones presentes en el nivel HOMO del colorante hasta el estado LUMO, estos electrones son a su vez inyectados a la banda de conducción de la TiO_2 y transportados hasta el vidrio conductor. Por otra parte, las moléculas de colorante oxidadas son regeneradas por la especie I^- presentes en el electrolito, las cuales se oxidarán para dar lugar a especies I^{3-}. Estas últimas difundirán hacia el contra-electrodo donde serán de nuevo reducidas, completándose así el circuito externo de los electrones.

Caracterización fotovoltaica

Las técnicas de caracterización estándares de las DSCs comprenden las medidas de las curvas corriente-voltaje (curvas IV) características del dispositivo y de la eficiencia espectral de conversión de fotones en electrones o IPCE (del inglés Incident Photon to Collected Electron efficiency).

Las curvas IV representan la respuesta integrada de la celda a todas las longitudes de onda simultáneamente. Experimentalmente, estas curvas se obtienen variando la resistencia de un circuito externo (Figura 2.A). A partir de estas curvas se obtienen los parámetros fundamentales de la celda; la corriente a corto circuito (I_{SC}), el voltaje a circuito abierto (V_{OC}), el ff (del inglés fill factor) y la eficiencia de conversión de energía solar en eléctrica (η).

Por otra parte, las medidas de IPCE cuantifican cuantos fotones que inciden sobre la celda de una longitud de onda determinada se transforman en electrones recogidos por el electrodo. Este factor depende de las propiedades eléctricas y ópticas del dispositivo.[4,5] La figura 2.B ilustra el espectro de absorción óptico correspondiente a una lámina semitransparente de TiO_2 sensibilizada con el colorante de rutenio N719, materiales que se van a usar durante esta tesis doctoral.

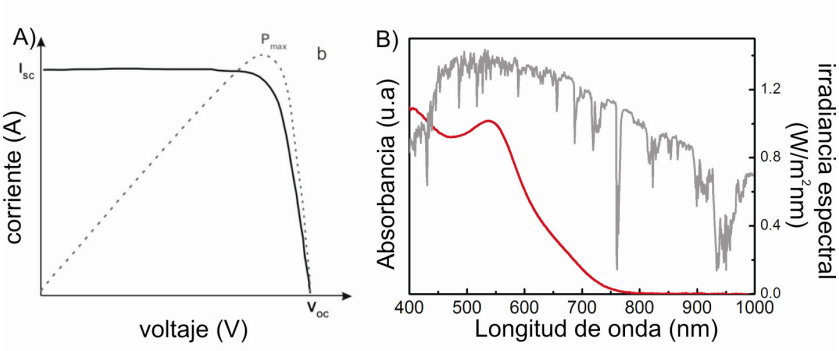

Figura 2. A) Curva IV de una DSC y los principales parámetros característicos que determinan la eficiencia del dispositivo (I_{SC}, V_{OC}, ff). B) Comparación entre la irradiancia correspondiente al espectro solar AM 1.5 y la absorción típica de una lámina de TiO_2 sensibilizada con N719.

Principales estrategias para aumentar la absorción óptica de las DSCs

El diseño de estas celdas solares de colorante es clave para conseguir un funcionamiento óptimo de las mismas. Mediante el uso de distintos elementos ópticos se consigue aumentar el tiempo de residencia de los fotones en la lámina fotoactiva y de este modo aumentar la eficiencia de recolección de luz y por lo tanto la eficiencia del dispositivo.

Tradicionalmente, el modo de conseguir este aumento del camino óptico ha sido empleando partículas de TiO_2 del orden de la longitud de onda de la radiación incidente [6]

Los primeros trabajos destinados a tal fin se basaron en conseguir un aumento del camino óptico de la luz para aquellos fotones que aún no han sido absorbidos como consecuencia de la difusión de la luz Estas partículas se pueden o mezclar con el electrodo o depositar en su superficie trasera formando una capa adicional de nanopartículas (Figura 3). En este punto es importante mencionar que los valores más altos de eficiencia publicados hasta el momento para este tipo de celdas solares hacen uso de la capa extra de partículas grandes de TiO_2.[7-11] Diversos estudios teóricos han tratado de modelar el comportamiento de la luz ante la presencia de estas partículas dispersoras, con el fin de encontrar el diseño óptimo del dispositivo.[12-17] Sin embargo, el uso de estas partículas como medio para incrementar la eficiencia de recolección de luz vuelve a la celda opaca, impidiendo su uso en dispositivos fotovoltaicos tales como ventanas. Además de estos diseños basados en el uso de partículas grandes, otros elementos dispersores de luz más complejos tales como multicapas difusoras[18] o partículas con estructuras porosas jerarquizadas[19,20] también se están desarrollando para su inclusión en las celdas solares de colorante.

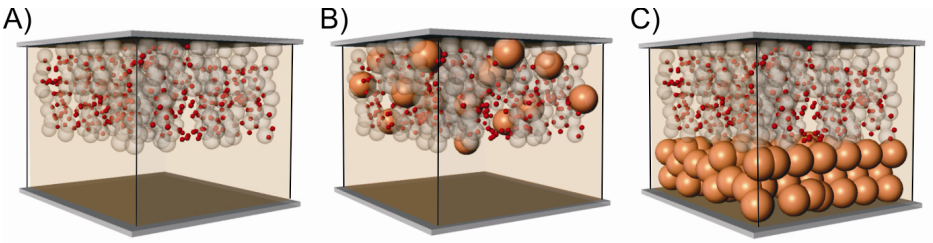

Figura 3. *Esquemas correspondientes a A) una celda estándar y dos celdas basadas en partículas difusoras B) incorporadas a la lámina fotoactiva y C) depositadas formando una capa extra sobre el electrodo.*

Otra propuesta, investigada recientemente es la inclusión de estructuras plasmónicas en las DSCs. De esta manera se pretende aprovechar la alta capacidad difusora de las partículas metálicas para aumentar el camino óptico de la luz en la capa activa y el campo cercano creado para aumentar la absortividad molar del colorante.[21,22] A pesar de que el uso de estas partículas habían dado buenos resultados en otros tipos de celdas solares,[23,24] para su empleo en las DSCs había que tener alguna consideración mas, y es que se

encontró que el contacto directo entre el electrolito y las partículas metalicas daba lugar a la recombinación de los electrones fotogenerados corroyendo el metal.[25] Para resolver este problema las partículas metalicas se cubrieron de una capa de un material (TiO_2 o SiO_2) que las aislara del entorno, para de esta manera conseguir un buen funcionamiento de la celda.[26-28] En la figura 4 se representa un esquema de este diseño de celda junto a los obtenidos.

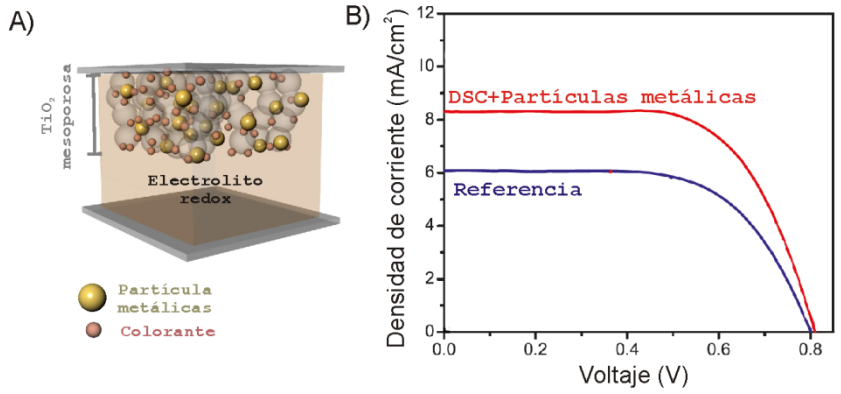

Figura 4. A) esquema de una DSC en la cual se han incluido partículas metálicas. B) Curvas IV de dos celdas, una referencia y otra en la que se han añadido partículas de Ag@TiO_2. (Extraído de la referencia 27)

Como alternativa al uso de estructuras desordenadas como las anteriormente mencionadas para amplificar la absorción óptica de las DSCs surgen diferentes estructuras periódicas que aprovechan distintos fenómenos de interferencia de la luz para mejorar el rendimiento de dichos dispositivos.

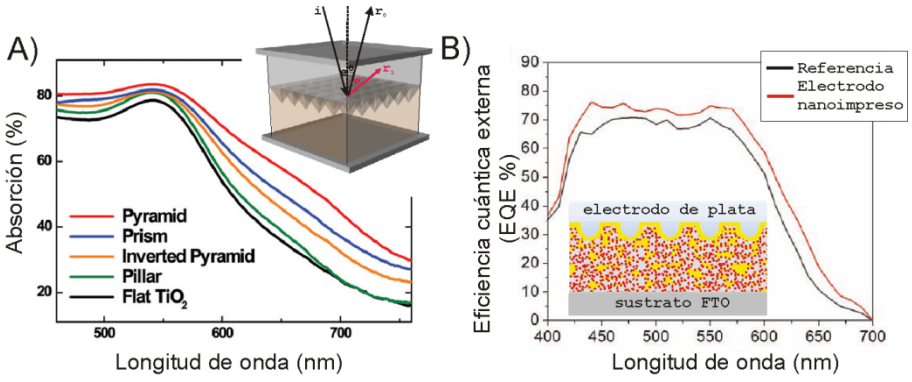

Figura 5. *Efecto que tiene el empleo de A) una red de diffraccion y B) una red metálica tienen sobre la absorción de luz de una celda solar de colorante. (Estraido de las referencias 30 y 32 respectivamente).*

Por un lado, el uso de redes de difracción creadas en la superficie trasera del electrodo se ha presentado recientemente como un prometedor candidato para aumentar la eficiencia de recolección de la luz a través del aumento del paso de luz en el electrodo por fenómenos de difracción de los fotones no absorbidos.[29,30] Una variante de esta estrategia es el uso de redes metálicas, de esta forma el plasmon superficial del metal es más fácilmente excitado gracias a la presencia de la red periodica. Esta característica es la que hace que estas estructuras sean interesantes para mejorar la absorptancia del dispositivo solar.[31,32] En la figura 5 podemos observar varios ejemplos de diseños de las celdas solares de colorantes basadas en el uso de redes periódicas.

Por otra parte, el uso de materiales dieléctricos con un ordenamiento periódico del índice de refracción ha sido también propuesto como alternativa para aumentar la absorción óptica de celdas solares. Los fenómenos interferenciales creados por estos elementos periódicos, conocidos como cristales fotónicos, determinarán la propagación o no de determinados rangos de frecuencias a través de la estructura, reflejándose unos y transmitiéndose otros, lo que se traduce en la aparición de un máximo en el espectro de reflectancia especular.[33] El primer ejemplo de la incorporación de este tipo de arquitecturas en DSCs fue presentado en 2003 por S. Nishimura et al., los cuales lograron amplificar la fotocorriente de este tipo de dispositivos acoplando un ópalo inverso al electrodo de nanopartículas.[34] Este aumento se puede atribuir a la reflexión de fotones cuyas frecuencias coinciden con las del band gap del ópalo hacia el electrodo sensitivizado con colorante,[35] por lo tanto la amplificación de la absorción óptica tiene lugar en el rango espectral del band gap fotonico. El hecho que este rango espectral sea fácilmente controlable a hizo que el interés hacia este tipo de elemento óptico para la mejora del funcionamiento de las DCS creciera.

En este contexto surgen los cristales fotónicos unidimensionales (1DPC) como amplificadores de la eficiencia de recolección de luz de las DSCs.[36] Los cristales fotónicos empleados para este fin se construyen alternando capas de nanopartículas de SiO_2 y TiO_2.[37] La principal novedad de esta nanoestructura que la hace idónea para su integración en DSCs es la red porosa que aparece como resultado de apilar partículas permitiendo el paso del electrolito líquido a

su través. En este caso el rango espectral al cual aparece el pico de reflectancia y por tanto en el que se produce el aumento de fotocorriente de la celda puede ser fácilmente controlado a partir del espesor de las capas que forman la estructura. De esta forma la semitransparencia de estas celdas se puede preservar permitiendo el paso de luz de altas longitudes de onda, como revelan los espectros de transmitancia de la figura 6.A. Esto es debido a que, para las distintas estructuras fotónicas acopladas a las celdas solares, se mantiene una ventana de transparencia en el rango de mayores longitudes de onda del espectro visible. Por el contrario, el uso de láminas difusoras, las cuales dispersan la luz sin una dirección preferencial, daría como resultado celdas solares prácticamente opacas, lo cual impediría su uso en ciertas aplicaciones potenciales, tales como en módulos de ventana o de decoración interior. Asimismo en la figura 6 B se muestran las curvas IV de estos dispositivos.

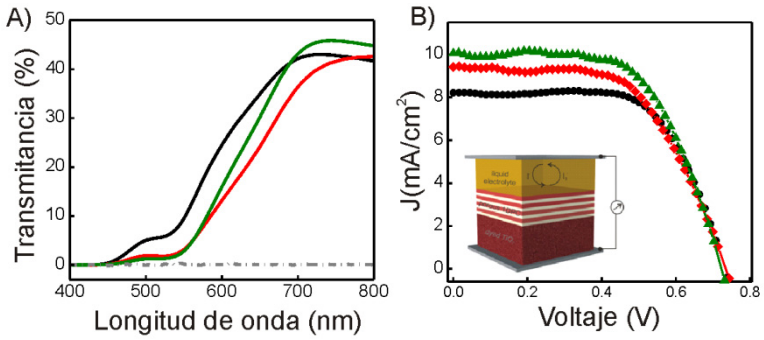

Figura 6. A) La transmitancia para DSCs acopladas a una lámina difusora (línea gris) y a una estructura porosa de 1DPC (línea verde). Con objeto de facilitar su compraración, se presenta también la curva IV correspondiente a una celda de referencia. B) Curvas IV características medidas de una celda referencia (línea negra) y de dos celdas en las que se han integrado dos 1DPC distintos(líneas roja y verde). (Extraidas de la referencia 36).

A pesar de los buenos resultados obtenidos con el acoplamiento de estos cristales unidimensionales, había señales de que existían problemas de difusión del electrolito: por un lado el empleo de 1DPC con mayor número de capas, factor que aumentaba la reflectancia del sistema, no daba lugar al aumento en fotocorriente que teóricamente se esperaba[38] y por otro la disminución del fill factor de la celda. (Figura 7)

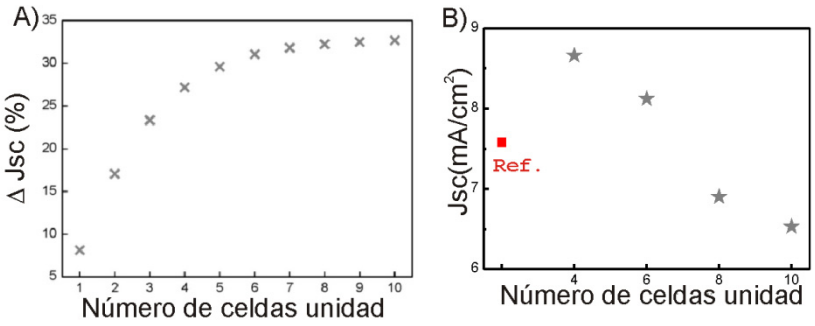

Figura 7. A) aumento teórico de la fotocorriente frente al número de capas que constituyen el cristal fotónico. (Extraído de la referencia 38) B) Datos experimentales de fotocorriente frente al número de celdas unidad.

2. Motivacion y objetivos de esta tesis

A raíz de los resultados obtenidos al acoplar un cristal fotónico unidimensional a una celda solar de colorante y teniendo siempre presente el potencial de estas celdas para futuras aplicaciones como módulos fotovoltaicos para su integración arquitectónica se plantea esta tesis.

El principal reto que se planteaba era la mejora de la difusión del electrolito a través de la estructura fotónica para así optimizar el funcionamiento de las DSC basadas en 1DPCs. Los objetivos que se persiguieron para la elaboración de la tesis denominada "materiales nanoestructurados para la celda solar de colorante" fueron:

Desarrollo de un procedimiento experimental que permitiera aumentar la porosidad y el tamaño de partícula de capas de nanopartículas. Esto a su vez implica el desarrollo de una técnica de porosimetría para analizar estas películas. Además del estudio de celdas que incorporen estos 1DPC de porosidad aumentada.

Integrar un cristal fotónico pancromático en la celda, cuyo pico de reflectancia cubra el espectro visible de luz, y de esta forma imitar el comportamiento de una lámina difusora de partículas.

Realizar un estudio completo del comportamiento de las DSCs basadas en 1DPC con el ángulo de iluminación, pensando en su posible aplicación como módulo de ventana.

Desarrollar una nueva alternativa basada en el uso de redes de difracción para el aumento de la eficiencia de recolección de luz de las DSCs.

3. Obtención de cristales fotónicos unidimensionales de gran porosidad

El primer paso hacia la optimización de los cristales fotónicos unidimensionales para su uso en celdas solares de colorante es la mejora del transporte de masa a su través. Para tal fin, es necesario modificar tanto la porosidad como la distribución de tamaño de poro de cada una de las capas que forman la estructura óptica. Un método empleado dentro del campo de catálisis y sensores para generar poros de un determinado tamaño en láminas delgadas consiste en la incorporación de polímeros orgánicos, también denominados porógenos, dentro de la matriz que contiene el material precursor. Una vez depositada la capa, un tratamiento térmico a altas temperaturas permite eliminar el material orgánico presente en la misma, dejando así poros abiertos en la estructura. [39,40]

Los materiales base para la construcción de estos espejos dieléctricos altamente porosos y reflectantes fueron suspensiones coloidales de nanopartículas de SiO_2 y TiO_2 y el porógeno elegido polietilenglicol 20000 (PEG). Este polímero fue seleccionado porque se ha demostrado que disminuye el número de defectos que aparece al utilizar como técnica de deposición el spin coating.[41] Para estudiar la influencia del PEG sobre las estructuras fotónicas se emplearon distintas relaciones en peso de PEG : nanopaticulas. Para eliminar el porógeno y crear las cavidadades tras la deposición de la capa de PEG/nanopartículas la estructura se calienta a 300 ˚C durante 15 min.

Previamente a la fabricación de los cristales fotónicos de alta pororsidad se caracterizan las monocapas que se obtienen por deposición de las suspensiones de SiO_2 y TiO_2 con distinta cantidad de porógeno por porosimetría de reflectancia especular (SRP, del inglés specular reflectance porosimetry). Esta técnica fue desarrollada en mi grupo de investigación y se basa en el análisis del cambio gradual de la respuesta óptica de una lámina delgada frente a la presión de vapor controlada de un líquido volátil.[42] En resumen, el espectro de reflectancia en el rango visisble que produce una lámina delgada depende del índice efectivo de esta, el cual va a cambiar a medida que la red porosa de tal lámina se llena de vapor de un solvente dado, en este caso isopropanol, por lo

tanto relacionando el cambio en es espectro de reflectancia con la variación controlada de la presión parcial de isopropanol en el sistema de medida se obtienen las isotermas de adsorción/desorción de las cuales se calcula la distribución de poro de las láminas.

En la tabla 1 se resumen los datos de porosidad obtenidos de las láminas de nanopartículas con distinta cantidad de PEG. Como se puede observar a medida que la relación entre PEG y nanopartículas en las suspensiones precursoras aumenta el índice efectivo de las capas cae, lo que implica que la cantidad de aire dentro de la estructura es mayor y por lo tanto la porosidad también.

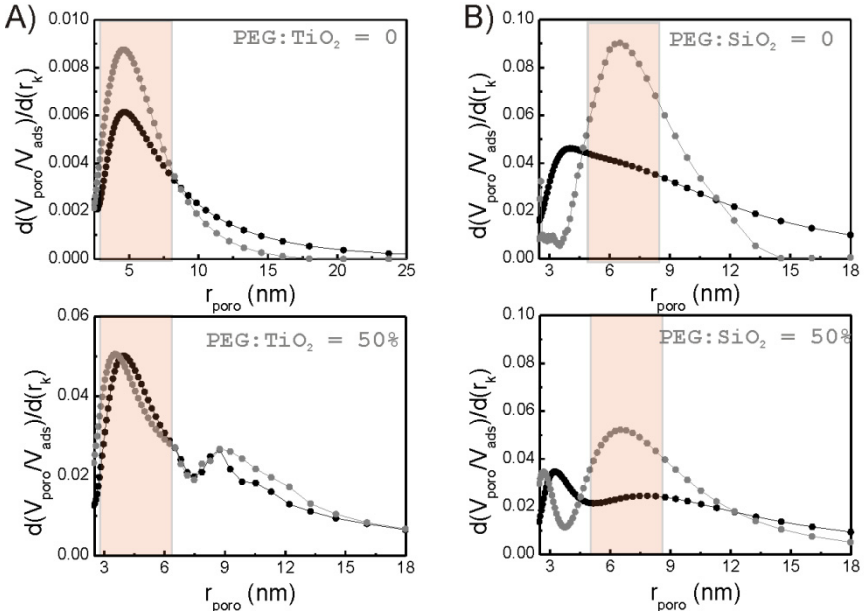

Figura 8. *Distribucion de tamaño de poro de las láminas creadas a partir de las suspensiones de A) TiO_2 y B) SiO_2 con distinta cantidad de porógeno.*

En la figura 8 se representan las distribuciones de tamaño de poro de las láminas de SiO_2 y TiO_2 en las que se usan diferentes cantidades de PEG para modificar la red porosa. Como se puede ver

Tras comprobar que la mezcla de nanopartículas con PEG aumenta la porosidad y el tamaño de poro de las láminas después de eliminar este último, el próximo objetivo era apilar dichas capas para formar una estructura con buenas propiedades ópticas. En la Figura 9 se presentan micrografías de SEM

correspondientes a secciones transversales de diferentes 1DPCs fabricados empleando tanto el método originalmente propuesto como aquél basado en la incorporación de una cierta PEG en las suspensiones precursoras de nanopartículas. Como se puede observar, además de la creación de poros de mayor tamaño en aquellas capas que incorporaban una cierta cantidad de porógeno, respuestas ópticas muy similares podían obtenerse con ambos tipos de estructuras.

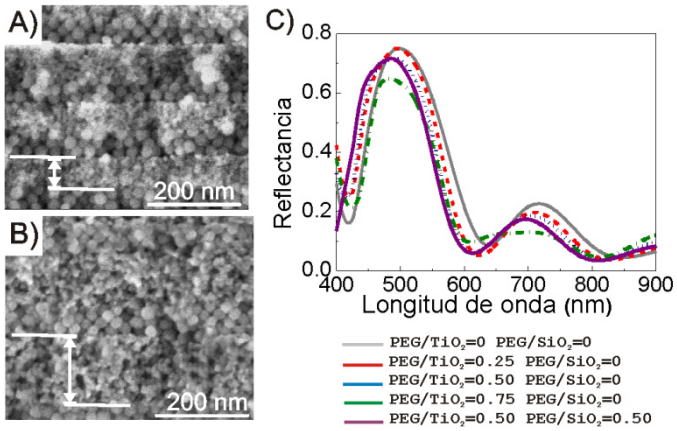

Figura 9. *A, B) Micrografías de SEM correspondientes a secciones transversales de 1DPCs fabricados usando suspensiones de nanopartículas como aquél basado en la incorporación de una cierta cantidad de PEG y C) espectros de reflectancia especular medidos para estos sistemas.*

Material	PEG:np (%peso)	n_{ef} monocapas	Porosidad de las monocapas (%)	n_{ef} en la estructura multicapa	Porosity (%) en la multicapa
TiO_2	----	1.70	47	1.69	47
	25	1.58	55	1.59	54
	50	1.55	57	1.54	57
	75	1.49	60	1.49	60
SiO_2	----	1.25	44	1.27	42
	50	1.22	50	1.22	50

Tabla 1. *Índices de refracción y porosidades de las capas individuales y dentro de la estructura multicapa.*

Los índices de refracción de estas láminas tras formar parte de una estructura multicapa se calcularon y se muestran en la tabla 1. Como se puede comprobar en la tabla, la porosidad de las capas de TiO_2 no se ven alteradas prácticamente al formar parte de la multicapa con respecto a la que presentan las monocapas. Sin embargo, para la capa de SiO_2 existe un pequeño aumento cuando forma parte de la estructura, esto puede ser debido a que la titania nanocristalina al ser de tamaño menor es capaz de penetrar por los huecos que forma la SiO_2 disminuyendo la porosidad de ésta.

Estudio de la Difusión a través de Cristales Fotónicos

La difusión a través de estos 1DPC con mayor porosidad se analizó mediante medidas de espectroscopia de impedancia. Para llevar a cabo tales medidas se preparó un dispositivo de doble electrodo con la multicapa separando dos vidrios conductores previamente platitinizados y embebida por una disolución de yodo 0.13 M en yoduro de 1-butil-3-metilimidazolio.

En primer lugar se midieron las curvas densidad de corriente frente a potencial para obtener las corrientes límites de difusión en función de la porosidad promedia del cristal fotónico y como evidencia la figura 10.A a medida que la porosidad del cristal aumenta dicha corriente baja lo que significa que hay un aumento en el transporte de masa a través de la estructura. Para un estudio más detallado cada muestra fue expuesta a cuatro corrientes con valores comprendidos entre 0 y el de la corriente límite correspondiente, obteniéndose los diagramas Nyquist. Esto nos permitió obtener los datos de resistecia asociada a la difusión de iones I^{3-} del electrolito empleado (R_d). Estos resultados se resumen en la figura 10.B, donde claramente se observa que tal resistencia disminuye a medida que aumenta la porosidad promedio del cristal fotónico. Por lo tanto, el aumento de transporte de masa a través de estos 1DPC es el resultado tanto de aumentar la porosidad como el tamaño medio de poro de la estructura.

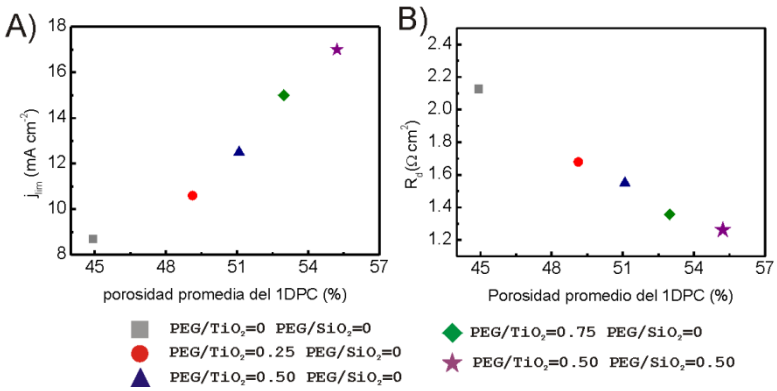

Figura 10. A) Corriente límite y B) Resistencia a la difusión obtenida a corriente 0 mA para los diferentes 1DPC.

Celdas solares de colorante basadas en cristales fotónicos de alta porosidad

En base a los resultados mostrados en el apartado anterior, el funcionamiento de estas nuevas estructuras periódicas como medio para aumentar la fotocorriente de las celdas solares de colorante se evaluó posteriormente tras ser integradas en DSCs de gran eficiencia basadas en el agente sensibilizador C101. Para este propósito los cristales fotónicos en los cuales la estructura porosa se había alterado se fabricaron usando en la suspensión de TiO_2 una relación en peso de PEG/TiO_2=0.5.

Los resultados extraídos para un set de electrodos de 5 µm de espesor se presentan en la Figura 11, donde se comparan, en primer lugar, las curvas IV obtenidas después de acoplar la estructura de 1DPC original y aquélla basada en la incorporación de la cantidad anteriormente mencionada de PEG. Como se puede apreciar en la gráfica, el mayor aumento de fotocorriente correspondía al caso en el que el cristal fotónico de mayor porosidad se incorporaba en el dispositivo, resultado esperado tras comprobar cómo el aumento de porosidad de la estructura hacia disminuir la resistencia a la difusión.

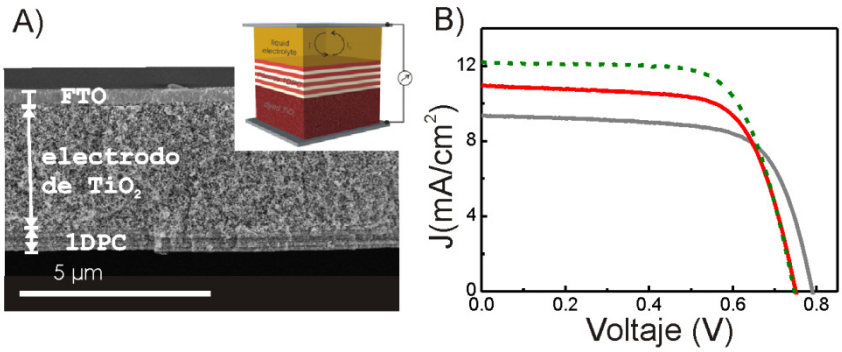

Figura 11. *A) Imágenes de SEM correspondientes a la sección transversal de un elecrtrodo de TiO_2 acoplado a un cristal ftónico. En el cuadro superior se encuentra un esquema de dicha delda. B) Curvas IV obtenidas para DSCs acoplada a: la estructura de 1DPC originalmente propuesta (línea roja) y la estructura de porosidad mejorada (línea verde punteada). En estas gráficas se incluyen también los datos correspondientes a una celda de referencia (línea gris continua).*

4. Cristal fotónico pancromático para la mejora del rendimiento de celdas solares de colorante

La amplificación de la absorción óptica que tiene lugar cuando se acopla un 1DPC al electrodo de una DSC es debido a reflexión de los fotones no absorbidos previamente con energías comprendidas dentro de la banda prohibida del cristal fotónico. De ahí que, las eficiencias más altas en DSC basadas en 1DPC se consigan acoplando multicapas cuyo pico de reflectancia coincida con el máximo de absorción de colorante. Por ello, extender el rango en el cual mejora la eficiencia de recolección de luz requiere el acoplamiento de 1DPC con bandas prohibidas más amplias en energía. Un cristal fotónico pancromático, es decir que refleje la mayor parte del espectro visible de la luz, es el resutado de apilar tres multicapas con diferente parámetro de red (Figura 12), de esta manera se aprovecha que cada cristal posea su band gap en un rango de longitudes de onda diferente, siendo el resultado final un aumento en la fotocorriente para un mayor rango de frecuencias. En la figura 12 se muestra el espectro de reflectancia total de este cristal fotónico de triple estructura junto con el de un cristal fotónico simple y una capa difusora de partículas de TiO_2 de 5µm de espesor acoplados a un electrodo de TiO_2 de 4.5 µm.

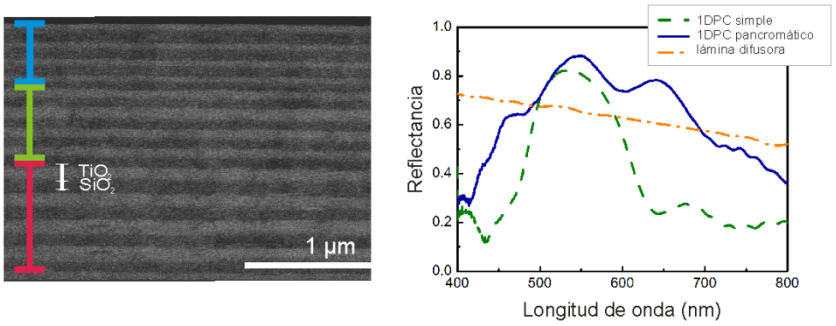

Figura 12. *Imágenes de SEM correspondientes a secciones transversales de un 1DPC compuesto por tres multicapas de distinto parámetro de red. Reflectancias de distintos elementos ópticos acoplados a un electrodo de TiO_2 nanocristalino.*

Una carasterística fundamental de las celdas solares de colorantes es su transparencia, gracias a la cual presentan gran potencial para ser usadas en aplicaciones de integración arquitectónica, característica que se preserva al integrar las estructuras fotónicas presentadas en esta tesis como revelan los datos de transparencia representados en la figura 13. Esto es debido a que, para las distintas estructuras fotónicas acopladas a las celdas solares, se mantiene una ventana de transparencia en el rango de mayores longitudes de onda del espectro visible. Por el contrario, el uso de láminas difusoras, las cuales dispersan la luz sin una dirección preferencial, daría como resultado celdas solares prácticamente opacas, lo cual impediría su uso en ciertas aplicaciones potenciales, tales como en módulos de ventana o de decoración interior.

Por otra parte la eficiencia de conversión de los distintos dispositivos se estimó a través de las correspondientes curvas IV bajo condiciones estándares de iluminación (Figura 13.B). Concluyendo que, las celdas basadas en cristales fotónicos mostraban un mejor comportamiento fotovoltaico y dentro de ellas la reflector pancromático daba el mayor aumento de fotocorriente, debido a la anchura espectral de su pico de reflectancia. Además si se comparan los valores de eficiencia de conversión se observa que se obtienen valores muy similares para los casos en los en los que se acoplaba un cristal fotónico pancromático (η=4.9) y una lámina difusora (η=5.2). Este es el mayor aumento en eficiencia conseguido integrando una estructura periodica a las DSCs con el valor añadido de preservar la semitransparencia del dispositivo.

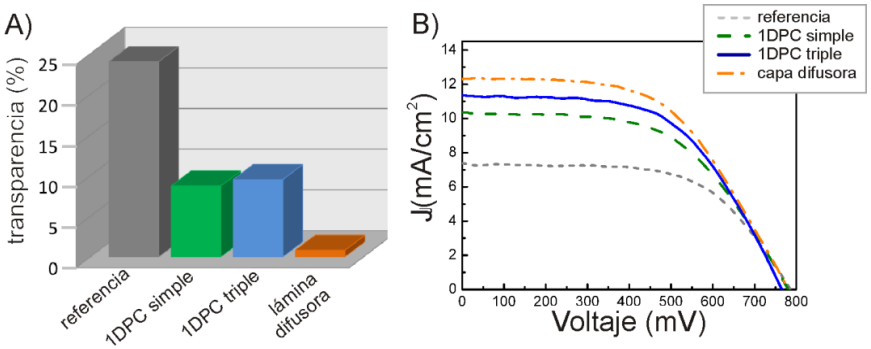

Figura 13. *A) Histograma mostrando los valores de transparencia de las DSCs acopladas a distintas estructuras ópticas. B) Curvas IV de dichos dispositivos.*

Por último para evaluar el rango espectral al que tiene lugar la mejora de fotocorriente se midieron los valores de IPCE del set de celdas analizadas en este apartado (Figura 14.A). El factor de mejora correspondiente al aumento de fotocorriente se calcula como la relación entre los valores de IPCE medidos para las celdas acopladas a estructuras ópticas y los valores de IPCE correspondientes a la celda referencia (Figura 14.B). El perfil de este factor de mejora da una idea del rango espectral en el que la absorción de la celda aumenta debida a la presencia de estas estructuras. Comparando estos perfiles se ve claramente que tanto la celda en la cual ha sido integrado un cristal fotónico pancromático como aquella en la que lo ha sido una lámina difusora presentan perfiles muy similares cubriendo todo el rango visible del espectro, lo cual está en concordancia con los valores parecidos de fotocorriente obtenidos en ambos diseños.

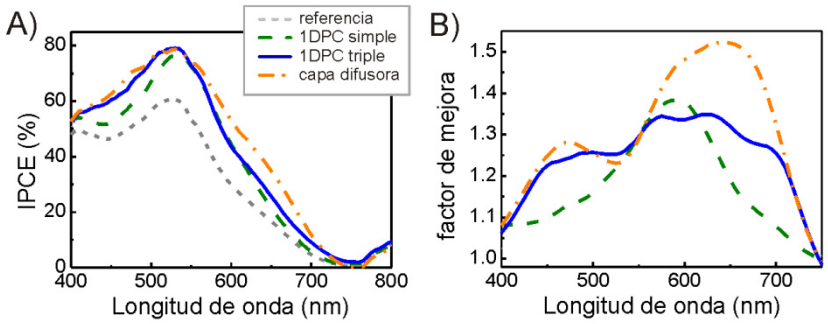

Figura 14. *A) Valores de IPCE y de B) factores de aumento de fotocorriente para distintos diseños de DSC.*

5. Respuesta angular de celdas solares de colorante basadas en cristales fotónicos unidimensionales

El espectro de reflectancia de un cristal fotónico es el resultado de efectos de interferencia de la luz reflejada y transmitida en las intercaras de las capas que forman la estructura dependientes a su vez de la dirección de propagación de la luz. Por lo tanto la posición espectral del máximo de reflexión o pico de Bragg, λ_B, de un cristal fotónico compuesto por dos capas alternas de espesores t_1y t_2 y de índices de refracción n_1 y n_2 respectivamente depende del angulo de incidencia de la luz con respecto a la normal de la superficie, □, como expresa la ecuación:

$$\lambda_B = 2d\sqrt{n^2 - (\sin\theta)^2} \quad (1)$$

Donde d es el tamaño de celda unidad y n el índice de refracción efectivo de la estructura, dado por:

$$n = \frac{t_1 n_1 + t_2 n_2}{d} \quad (2)$$

Puesto que la respuesta óptica de los cristales fotónicos es diferente dependiendo del ángulo de incidencia de la luz, es importante conocer cómo se va a comportar los dispositivos que usan este tipo de estructuras para mejorar su rendimiento según el ángulo de iluminación.

En este estudio se van a evaluar el comportamiento de dispositivos solares en los que se han integrado cristales con distinto parámetro de red, es decir estructuras que reflejan distintos rangos del espectro visible, un cristal fotónico pancromático, como el presentado en la sección anterior y una lámina difusora de partículas de TiO_2 con un espesor de 5μm. También se analizo el comportamiento angular de una celda referencia (fabricada usando el mismo espesor de electrodo pero sin contener ningún elemento óptico adicional) y de una celda incluyendo una lámina difusora de 5 μm de espesor. En la figura 15 se presentan los espectros de reflectancia total de dichas etructuras junto a la absorptancia de una lamina de TiO_2 sensitivizada con el colorante usado (N719) en las DSCs.

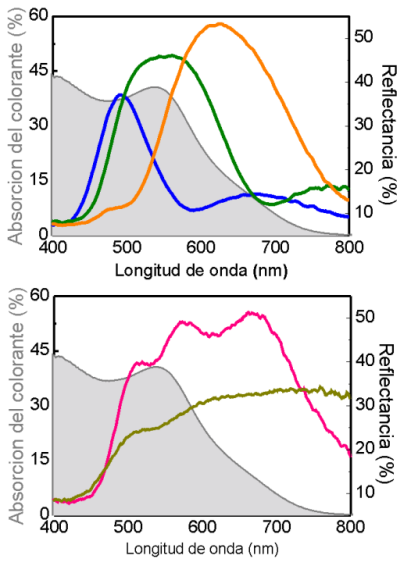

Figura 15. *Espectros de reflectancia total de tres cristales fotónicos cuyo parámetro de red es constante (azul, verde y naranja),un cristal fotónico pancromático (magenta) y una lámina difusora acoplados a electrodos de TiO_2. El espectro de absorción del colorante usado (N719) también se muestra (área gris).*

Variación de las Propiedades Ópticas en función del Ángulo de Incidencia de la Luz

En primer lugar se estudio el cambio en apariencia de las celdas a medida que el ángulo de incidencia de la luz se aleja de la normal a la superficie del dispositivo.

Para tal fin, se recogieron los espectros de transmitancia de cada muestra desde 0 a 60 grados y a partir de ellos se calcula la transparencia de la celda en cada situación. Como se observa en la figura 16 A la transparencia de la celda referencia cae ligeramente al aumentar el ángulo de incidencia como consecuencia tanto del aumento de reflectancia en la interfaz aire/vidrio tal como prevé la ley de Fresnell como por aumento del paso óptico a través del electrodo, lo que aumenta la cantidad de luz absorbida por el colorante. Por otro lado, los cambios observados en las celdas con cristal fotónico son de origen más complejo, siendo el principal motivo el desplazamiento del pico de reflectancia hacia longitudes de onda más cortas, lo que hacer cambiar su posición relativa al espectro de absortancia del colorante. Por lo tanto según el

pico de reflectancia de la multicapa se vaya alejando o acercando espectralmente al máximo de absorción del colorante la transparencia de la celda irá aumentando o disminuyendo respectivamente. Este desplazamiento de la posición espectral del pico de Bragg es también apreciable a simple vista como se aprecia en la figura 16 B y C.

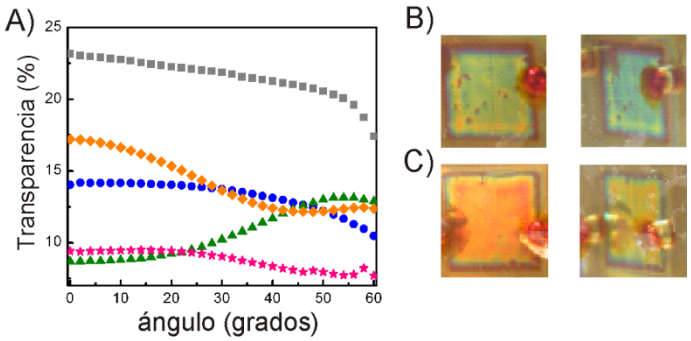

Figura 16. *A) Evolucion de la transparencia de las celdas según el ángulo de incidencia de la luz para una celda referencia (cuadrados grises) y celdas en las que se han integrado distintos cristales fotónicos reflejando en el rango azul (círculos azules), verde (triangulos verdes) y rojo (rombos naranjas) del espectro visible. Los valores de transparencia de una celda conteniendo un cristal pancromático también son graficados (estrellas rosas).*

Variación de las Propiedades Fotovoltaicas en función del Ángulo de Incidencia de la Luz

La posición relativa del pico de reflectancia de la estructura fotónica con el espectro de absorción del colorante determinará la eficiencia final del dispositivo. Cuanto mayor sea el acoplamiento entre ambos espectros mayor será la eficiencia de conversión de la celda solar. Por ello, es interesante estudiar como varía la respuesta fotovoltaica de los dispositivos al cambiar el espectro de reflectancia de los 1DPCs como consecuencia del angulo de iluminación. Para este estudio se analizaron las curvas IV de los distintos dispositivos variando el ángulo de iluminación de 0 a 60 grados.

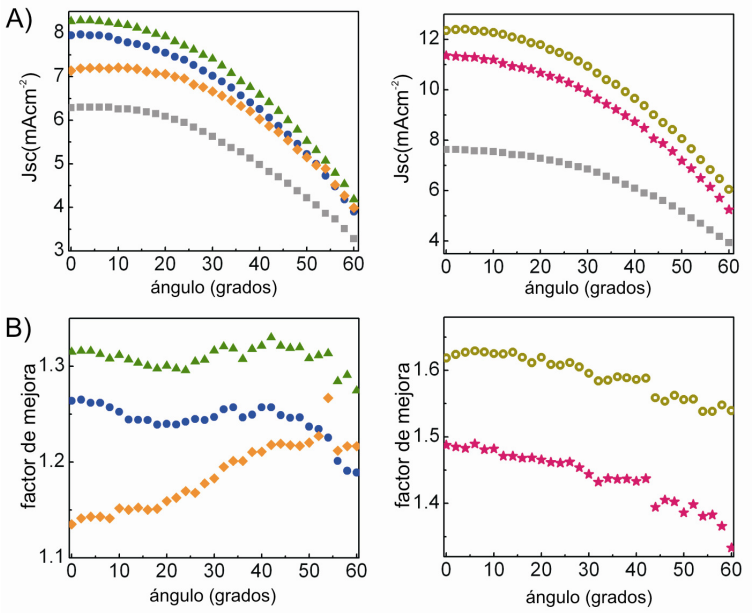

Figura 17. *A) Jsc en función del angulo de iluminación para una celda referencia (cuadros grises), tres celdas en las que se han acoplado cristales fotónicos de multicapa simple cuyos picos de reflectancia se centran en λ = 500 (círculos azules), λ = 550 (triangulos verdes) y λ = 630 (rombos naanjas), una celda acoplada a un cristal fotónico pancromático (círculos amarillos) y a una lámina difusora (estrellas magenta). B) factor de mejora de Jsc con el mismo criterio de colores.*

En la figura 17 se recoge la evolución de la fotocorriente a circuito cerrado (Jsc) con el angulo de incidencia de la luz. El comportamiento observado en este caso sigue la ley del coseno de Lambert, según la cual la iluminación producida sobre una superficie, I, por una fuente luminosa puntual es proporcional al angulo de incidencia, □:

$$I(\theta) = I(0)\cos(\theta) \qquad 3$$

Este es el origen de las llamadas "perdidas tipo coseno" que aparecen cuando los módulos fotovoltaicos operan con una cierta inclinación. Sin embargo la caída de fotocorriente observada experimentalmente no se ajusta exactamente a la ecuación anterior, debido a que a medida que el ángulo de iluminación es mayor el recorrido que la luz hace dentro del electrodo aumenta, incrementándose con ello la probabilidad de absorción de fotones y por lo tanto la fotocorriente. Además, para ángulos altos, se produce perdida de

fotones por reflexión en la interfaz aire/vidrio. Este comportamiento es general para todos los dispositivos bajo estudio. En este punto es importante remarcar que la tendencia observada para el dispositivo con la lámina difusora es la que más se ajusta a la curva prevista por la ley del coseno de Lambert, debido a que la presencia de esta lámina aleatoriza la dirección de la luz en el interior del electrodo sensitivizado, enmascarando el efecto del aumento del camino óptico producido al aumentar el ángulo de iluminación.

Para el caso de las DSCs basadas en 1DPCs la principal razón de la diferencia entre los valores de fotocorriente obtenidos en su caso y en el caso de la celda de referencia es debido al diferente aumento en absorción obtenido como consecuencia del solapamiento entre el pico de Bragg y la banda de absorción del colorante. Esto explica el efecto observado para aquel dispositivo en el que se integro un 1DPC cuyo máximo de reflectancia se situaba en λ = 630 nm, en el cual este solapamiento aumenta a medida que también lo hace el ángulo de iluminación obteniéndose para ángulos altos las mayores mejoras de fotocorriente.

Por otra parte, la variación de la Voc con el ángulo de incidencia sigue la siguiente ecuación basada en un modelo de diodo, en el cual la lámina mesoporosa de TiO_2 se comporta como material tipo n y el par redox como material tipo p:

$$V_{OC} = m\frac{KT}{e}\ln\left(\frac{\mathrm{Isc}}{I0}\right) \qquad 4$$

Donde m es un factor de idealidad, cuyo valor varía entre 1 y 2, T la temperatura de la celda, K la constante de Boltzman y e la carga del electrón. El comportamiento angular del Voc se puede describir en una primera aproximación considerando la ley del coseno de Lambert siguiendo la ecuación:

$$V_{OC}(\theta) = V_{OC}(0) + m\frac{KT}{e}\ln\left(\frac{\mathrm{I}(\theta)}{I(0)}\right) = V_{OC}(0) + m\frac{KT}{e}\ln(\cos\theta) \qquad 5$$

Donde Voc (0) es el voltaje a circuito abierto a incidencia normal. Sin embargo la tendencia del Voc de los dispositivos con cristal fotónico se aleja de las previsiones de esta ecuación donde el poder electromagnético dentro del electrodo depende fuertemente de la posición relativa del pico de Bragg con respecto a la banda de absorción del rutenio.

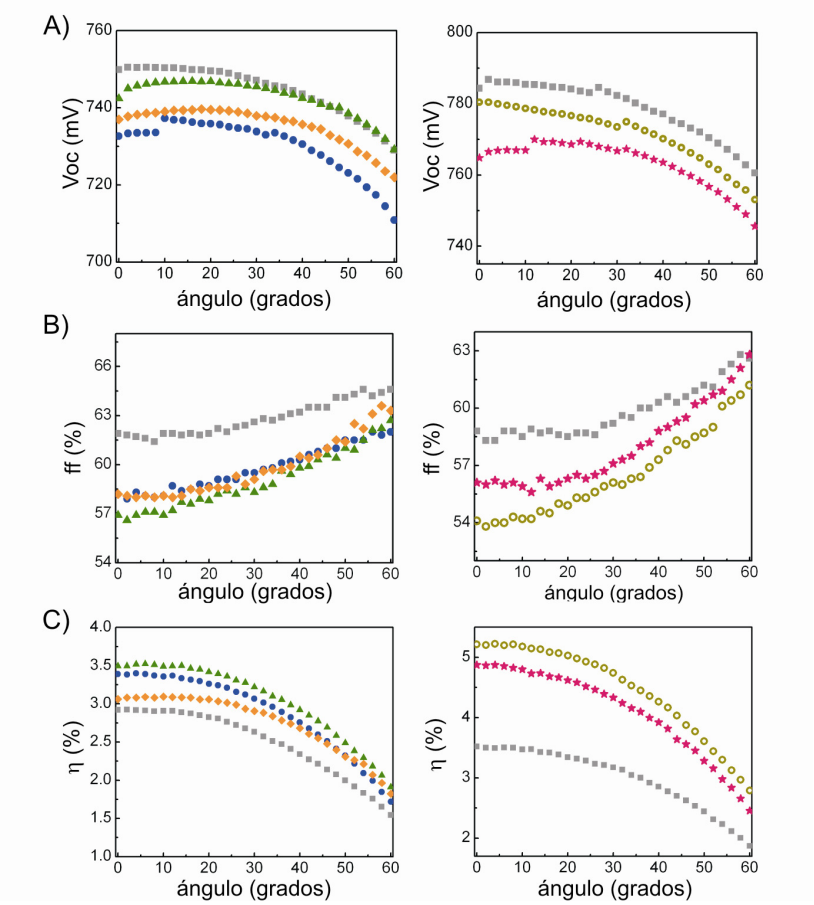

***Figura 18**. A) Voc, B) ff y C) eficiencia de una celda referencia (cuadros grises), tres celdas en las que se han acoplado cristales fotónicos de multicapa simple cuyos picos de reflectancia se centran en λ = 500 (círculos azules), λ = 550 (triangulos verdes) y λ = 630 (rombos naanjas), una celda acoplada a un cristal fotónico pancromático (cículos amarillos) y a una lámina difusora (estrellas magenta).*

Con respecto al fill factor, ff, el hecho de acoplar un material reflector al electrodo de trabajo da lugar a pequeñas resistencias al flujo de electrolito disminuyendo el ff. Cuando estos dispositivos fotovoltaicos se iluminan con un cierto ángulo, la irradiancia que alcanza la superficie de la celda es menor de acuerdo con la ley del coseno de Lambert previamente comentada, lo cual conduce a una reducción de las resistencias internas de la celda dependientes de la cantidad de carga,[43] reduciendo la recombinación de carga y aumentando el ff, como se observa en la figura 18.B. Un efecto secundario causado por la reducción de la cantidad de carga es la disminución de la movilidad de

electrones en la red de semiconductor debido al aumento de la probabilidad de que esos electrones queden atrapados en "trampas" (niveles energéticos por debajo de la banda de conducción), reduciendo el ff. Sin embargo, el efecto producido por la caída de las resistencias internas es mayor que este último, por lo que queda finalmente enmascarado.

Finalmente, la evolución de la eficiencia de conversión, η, con el ángulo de incidencia sigue la tendencia observada para la Jsc, pero con una caída más lenta causada por el comportamiento opuesto de Voc y ff.

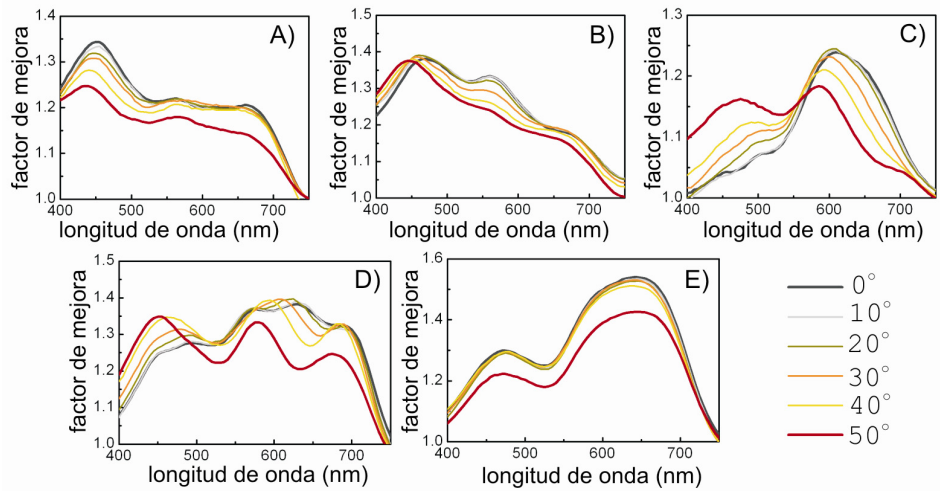

Figura 19. *Factor de mejora de IPCE de celdas en las que se han acoplado cristales fotónicos de multicapa simple cuyos picos de reflectancia se centran en λ = 500 (A), λ = 550 (B) y λ = 630 (C), una celda acoplada a un cristal fotónico pancromático (D) y a una lámina difusora (F).*

Por otro lado, para relacionar los cambios en fotocorriente medidos con el desplazamiento hacia longitudes de onda menores a medida que el angulo de iluminación aumenta de los dispositivos con cristal fotónico, los valores de IPCE se adquirieron. En principio, cuando estos 1DPCs se emplean se obtiene un aumento de IPCE para cualquier ángulo, lo que está en concordancia con los resultados obtenidos de las curvas IV y presentados anteriormente, presentando el mayor aumento en el rango espectral en el que el cristal fotónico posee su pico de reflectancia.

Para cada ángulo se calculó el factor de aumento de la IPCE para las celdas que contenían el material dispersante de luz. De esta manera se ve claramente

que este factor de aumento se desplaza hacia longitudes de onda menores a medida que aumenta la inclinación de la celda, mientras que para el caso en el que se usa una lámina difusora este factor de mejora permanece invariable espectralmente. De nuevo este comportamiento es debido al desplazamiento de la posición espectral del pico de Bragg dado por la ecuación 1.

6. Redes de Difracción Unidimensionales para Mejorar la Recolección de Luz en Celdas Solares de Colorante

En esta última sección se va a llevar a cabo un estudio de las mejoras en fotocorriente de una celda solar de colorante cuando se emplea una red de difracción unidimensional para aumentar el camino óptico dentro del electrodo sensitivizado con colorante.

En este caso los electrodos de TiO_2 se moldearon para obtener una red de difracción en su superficie posterior, de este modo cuando los fotones que no han sido absorbidos previamente llegan a esta estructura periódica son reflejados de vuelta la lámina fotoactiva con un cierto ángulo aumentando el paso óptico y por lo tanto la eficiencia de recolección de luz.

Para fabricar dichos electrodos texturizados primeramente se emplea la litografía suave para obtener un sello hecho de un composite basado en h-PDMS[44] a partir de un patrón comercial que presenta un perfil de dientes de sierra con una periodicidad de 1200 líneas/mm.[45] Se usó h-PDMS como material para conseguir los sellos por su habilidad para reproducir y transferir un patrón fielmente.[46,47] El siguiente paso consiste en presionar este sello contra la pasta de TiO_2 a una temperatura adecuada, transcurridos unos minutos ambas estructuras se separan y el electrodo de TiO_2 se sinteriza. En la figura 20, se presentan las imágenes recogidas por AFM (microscopia de fuerza atómica) y los perfiles tanto del sello como del electrodo final para demostrar el buen funcionamiento de este proceso.

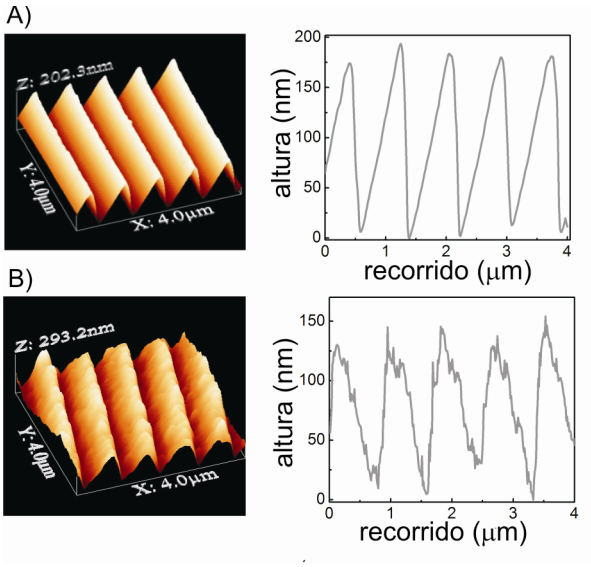

Figura 20*.Imágenes de AFM y perfiles A) del sello de h-PDMS y B) del electrodo estampado.*

El comportamiento de estos electrodos como redes de difracción se evaluó comparando medidas del ángulo de difracción y de eficiencia de reflectancia en función de la longitud de onda incidente con cálculos teóricos (Figura 21). El ángulo de difracción de la luz con una longitud de onda, λ, para una red cuyo especio entre cimas, l:[48]

$$m\lambda = l(\sin i + \sin r) \qquad 6$$

Donde m es el orden de difracción, y Θi y Θr son el ángulo de incidencia y reflejado medidos con respecto a la normal de la red. Por otro lado, el cálculo de la eficiencia de reflectancia se hizo empleando un código basado en un análisis de la teoría de ondas acopladas (RCW).[49] La comparación entre los datos teóricos y experimentales demuestra que estos electrodos poseen propiedades de redes de difracción en el rango espectral de la banda de absorción del colorante de rutenio.

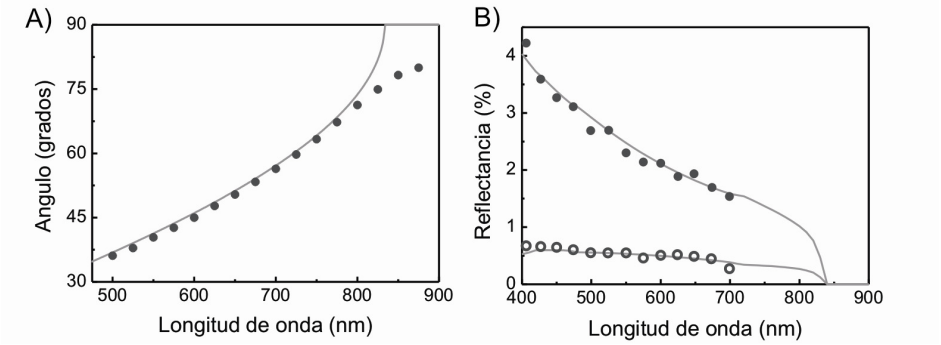

Figura 21.*A) Dependencia angular de la luz difractada por la red de difraccion bajo estudio. B) Datos experimentales (línea solida) y teóricos (circulos) de la eficiencia de reflexión espectral.*

Estos electrodos estampados están diseñados para ser usados tanto como redes de difracción por reflexión como por transmisión, por ello es interesante estudiar el comportamiento de las celdas en las que se usan dichos electrodos cuando estos son iluminados desde la cara frontal como desde la posterior. En este último caso la luz pasa por el electrolito antes de llegar a la superficie corrugada periódicamente para abrirse en diferentes haces dependiendo de la longitud de onda y viajar por lámina activa. Para este análisis celdas referencias en las cuales se emplea un electrodo de igual espesor al de la celda con la red de difracción pero sin esta superficie de difracción se emplean para comparar ambos comportamientos. En la figura 22 se muestran las curvas IV y los datos de IPCE. Como se puede ver en ambos casos la presencia de esta superficie con propiedades de redes de difraccion da lugar a un aumento de fotocorriente del dispositivo causado por el aumento del paso óptico de la luz en el electrodo fotoactivo.

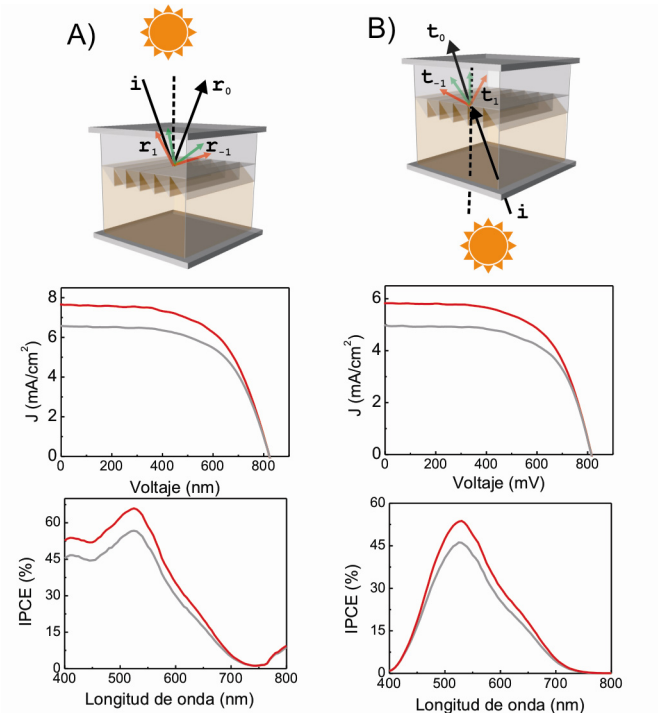

Figura 22. Curvas IV e IPCE recogidas bajo A) iluminación frontal y B) iluminación trasera.

7. Conclusiones

Se ha propuesto un método para modificar la red de poros de las estructuras de 1DPC de nanopartículas mediante la incorporación de polímeros orgánicos en las suspensiones precursoras. La posterior eliminación por calentamiento de estos polímeros da lugar a la creación de poros de mayor tamaño, lo que facilita el transporte de especies a través de la estructura fotónica.

El acoplamiento de estructuras de 1DPC con una porosidad optimizada en DSCs ha dado lugar a aumentos de eficiencia mayores que las conseguidas con los cristales fotónicos originales.

Se ha demostrado por primera vez que mediante el acoplamiento a una DSC de un cristal fotónico cuyo pico de reflectancia cubra el rango del espectro de absorbancia del colorante usado en la celda es posible obtener mejoras de eficiencia y fotocorriente similares a las obtenidas acoplando una lámina difusora de partículas de TiO_2. Además esta compleja estructura multicapa con

propiedades de cristal fotónico tiene la capacidad de preservar la semitransparencia de la celda.

Se ha estudiado el comportamiento de DSCs en las que se integran distintos cristales fotónicos frente al ángulo de iluminación. Encontrándose que es posible minimizar las "pérdidas tipo coseno" en la fotocorriente de las celdas utilizando un cristal fotónico con un diseño adecuado.

Por último, se propone el uso de electrodos en los que se ha estampado una red de difracción en su parte trasera para aumentar el camino óptico de la luz. Consiguiéndose de este modo un diseño de la celda con un comportamiento fotovoltaico mejorado cuando esta es iluminada desde ambos lados.

8. Referencias

[1] B. O'Regan, M. Grätzel, Nature, 1991, 353, 737.

[2] J.E. Moser, M. Grätzel, Chimia, 1998, 52, 160.

[3] A.J. Frank, N. Kopidakis, J. van de Lagemaat, Coordin. Chem. Rev., 2004, 248, 1165.

[4] J. Halme, G. Boschloo, A. Hagfeldt, P. Lund, *J. Phys Chem C*, 2008, **112**, 5623.

[5] R.P. Barnes, A.Y. Anderson, S.E. Koops, J.R. Durrant, B.C. O'Regan, *J. Phys Chem C*, 2009, **113**, 1126.

[6] H. C. van de Hulst, Light Scattering by Small Particles, Wiley, New York 1957.

[7] Y. Chiba, A. Islam, Y. Watanabe, R. Komiya, N. Koide, L. Han, Jpn. J. Appl. Phys., 2006, 45, 638.

[8] F. Gao, Y. Wang, D. Shi, J. Zhang, M. Wang, X. Jing, R. Humphry-Baker, P. Wang, S. M. Zakeeruddin, M. Grätzel, J. Am. Chem. Soc., 2008, 130, 10720.

[9] C. Chen, M. Wang, J. Li, N. Pootrakulchote, L. Alibabaei, C. Ngocle, JD. Decoppet, J.Tsai, C. Gra□tzel, C.Wu, SM. Zakeeruddin, M. Gra□tzel, ACS Nano, 2009, 3, 3103.

[10] Y. Cao, Y. Bai, Q. Yu, Y. Cheng, S. Liu, D. Shi, F. Gao, P. Wang, J Phys Chem C, 2009, 113, 6290.

[11] A. Yella, H.W. Lee, H.N. Tsao, C.Y. Yi, A.K. Chandiran, M.K. Nazeeruddin, E.W.G. Diau, C.Y. Yeh, S.M. Zakeeruddin, M. Grätzel, Science, 2011, 334, 629.

[12] A. Usami, Chem. Phys. Lett., 1997, 277, 105.

[13] J. Ferber, J. Luther, Sol. Energy Mater. Sol. Cells, 1998, 54, 265.

[14] G. Rothenberger, P. Comte and M. Gratzel, Sol. Energy Mater. Sol. Cells, 1999, 58, 321.

[15] W.E. Vargas, G.A. Niklasson, Sol. Energy Mater. Sol. Cells, 2001, 69, 147.

[16] Y. Tachibana, K. Hara, K. Sayama, H. Arakawa, Chem. Mater., 2002, 14, 2527.

[17] F. E. Galvez, E. Kemppainen, H. Miguez and J. Halme, J. Phys. Chem. C, 2012, 116, 11426.

[18] Z. S. Wang, H. Kawauchi, T. Kashima and H. Arakawa, Coord. Chem. Rev., 2004, 248, 1381.

[19] H. koo, Y.J. Kim, Y.H. Lee, W. I. Lee, K.Kim, N. Park, Adv. Mater., 2008, 20, 195.

[20] Y.J. Kim, M.H. Lee, H.J. Kim, G. Lim, Y.S. Choi, N.G. Park, K. Kim, W.I. Lee, Adv. Mat., 2009, 21, 3668.

[21] K.R. Catchpole, A. Polman, Opt. Express, 2008, 16, 21793.

[22] H.A. Atwater, A. Polman, Nat. Mater., 2010, 9, 205.

[23] D. Derkacs, S. H. Lim, P. Matheu, W. Mar, E. T. Yu, Appl. Phys. Lett., 2006, 89, 093103.

[24] K. Tvingstedt , N.K. Persson , O. Inganas , A. Rahachou , I. V. Zozoulenko, Appl. Phys. Lett. 2007, 91, 113514 .

[25] S. Standridge, G. Schatz, J. Hupp, J. Am. Chem. Soc. 2009, 131, 8407.

[26] M.D. Brown, T. Suteewong, R.S.S. Kumar, V. D'Innocenzo, A. Petrozza, M.M. Lee, U. Wiesner, H.J. Snaith, Nano Lett., 2011, 11, 438.

[27] J. Qi, X. Dang, P.T. Hammond, A.M. Belcher, ACS Nano, 2011, 5, 7108.

[28] H. Choi, W.T. Chen, P.V. Kamat, ACS Nano, 2012, 6, 4418.

[29] J. Kim , J. K. Koh , B. Kim , J. H. Kim , E. Kim , Angew. Chem. Int. Ed,. 2012 , 51 , 6864 .

[30] S. Wooh, H. Yoon, JH. Jung, YG. Lee, J.H. Koh, B.Lee, Y.S. Kang, K. Char, Adv. Mat., 2013, 25, 3111.

[31] A. Baba, K. Wakatsuki, K. Shinbo, K. Kato, F. Kaneko, J. Mater. Chem., 2011, 21, 16436.

[32] I. K. Ding, J. Zhu, W. Cai, S.-J. Moon, N. Cai, P. Wang, S. M. Zakeeruddin, M. Grätzel, M. L. Brongersma, Y. Cui,M. D. McGehee, Adv. Energy Mater., 2011, 1, 52.

[33] J. Joannopoulos, R. Meade, J. Winn, Photonic Crystals: Molding the Flow of Light, 1995,Princeton University Press, New Jersey.

[34] S. Nishimura, N. Abrams, B.A. Lewis, L.I. Halaoui, T.E. Mallouk, K.D. Benkstein, J. van de Lagemaat, A.J. Frank, J. Am. Chem. Soc., 2003, 125, 6306.

[35] A. Mihi, H. Míguez, J. Phys. Chem. B, 2005, 109, 15968.

[36] S. Colodrero, A. Mihi, L. Haggman, M. Ocaña, G. Boschloo, A. Hagfeldt, H. Míguez, Adv. Mat., 2009, 21, 764.

[37] S. Colodrero, M. Ocaña, H. Miguez, Langmuir, 24, 2008, 4430.

[38] G. Lozano, S. Colodrero, O. Caulier, M. E. Calvo, H. Miguez, J. Phys. Chem. C, 2010, 114, 3681.

[39] M.V. Badiger, M.E. McNeill, N.B. Graham, Biomaterials, 1993, 14, 1059.

[40] E. Della Gaspera, A. Antonello, M. Guglielmi, M.L. Post, V. Bello, G. Mattei, F. Romanato, A. Martucci, J. Mater. Chem., 2011, 21, 4293.

[41] D. P. Puzzo, L. D. Bonifacio, J. Oreopoulos, C. M. Yip, I. Manners and G. A. Ozin, J. Mater. Chem., 2009, 19, 3500.

[42] N. Hidalgo, C. López-López, G. Lozano, M.E. Calvo, H. Míguez, Langmuir, 2012, 28, 13777.

[43] B.C. O´Regan, J.R.Durrant, Acc.Chem.Res., 2009, 42, 1799.

[44] H. Schmid, B. Michel, Macromolecules, 2000, 33, 3042.

[45] D. Quin, Y. Xia, G.M. Whitesides, Nature protocols, 2010, 5, 491.

[46] T.W. Odom, J.C. Love, D.B. Wolfe, K.E. Paul, G.M. Whitesides, Langmuir, 2002, 18, 5314.

[47] TW. Lee, O. Mitrofanov, J.W.W. Hsu, Adv. Funct. Mater., 2005, 15, 1683.

[48] C. Palmer and E. Lowen, Diffraction Grating Handbook (Richardson Grating Laboratory, Rochester, NY, 2002).

[49] M.G. Moharam, T.K. Gaylord, J. Opt. Soc. Am. 1981, 71, 811.

List of Publications

The most relevant publications resulting from this thesis are:

1. Enhanced diffusion through porous nanoparticle optical multilayers
   C. López-López, S. Colodrero, S.R. Raga, H. Lindström, F. Fabregat-Santiago, J. Bisquert, H. Míguez
   J. Mater. Chem., 2012, 22, 1751
2. Characterization of mesoporous thin film by Specular Relfectance Porosimetry
   N. Hidalgo, **C. López-López**, G. Lozano, M.E. Calvo, H. Míguez
   Langmuir, 2012, 28, 13777
3. Panchromatic porous specular back reflectors for efficient transparent dye solar cells
   C. López-López, S. Colodrero, H. Míguez
   Phys. Chem. Chem. Phys., 2013, to be published.
4. Angular response of photonic crystal based dye sensitized solar cells
   C. López-López, S. Colodrero, M.E. Calvo, H. Míguez
   Energy Environ. Sci., 2013, 6, 1260.
5. Effect of patterning one dimensional optical gratings onto dye sensitized electrodes
   C. López-López, S. Colodrero, A. Jiménez-Solano, R. Ortiz, M.E. Calvo, H. Míguez

Other publications closely related to this thesis are listed below:

6. Porous one dimensional photonic crystals: novel multifunctional materials for environmental and energy applications
   M.E. Calvo, S. Colodrero, N. Hidalgo, G. Lozano, **C. López-López**, O. Sánchez-Sobrado, H. Míguez
   Energy Environ. Sci., 2011, 4, 4800

7. Efficient Transparent Thin Dye Solar Cells Based on Highly Porous 1D Photonic Crystals
S. Colodrero, A. Forneli, **C. López-López**, L. Pellejà, H. Míguez, E. Palomares
Adv. Funct. Mater., 2012, 22, 1303

Other publications:

8. Integration of gold nanoparticles in optical resonators
Jiménez-Solano, **C. López-López**, O. Sánchez-Sobrado, J.M. Luque, M.E. Calvo, C. Fernández-López, A. Sánchez-Iglesias, L.M. Liz-Marzán, H. Míguez
Langmuir, 2012, 28, 9161.

9. Collective osmotic shock: a novel method for polymeric membrane generations
P. Zabala Rivera, E. Sivaniah, S.K. Nataraj, M.E. Calvo, H. Míguez, **C. López-López**
Procedia Engineering, 2012, 44, 323.